LONDON'S GLOBAL UNIVERSITY

The investigation into highly efficient heptazine-based polymeric photocatalysts for visible light-driven solar fuel synthesis

Yiou Wang

2019.1

A thesis submitted for the degree of Doctor of Philosophy at University College London

Department of Chemical Engineering,
University College London,
Torrington Place,
London,
WC1E 7JE

Declaration:

I, Yiou Wang, confirm that the work presented in this thesis is my own. Where information has been derived from other sources, I confirm that this has been indicated in the thesis.

.....

Signature

.....

Date

I. Acknowledgements

I want to give my sincere thanks to my supervisor Prof. Junwang Tang for his guidance and kindness over the past four years. He strongly and continuously supported me. In the difficult times of my research, it was his expertise, outstanding insight and continuous determination that guided me out of struggling. I learnt a lot from him and would learn more in the future if possible. To me, he will remain a lifelong mentor.

Huge thanks must go to Dr Mustafa K. Bayazit and Dr Savio J.A. Moniz, the two senior researchers in the group. Their caring, suggestions and discussions during these years have made my life much easier. Also, I want to thank both as two lab safety managers, who keep my everyday environment tidy and safe.

I also thank Prof. James Durrant, Dr Robert Godin and Dr Wenxing Yang for their expertise and contribution in the discussion of ultrafast time-resolved spectroscopies. Thanks to Prof. C. Richard. A. Catlow, Prof. Zhengxiao Guo, Dr Xiaoyu Han, Dr Natalia Martsinovich and Fabrizio Silveri for their DFT computing results and the patient discussions during the collaborations. They have made a substantial

contribution to my projects and taught me very useful knowledge in computing modelling and mechanistic understanding.

Thanks to Dr Jiefang Sun, Dr Xu Liu, Dr Nianquan Jiang, and Dr Wenjun Luo, visiting scholars from China. Their unique advice has been quite useful for my research, and I hope their career would succeed more in the future.

I am grateful to my colleagues in my group: Dr Chiching Lau, Chaoran Jiang, Qiushi Ruan, Dan Kong, Yaomin Li, Jijia Xie, Ayoola Shoneye, Deqiang Zhao, Qingning Yang, Hui Wang, Dr Kiran Vankayala, Dr Christopher Windle and all the rest of you guys. My kind colleagues were always helpful and did me a lot of favour in these years. My discussions and collaborations made my life fun.

I especially acknowledge China Scholarship Council (CSC) for my PhD funding and Royal Society of Chemistry for an early-career travel funding. Finally, to my family, Mum, Dad, my girlfriend Miss Pianpian Wang and my cousins, who believe in me throughout the good times and bad - I couldn't have made such progress without you. You are here; there is nothing I fear.

II. Abstract

Artificial photosynthesis has been regarded as a promising method to generate fuels in a much greener way by utilising inexhaustible solar energy via water splitting and CO_2 conversion. Polymeric semiconductors have been recently identified as promising photocatalysts due to their comparatively low cost and ease modification of the electronic structure. However, the majority only respond to a limited wavelength region (<460 nm) and still suffer from fast charge recombination. Herein, a novel synthetic pathway has been developed to control the O and N linker/terminal species in polymeric photocatalysts, which highly influences the bandgap, band positions and charge separation. As such, the synthesised oxygen-doped C_3N_4 polymers can be excited from UV via visible to even near-IR (800 nm) wavelengths, resulting in one order of magnitude higher H_2 evolution rate than the widely-reported polymeric g-C_3N_4 (λ > 420 nm), leading to a 10.3% apparent quantum yield (λ = 420 nm). Both theoretical calculations and spectroscopies have attributed such superior performance to enhanced charge separation and narrow bandgap. Such new polymer was then coupled with an inorganic photocatalyst

to construct a Z-scheme system, which successfully splits water into both H_2 and O_2 in a stoichiometry ratio.

Further, an efficient strategy was demonstrated to stepwise tailor the bandgap of polymeric photocatalysts from 2.7 to 1.9 eV by carefully manipulating the O/N linker/terminal atoms in the heptazine chains. These polymers work stably and efficiently for both H_2 and O_2 evolution (420 nm < λ < 710 nm), exhibiting nearly 20 times higher activity compared to g-C_3N_4 with high AQYs under visible light irradiation. Experimental and theoretical results have attributed the narrowed band gap and enhanced charge separation to the oxygen incorporation into the linker/terminal position.

Based on this success, a more challenging multi-electron photochemical process of visible light-driven CO_2 reduction in water was investigated using junctions consisting of the novel polymers and two kinds of carbon quantum dots (CQD) cocatalysts. The novel CQD was synthesised via a microwave-assisted method while the other CQD fabricated via sonication of glucose was reported as reduction cocatalysts (^{red}CQD). In CO_2 reduction reactions, the novel CQD/polymer junctions selectively produce methanol and O_2 while the ^{red}CQD/polymer junction generates CO only. Ultrafast spectroscopies

revealed that novel CQD works as a hole acceptor in the junctions, different from the ^{red}CQD as an electron acceptor. Electrons reach the surface of polymers to reduce CO_2 to produce methanol while holes accumulate on CQD to oxidise water. Microwave-assisted CQD shows more favourable water adsorption instead of methanol adsorption compared with polymers, thus facilitating methanol production instead of CO. Therefore, the function of CQD is a key reason for such high selectivity.

III. Impact statement

Sunlight-driven fuel synthesis (*e.g.* water splitting, CO_2 conversion) is a promising solution to current energy and environmental issues by storing solar energy in fuels (*e.g.* hydrogen, methanol). The development of novel semiconductors to utilise photons in the strongest region of the solar spectrum is key to achieve a practical solar to fuel efficiency.

Herein, I have successfully synthesised a group of linker/terminal-controlled polymeric semiconductor photocatalysts which can harvest the UV, visible and near-IR light for hydrogen production from water. Further, the linker/terminal-controlling strategy has been applied to carefully tailor the bandgaps of polymeric semiconductors for enhanced hydrogen and oxygen production. The bandgap-tuneable materials will lead to more advanced applications in photocatalysis. Moreover, such linker-controlled strategy can be extended to the modification of other polymeric photocatalysts and stimulate the fundamental research on the influence of monomer linkers on polymer structure and functions. It will also benefit the

research in organic/polymeric semiconductors, catalysis, solar fuels, solar cells, photochemistry and environmental purification.

I successfully achieved overall water splitting to hydrogen and oxygen as well as CO_2 conversion to methanol under visible light irradiation on the developed polymers. Such discovery would contribute to the sustainable production of fuel and the mitigation of energy and environmental issues to some extent.

IV. Publications and Conferences

1. **Y. Wang,** H. Suzuki, J. Xie, O. Tomita, D. J. Martin, M. Higashi, D. Kong, R. Abe, J. Tang, "Mimicking Natural Photosynthesis: Solar to Renewable H_2 Fuel Synthesis by Z-Scheme Water Splitting Systems", *Chemical Reviews*, **2018**, 118 (10), 5201–5241. DOI: 10.1021/acs.chemrev.7b00286.

2. **Y. Wang,** F. Silveri, M. K. Bayazit, Q. Ruan, Y. Li, J. Xie, C.R.A. Catlow and J. Tang, "Bandgap Engineering of Organic Semiconductors for Highly Efficient Photocatalytic Water Splitting" *Advanced Energy Materials*, **2018**, DOI:10.1002/aenm.201801084.

3. **Y. Wang,** M. K. Bayazit, S. J. A. Moniz, Q. Ruan, C. C. Lau, N. Martsinovich, J. Tang, "Linker-controlled polymeric photocatalyst for highly efficient hydrogen evolution from water", *Energy and Environmental Science*, **2017**, 10, 1643-1651. DOI: 10.1039/C7EE01109A.

4. **Y. Wang,** R. S. Sprick, M. Sachs, M. A. Zwijnenburg, S. J. A. Moniz, R. Godin, J. R. Durrant, A. I. Cooper and J. Tang, "Polymeric photocatalysts for solar driven H_2 synthesis", *Nature Energy*, under review.

5. X. Liu, **Y. Wang (contributed equally)**, X. Han, R. Godin, J. Chen, W. Zhou, C. Jiang, J. F. Thompson, M. K. Bayazit, S. A. Shevlin, J. R. Durrant, Z. Guo, J. Tang, "Ambient condition CO_2 reduction by H_2O to methanol with nearly unity selectivity by carbon-based junction photocatalysts", in preparation.

6. **Y. Wang,** R. Godin, M. K. Bayazit, Q. Ruan, J. R. Durrant and J. Tang, "Metal-free Junctions for Nature-Mimicking Artificial Photosynthesis", in preparation.

7. R. Godin, **Y. Wang,** M. A. Zwijnenburg, J. Tang, J. R. Durrant, "Time-Resolved Spectroscopic Investigation of Charge Trapping in Carbon Nitrides Photocatalysts for Hydrogen Generation", *Journal of the American Chemical Society*, **2017**, 139, 5216-5224. DOI: 10.1021/jacs.7b01547.

8. M. Li, **Y. Wang**, P. Tang, N. Xie, Y. Zhao, X. Liu, G. Hu, J. Xie, Y. Zhao, J. Tang, T. Zhang, D. Ma, "Graphene with Atomic-Level In-Plane Decoration of h-BN Domains for Efficient Photocatalysis", *Chemistry of Materials*, **2017**, 29, 2769-2776. DOI: 10.1021/acs.chemmater.6b04622.

9. Q. Ruan, W. Luo, J. Xie, **Y. Wang,** X. Liu, Z. Bai, C. J. Carmalt, J. Tang, "A Nanojunction Polymer Photoelectrode for Efficient Charge Transport and Separation", *Angewandte Chemie International Edition*,

2017, 56, 8221-8225. https://doi.org/10.1002/anie.201703372.

10. D. Kong, Y. Zheng, M. Kobielusz, Y. Wang, Z. Bai, W. Macyk, X. Wang, J. Tang, "Recent advances in visible light-driven water oxidation and reduction in suspension systems", *Materials Today*, 2018, https://doi.org/10.1016/j.mattod.2018.04.009.

11. Q. Ruan, M. K. Bayazit, K. Vankayala; J. Xie, Y. Wang, J. Tang, Junwang, "Key Factors Dominating Catalytic Performance of g-C3N4 Polymer Photoelectrodes", *Journal of the American Chemical Society,* Submitted.

Conferences

- "Heptazine-based Semiconductors for Artificial Photosynthesis", *Yiou Wang*, East China University of Science and Technology, Shanghai, China, 2018
- "Polymeric Photocatalysts for Water Splitting and CO2 conversion", *Yiou Wang*, Northwestern University, Xi'an, China, 2018
- "Mimicking Natural Photosynthesis: Solar to Renewable Hydrogen from Water Splitting", *Yiou Wang* and Junwang Tang, Oil gas 2018 conference, Dubai, UAE, 2018

- "Organic Semiconductors for Artificial Photosynthesis", ***Yiou Wang*** and Junwang Tang, 22nd International Conference on Photochemical Conversion and Storage of Solar Energy (IPS-22), Hefei, China, 2018
- "Band Gap Engineering of Polymeric Semiconductors for Efficient Photocatalytic Water Splitting." ***Yiou Wang*** and Junwang Tang, Solar Fuel Network Meeting, *York*, 2018
- "Linker-Controlled Polymeric Photocatalyst for Highly Efficient Hydrogen Evolution from Water" ***Yiou Wang,*** Mustafa K. Bayazit, Savio J.A. Moniz, Natalia Martsinovich and Junwang Tang, 2017 MRS Fall Meeting & Exhibit, *Boston*, USA, 2017
- "An Oxygen Rich Polymer Active up to 800 nm for Efficient Photocatalytic H_2 Production from Water" ***Yiou Wang***, Mustafa, K. Bayazit, Savio J.A. Moniz and Junwang Tang, the 16th International Congress on Catalysis (ICC 16), *Beijing,* 2016
- "An Oxygen Rich Carbon Nitride (OCN) for Visible light-driven Hydrogen Production from Water" ***Yiou Wang*** and Junwang Tang, the 4th UK Solar Fuels Symposium, *Cambridge*, 2016

V. Table of Contents

VI. List of Figures

VII. List of Tables

VIII. Nomenclature

Acronyms & initialisms

ADP	adenosine diphosphate
AQY	apparent quantum yield
ATP	adenosine triphosphate
ATR	Attenuated Total Reflectance
BET	Brunauer–Emmett–Teller
CB	Conduction band
CBE	Conduction Band Edge
COF	covalent organic frameworks
CQD	Carbon quantum dots
CTF	covalent triazine frameworks
DCDA	Dicyandiamide
DI	Deionised (water)
DFT	Density functional theory
DOS	density of states
DSC	Differential Scanning Calorimetry
EA	Elemental Analysis
EDX	Energy Dispersive X-ray Spectroscopy
FAT	formic acid treatment polymer
FID	Flame Ionisation Detector
FTIR	Fourier transform infrared spectroscopy
GC	Gas Chromatographs
GCN	Graphitic carbon nitride
GCNN	Graphitic carbon nitride nanosheet
g-C3N4	graphitic carbon nitride
HEP	hydrogen evolution photocatalyst
HER	hydrogen evolution rate
HOMO	Highest Occupied Molecular Orbital
IR	infrared
LED	Light Emitting Diode

LUMO	Lowest Unoccupied Molecular Orbital
MOF	metal-organic framework
NADPH	Nicotinamide adenine dinucleotide phosphate
SEM	Scanning electron microscopy
SHE	normal hydrogen electrode
NMR	nuclear magnetic resonance
OEP	oxygen evolution photocatalyst
OER	oxygen evolution rate
ONLH	oxygen and nitrogen co-linked
OWS	Overall water splitting
PEC	Photoelectrochemical
PRGO	Photoreduced graphene oxide
PSI	Photosystem I
PSII	Photosystem II
PTI	Poly(triazine imide)
PXRD	Powder X-ray diffraction
QD	quantum dots
QY	quantum yield
SSA	Specific Surface Area
SEM	Scanning Electron Microscopy
STH	solar-to-hydrogen
TAS	Transient absorption spectroscopy
TCD	Thermal Conductivity Detector
TEOA	Triethanolamine
TGA	Thermo-Gravimetric Analysis
TOF	Turnover Frequency
TON	Turnover Number
UV-Vis	Ultraviolet-Visible Spectroscopy
VB	valence band
VBE	valence band edge
XPS	X-ray photoelectron spectroscopy

1. Introduction

1.1 Background

Solar to fuel synthesis via artificial photosynthesis (*e.g.* water splitting and CO_2 conversion) has attracted substantial interest over the past half-century as it has the potential to meet the growing global energy demand and provide a solution to the concern about greenhouse gas emission. The solar irradiation hitting the Earth amounts to over 120,000 terawatts per year, while energy consumption will be no more than 30 terawatts per year by 2050 according to non-conservative estimates.[9] As sunlight and water/CO_2 are abundant and essentially inexhaustible, hence there is an opportunity to achieve solar-driven fuel synthesis (*e.g.* H_2 and methanol) on a large scale.[10] Most importantly, economical solar to fuel conversion process needs at least 10% efficiency. Considering almost half of the sunlight on the earth's surface lies in the visible region (400 nm to 750 nm, equal to 3.1 to 1.65 eV), the efficient harvest of visible light photons is one of the key challenges to fulfil the 10% energy conversion efficiency requirement.[11]

Therefore, to develop a visible light-driven photocatalytic system has become the significant target recently.

Since the discovery of Honda-Fujishima effect in 1972, many efforts have been made to discover a single visible light-driven photocatalyst, on which both proton reduction and water oxidation reactions should take place efficiently.[12-13] Few materials have been successfully developed for overall water splitting (OWS) to H_2 and CO_2 conversion to fuel due to chemical constraints required. The bandgap of the photocatalyst must be relatively small to enable the absorption of a wide wavelength range of visible light. Meanwhile it should also be adequately positioned so that the conduction band (CB) is negative enough in terms of potential to reduce protons (0 eV vs SHE), or CO_2 (-0.58 to -0.24 eV vs SHE), and the valence band (VB) is positive enough to oxidise water (+1.23 eV vs SHE). It requires technological advances to achieve this potential.

However, it seems to be very challenging to achieve overall water splitting or CO_2 conversion on a single photocatalyst. So far, most reported visible light-driven photocatalysts are only efficient for either proton/CO_2 reduction or water oxidation half reaction because the

combination of both bandgap magnitude and band positions is quite difficult to achieve. On the one hand, considering the required overpotential (usually > *ca.* 0.5 eV each in the absence of external bias) for sufficient driving force, the bandgap for a single photocatalyst is usually larger than *ca.* 2.3 eV.[14] Such a wide bandgap limits the utilisation of photons above 550 nm thus hindering a high solar to fuel efficiency. The difficulty in altering the band positions of single photocatalysts is very large hence to achieve 10% solar to fuel efficiency artificial photosynthesis on a single photocatalyst remains a holy grail after decades of investigation. On the other hand, both overall water splitting and CO_2 conversion involve multi-charge process, which requires relatively long lifetime electrons and holes to complete the reaction competing with the recombination. Therefore, a system is highly desired to take advantage of narrow bandgap semiconductors and apply effective charge separation strategies.

Z-scheme system

Different from the idea of solar fuel synthesis by a single photocatalyst, nature applies a two-stage, double-excitation process (named as Z-scheme) in natural photosynthesis. A Z-scheme system is

composed of two half reactions: proton reduction and water oxidation (Scheme 1). A water splitting system based on single photocatalyst usually needs one wide bandgap materials to fulfil the requirement of redox potential (1.23 eV) and overpotential (approximately 0.5 eV each) for both H_2 and O_2 evolution reactions, thus limiting the optical window to a small region in the solar spectrum. However, a double excitation system allows the use of two narrow bandgap materials, which could utilise more photons in the visible region of the solar spectrum, because each of them only needs to work for a half reaction. There is of significant interest in renewable solar fuel synthesis via a robust and

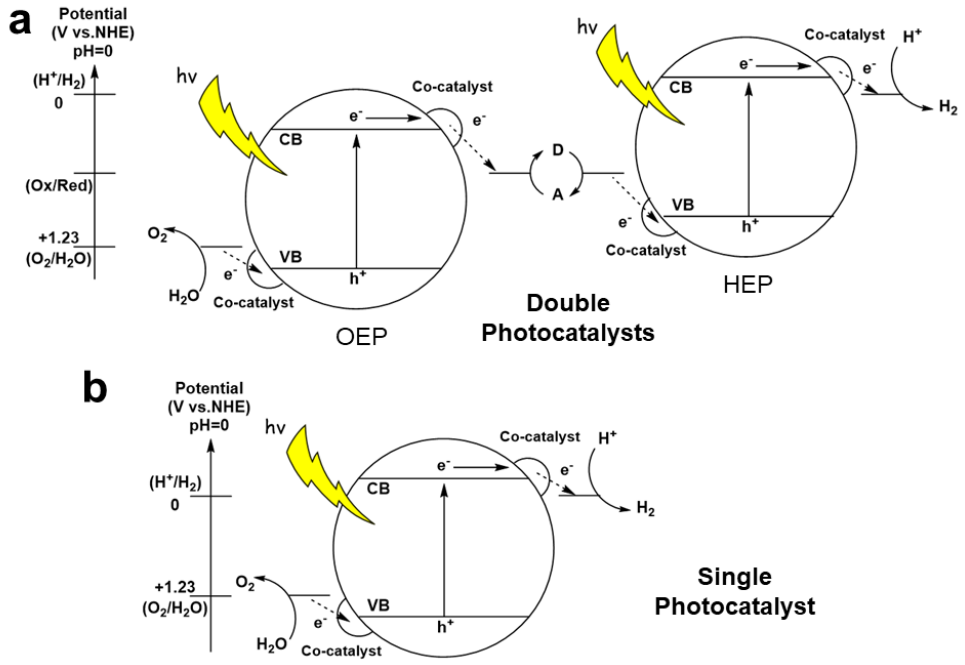

Scheme 1. Water splitting systems based on (a) double photocatalysts (Z-scheme) and (b) single photocatalyst.

economic two-photocatalyst system against a single photocatalyst because the former has a theoretical 40 % solar to fuel conversion efficiency, which is higher than the latter (max. 30% efficiency).[15-17]

Taking photocatalytic water splitting as an example, inspired by natural photosynthesis of green plants, an inorganic analogue to natural Z-scheme was firstly constructed to achieve artificial photosynthesis by coupling two narrow bandgap semiconductors, an oxygen evolution photocatalyst (OEP) with a hydrogen evolution photocatalyst (HEP) connected via an electron mediator, which has developed very fast over the past 10 years. On the one hand, photoexcited electrons in the conduction band (CB) of a HEP reduce water and holes in the valence band (VB) of the OEP oxidise water, evolving H_2 and O_2 separately on different photocatalysts.

On the other hand, the CB electrons of the OEP can pass through a relay/shuttle to combine with holes on the valence band of the HEP thus completing the cycle and maintaining charge neutrality. Overall water splitting using Z-schemes reactions require three conditions; (a) an OEP which can inject electrons to acceptors, (b) a HEP that can accept electrons from donors, (c) an electron relay system with suitable potentials where subsequent back reactions are suppressed. In such

dual photocatalyst systems, both OEP and HEP could be narrow bandgap photocatalysts driven by visible light. Thus a large portion of visible photons in the solar spectrum can be utilised to achieve high energy conversion efficiency.

Moreover, the strategy of using Z-scheme has a large degree of flexibility and can utilise a large library of reported half reaction photocatalysts. So, it's much more applicable than a single photocatalyst system for the final target. For this reason, my research project will concentrate on the discovery of efficient candidate photocatalyst for visible light-driven Z-scheme water splitting.

In a Z-scheme system, both water reduction and oxidation photocatalysts are crucial. A narrow bandgap photocatalyst can promise a very high solar energy conversion efficiency provided the other photocatalyst can be matched. Therefore, substantial efforts have been put into searching for a narrow bandgap photocatalyst only active for half reaction. In general, the design and synthesis of efficient semiconductor photocatalysts are deemed the primary target. It should firstly meet the thermodynamic band position requirement for water splitting where a conduction band (CB) position more negative than the H_2 redox potential (0 V *vs* Standard Hydrogen Electrode, SHE, pH = 0)

and a valence band (VB) more positive than the O_2 redox potential (1.23 V *vs* SHE, pH = 0), in addition to being chemically stable and reasonably low-cost.[18]

Polymeric photocatalysts: *e.g.* g-C_3N_4

As mentioned above, a method to harvest the visible photons (400 nm to 750 nm) adequately is among one of the biggest challenges to be overcome to turn the overall water splitting concept into a device.[11] In other words, a system comprising narrow bandgap, low-cost and earth-abundant photocatalysts with an at least 10% solar-to-hydrogen (STH) energy conversion efficiency is commercially required.[19] Four decades of extensive exploration into inorganic semiconductor photocatalysts, particularly metal oxides, has demonstrated that the tuning of their structures for efficient visible light harvesting is very challenging due to their low processability.[20] To the best of my knowledge, polymeric photocatalysts are one of the most promising candidates to fulfil such requirements due to their low cost and ease of modification to meet the band positions requirements.

For many organic semiconductors, such as polymers which possess better tunability, the issue of poor long-term stability remains a key

shortcoming.[21] The stability issue was addressed in part by the discovery that the semiconducting polymeric graphitic carbon nitride (g-C_3N_4) could stably produce H_2 from water under visible light, due to its suitable CB position for water reduction coupled with outstanding chemical stability and relatively narrow bandgap.[22] G-C_3N_4 is thus a seminal example of stable half reaction by a polymer which has since stimulated the investigation of polymeric semiconductors in solar fuel synthesis. The attraction of such materials for solar energy conversion has been widespread. According to the *Web of Science*, approximately 2500 since 2009 were reported related to polymeric photocatalysts. As stated above, the most significant advantage of polymeric semiconductors is their facile structural tunability compared to traditional inorganic materials, which allows the possibility of creating a family of excellent photocatalysts by tuning their photophysical properties via the ease modification of structure.

Besides g-C_3N_4, a whole family of photo-sensitive organic polymers have been developed, including pyrene-based conjugated microporous polymers (CMPs), covalent triazine frameworks (CTFs), covalent organic frameworks (COFs), and planarized-fluorinated conjugated polymers, to name a few.[23-26] These polymeric

photocatalysts show sound potential to be used for both water oxidation and reduction and will be mentioned in my papers. But more importantly, to date, no single polymer for half reactions has been able to possess an absorption that matches well with the solar spectrum to exhibit activity at long wavelengths (such as beyond 600 nm), which hinders the overall efficiency of the process.[27]

1.2 Motivation, aim and objectives

As discussed above, the most promising way to achieve meaningful solar fuel synthesis (*e.g.* solar water splitting, CO_2 conversion) is to use the Z-scheme system instead of a single photocatalyst system. In such an efficient dual-photocatalyst system, the bandgap of both HEP and OEP should be relatively narrow so that a large portion of visible photons could be utilised for photocatalysis. At the same time, the photocatalysts need to be highly efficient. Considering the difficulty in altering inorganic photocatalysts' structure for proper bandgaps and efficient charge separation, the modification of polymeric photocatalysts' structure is surely more feasible providing the good stability is maintained. However, the advantage of outstanding tunability of polymeric photocatalysts hasn't been taken

yet. Thus long wavelength active polymeric photocatalysts are a heavy shortage.

I aim to develop a strategy to tune the bandgap of low-cost polymeric photocatalysts towards a narrow one that well matches the solar spectrum in the visible region for stable and highly efficient solar fuel synthesis. Further, I plan to apply these polymers in overall water splitting and CO_2 conversion.

The key objectives include 1) to develop a novel narrow bandgap polymeric photocatalyst for H_2 production; 2) to develop a strategy to stepwise tune the bandgap polymeric photocatalysts for both H_2 and O_2 production; 3) application of these novel polymers in water splitting; 4) application of these novel polymers in combination of water splitting and CO_2 conversion.

1.3 Structure of the thesis

There will be seven chapters in this thesis, focusing on visible light-driven heptazine-based polymeric photocatalysts for water splitting and CO_2 conversion. Briefly, after the brief introduction of Chapter 1, Chapter 2 firstly review the latest advancements in visible light-driven Z-scheme for water splitting through oxidation and reduction

photocatalysts and various strategies applied. Then it reviews the development of polymeric photocatalysts focusing on g-C_3N_4, which is among the most promising ones to produce H_2 and to be applied in a Z-scheme as a reduction photocatalyst. In Chapter 3, it would first introduce the methods of synthesis, characterisations and computing used in the following studies. Afterwards, in Chapter 4, the linker-controlled polymeric photocatalysts will be described for efficient H_2 production and water splitting via Z-scheme. The structure of this new polymer would be identified, and the reasons for enhanced performance in visible light absorption and efficiency would be proposed corresponding to experimental and computational results. In Chapter 5, I discuss another method of stepwise controlling the linkers in polymeric photocatalysts according to the strategy developed in Chapter 4 for both hydrogen and oxygen production. Further, following the successful development of polymeric photocatalysts, in Chapter 6 I report efficient junctions for photocatalytic CO_2 conversion. The last Chapter summarises the key conclusions and proposes future work.

The theoretical modelling in Chapter 4 was calculated by my collaborator Dr. Natalia Martsinovich. The theoretical calculations in Chapter 5 were done by my collaborator Fabrizio Silveri and Prof. C.

Richard. A. Catlow. The theoretical modelling results in Chapter 6 were carried out by my collaborator Dr. Xiaoyu Han and Prof. Zhengxiao Guo. The TAS measurements were carried out by Dr. Robert Godin and Prof. James Durrant.

2. Literature survey

This project focuses on polymeric photocatalysts for solar fuel synthesis. Therefore the following only reviews the recent progress of polymeric photocatalysts and their applications in water splitting and CO_2 conversion. Some contents in this chapter are reproduced with permission from my own published work ref. 105. Copyright 2018 American Chemical Society.

2.1 Mechanism of water splitting

The earliest demonstration of photo-assisted water splitting dates back to 1921, reported by Baur & Rebmann using UV light and a AgCl/TlCl system in pure water.[28] Since the discovery of Honda-Fujishima effect in 1972, many efforts have been made in the search for a single photocatalyst, where both proton reduction and water oxidation reactions should take place concurrently at different sites.[12-13] Such a single photocatalyst system is shown in Figure 1, where a semiconductor material can absorb photons with energy greater or equal to the band gap, thus exciting electrons from the valence band (VB) into the conduction band (CB), leaving positively charged holes in

the valence band. The overall water splitting process requires a positive Gibbs free energy ($H_2O \rightarrow H_2 + 0.5\ O_2$, $\Delta G^0 = 237.13$ kJ/mol) and thus cannot occur spontaneously. Photogenerated electrons and holes can have strong reduction and oxidation potentials and can be used for catalytic surface redox reactions, *e.g.* water splitting.[10] Water splitting requires two electrons or four holes to evolve one mole of H_2 or O_2, respectively. The CBM of semiconductors must be more negative than the reduction potential of H^+/H_2 (0 V vs Standard Hydrogen Electrode (SHE) at pH 0), and the VBM must be more positive than the oxidation potential of O_2/H_2O (+1.23 V vs SHE at pH 0). Therefore, the theoretical minimum requirement of photon energy is 1.23 eV, which corresponds to a wavelength in the range of approximately 1000 nm and is in the near-infrared range. However, activation energy (overpotential) is necessary to overcome the energy barrier of redox reactions between charge carriers and water molecules. Therefore, the band gap of a photocatalyst should be larger than the minimum requirement of 1.23 eV. Hence, the suitable size of band gaps and the positions of conduction band minimum (CBM) and valence band maximum (VBM) are the most important aspects for overall water splitting. In terms of solar spectrum, 52%-55% sunlight at Earth's surface is infrared light

(above 700 nm), 42%-43% visible light (400 – 700 nm) and 3%-5% ultraviolet light (below 400 nm).[29] Therefore, to achieve a reasonable efficiency of the overall water splitting reaction, the bandgap of photocatalysts should be narrower than 3.1 eV to utilise more visible light energy from the solar spectrum and also possess a large enough overpotential. As for some sulphides and nitrides with suitable bandgap potentials for overall water splitting, many of them are not stable in an overall water splitting reaction due to self-oxidation.[30-31] For example, most (oxy)nitrides with the introduction of N 2p orbital in the VB formation undergo self-oxidative deactivation to some degree, in which photogenerated holes oxidise N^{3-} to N_2 ($2N^{3-} + 6h^+ \rightarrow N_2$). Self-oxidative deactivation proceeds competitively, and in some cases even when appropriate cocatalysts are used, the water-splitting rate gradually decreases as the compound decomposes. As for some materials with narrower band gaps, such as the ground-breaking example of GaN-ZnO solid solution (2.5 eV), which could split water into H_2 and O_2 under visible light, the efficiency was still unsatisfactory (average quantum efficiency of 0.14% in the range of 300 to 480 nm).[32] So far, only a few examples of overall water splitting by a single

photocatalyst system under visible-light irradiation exist in literature, such as GaN:ZnO solid solutions[32], nitrides,[33] sulfides[34], and g-C_3N_4.[35]

The majority of reported visible light-driven photocatalysts are only effective for the half reactions of either proton reduction or water oxidation, as the combination of both bandgap magnitude and positioning is difficult to engineer.[36-37]

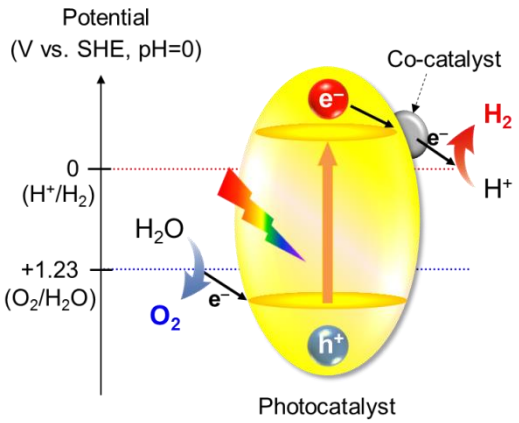

Figure 1. A typical model of a single photocatalyst system for water splitting

2.2 Graphitic carbon nitride (g-C_3N_4)-based photocatalysts for H_2 production half reaction

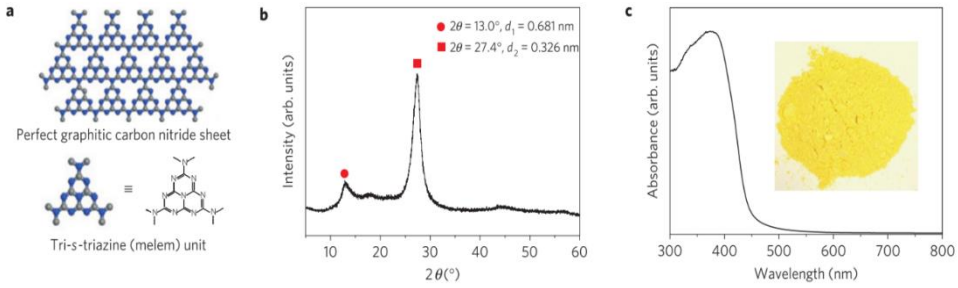

Figure 2. Crystal structure and optical properties of graphitic carbon nitride. (a) Schematic diagram of a perfect graphitic carbon nitride sheet constructed from heptazine units. (b) Experimental XRD pattern of the polymeric carbon nitride, revealing a graphitic structure with an interplanar stacking distance of aromatic units of 0.326nm. (c) Ultraviolet–visible diffuse reflectance spectrum of the polymeric carbon nitride. Inset: Photograph of the photocatalyst. Reproduced with permission from ref. 22. Copyright 2009 Macmillan Publishers Limited.

Apart from crystalline inorganic semiconductors, which have been well studied since the discovery of the Fujishima-Honda effect in the early 1970s, polymeric semiconductors have attracted increasing attention since graphitic carbon nitride (g-C_3N_4) (Figure 2) was reported for visible light-driven photocatalytic hydrogen production.[22, 38] Carbon nitrides are a family of triazine-based polymers, typically with idealised composition C_3N_4, although in practice many carbon nitride materials also contain a significant amount of hydrogen. The strictly denoted carbon nitride materials are often referred to as graphitic carbon nitride,

named after the likely crystalline structure of C_3N_4, but in practice, most materials of relevance to photocatalysis will probably be based on the melon polymer[39-40] and poorly-crystalline.[41] The latter is a linear polymer formed of heptazine units linked through amine (–NH-) bridges with the solid-state structure stabilised by hydrogen bonds involving the amine groups. Alternatively, samples prepared using molten salt as solvent yield the crystalline layered poly(triazine imide) structure in which some of the salt ions are incorporated (Figure 3).

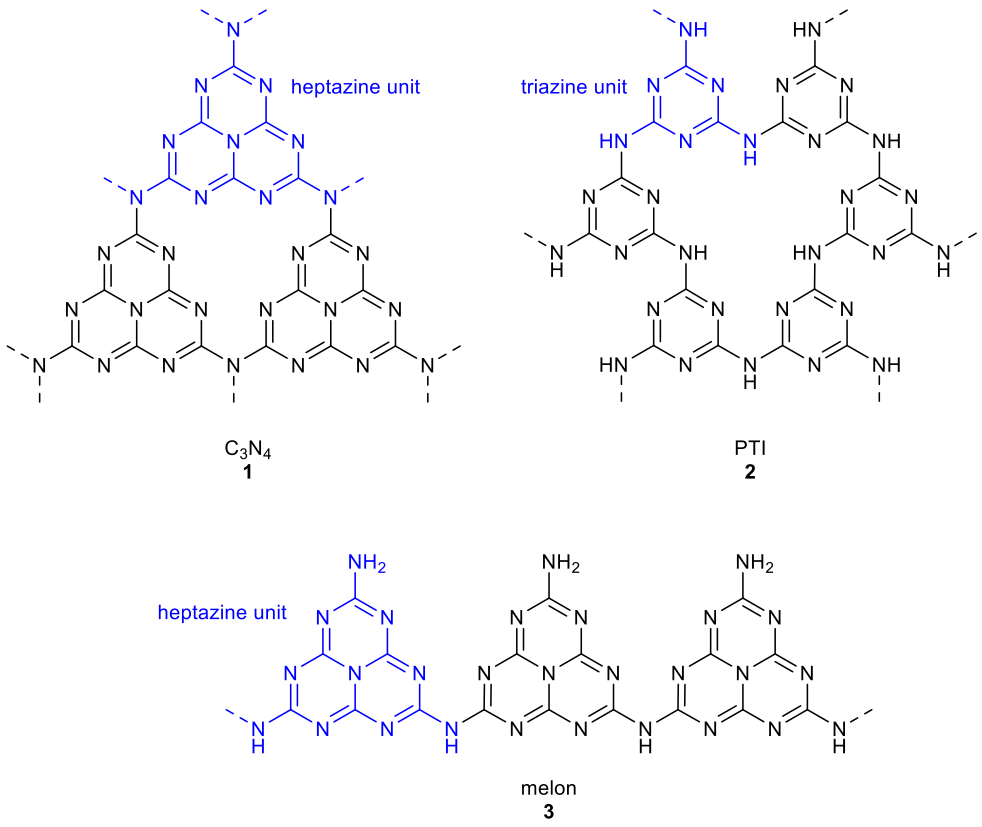

Figure 3. Structures of the different possible carbon nitride materials (heptazine subunit highlighted in blue.

G-C_3N_4 composed of ordered heptazine units has been reported to have a relatively small bandgap of 2.7~2.9 eV, with a negative enough CB position(at -1.4 eV vs SHE at pH = 0) to drive electrons to reduce protons to hydrogen.[42] Composed of extremely abundant elements, graphitic carbon nitride is low-cost, robust and nontoxic. However, as g-C_3N_4 was only used as a photocatalyst since 2009, efficiencies are still relatively low for H_2 production and the responsive wavelength range is limited to 460 nm. Consequently, many strategies have since been employed to improve the compound regarding performance and durability. Precursors including urea, melamine, dicyandiamide, thiourea have been found to be able to produce g-C_3N_4 by simple pyrolysis in various atmospheres, including air.[38] Elemental doping of P, B, F, I, S, O and N were also examined.[6, 43-48] Other methods such as nanostructure design and molecular incorporation were also applied herein to enhance the moderate performance.[49-50] However, only a few groups have succeeded in coupling the g-C_3N_4 in Z-scheme water splitting.

Table 1 summarises the most promising examples of high-efficiency carbon nitride materials reported for H_2 evolution in the literature to date. In all these systems, a TEOA hole scavenger and a

certain % weight loading of Pt co-catalyst (usually by photodeposition) are required. As for the modification of carbon nitride, on the one hand, to promote the charge separation thus achieving high quantum efficiency at certain wavelengths (*e.g.* 420 nm), strategies such as increasing the degree of polymerisation, nanosheet fabrication, treatment in molten salts, *etc.*, have been developed. On the other hand, to correlate with the strongest region of the solar spectrum, strategies such as selective doping, copolymerisation, the introduction of defects, *etc.* have narrowed the intrinsic bandgap of carbon nitride (2.7-2.8 eV) to harvest more visible photons. Recently Tang's group found that carefully tuning the structure of g-C_3N_4 through controlling the degree of polymerisation, a dramatic enhancement in efficiency was observed. As the degree of polymerisation increased, and the proton concentration decreased, the HER rose because the CB position exhibited a pronounced negative shift and charge separation was enhanced from DFT calculations, resulting into a 26% AQY at 400 nm.[38] Given the knowledge of the structural similarity between graphene and graphitic carbon nitride, studies of a few-layer C_3N_4 have recently attracted much attention. Through direct calcination in air, sonication in different solvents (*e.g.* IPA, H_2O, NMP, ethanol, acetone) or *via* a gas-

template approach, nanosheets g-C_3N_4 could be synthesised with promoted photoactivity. Interestingly, instead of tuning the bulk structure, changing the surface property using an additive, *eg.* K_2HPO_4 was also found to be helpful for charge separation.[51] Electrochemistry revealed the additive promotes TEOA oxidation by photo holes which allowed more efficient proton reduction, indicating hole transport might be one barrier limiting its activity. There is also an s-triazine-based g-C_3N_4 (PTI/Li^+Cl) with the melted salt stabilising its structure and acts as a solvent, resulting into an AQY of 7% at 420 nm with compatible 2,4,6-triaminopyrimidine (TAP) dopants. Likely, its optical window was broadened by increased π-electron delocalisation introduced by TAP, and the HER increased due to the well-condensed structure.[52] The terminal cyanamide groups introduced via a KSCN-treated method were believed to improve activity due to the fast *in-situ* electron transfer to co-catalyst and enhanced separation that arises from the potential difference within the polymer structure, resulting in an AQY of 9.3% at 400 nm with methanol as an electron donor .[53]

The other approach is *via* elementary doping with boron, fluorine, iodine, sulfur, nitrogen and phosphorus, which can extend the absorption into the visible region, resulting in a smaller bandgap and a

more favourable CB position for proton reduction.[6, 54-57] For example, in phosphorus-doped C_3N_4, the altered electronic structure led to higher conductivity, narrower bandgap and suppressed recombination, resulting in an AQY of 5.8%. The bandgap of g-C_3N_4 could also be tuned by coupling with foreign aromatic or aliphatic monomers (barbituric acid or amino cyano moieties); the resultant HER of the optimised materials increased by 4 and 7-fold respectively.[58-59] The activity declined when an excess of foreign monomers was used which were likely acting as recombination sites. Also, PEC measurements and theoretical calculations revealed that charge separation and transfer could be accelerated *via* the incorporation of aromatics containing amino and cyano groups at the ortho positions. Decreasing the size of g-C_3N_4 particles to quantum dot (QD) dimensions could also aid light absorption because of strong quantum confinement effects and high surface area, resulting in a HER *ca.* 7 times higher than bare g-C_3N_4 and crucially, absorption of photons greater than 600 nm. Reducing the crystallinity extended the overall absorption to 600 nm and reduced charge recombination due to its disordered structure.[60-61] Other strategies such as metal-ligand effects and introduction of carbon quantum dots as sensitisers also have been reported to broaden the

optical window above 600 nm.[27, 62] However, most of these absorption-enhanced samples have very low or unreported AQY.

The absolute HER is highly dependent on the experimental setup. For example, vacuum conditions, phosphate environment, optimum sacrificial regents are all significantly favourable to high activity. Therefore, it is fair to compare the activity by AQY under identical and reported conditions. So far, the benchmark AQY of 60% at 420 nm on carbon nitride is the urea-derived one treated in molten salts[63], although the absorption edge is below 500 nm. Recently, a few carbon nitrides with controlled terminal groups, including cyanamide, urea and hydroxyl species, have demonstrated boosting HER, suggesting that terminals in carbon nitride structure play a special role in HER. Briefly, effective approaches should be developed to both enlarge the optical window (but maintain the stability and enough driving force) and enhance charge separation of carbon nitrides by tailoring the polymerisation pathway under the guidance of theoretical prediction or charge kinetic knowledge from cutting-edge spectroscopies.

Table 1. Comparison of absorption and apparent quantum yield (AQY) of exemplary g-C_3N_4 photocatalysts

#	Properties	Absorption edge[a]		AQY[d] [%]	HER / OER[e] [μmol h^{-1} g^{-1}]	Light source		Conditions[f]	Ref.
		λ_{edge} [nm]	E_{gap} [eV]			Power [W]	Filter [nm]		
1	Highly-polymerised	415	3.0	26.5@400nm, 12.5@420nm	H_2:3327, no O_2	300 (Xe)	> 395	TEOA	[38]
2	Nanosheets	472	2.6	3.75% @ 420 nm	H_2:1860, no O_2	300 (Xe)	> 420	TEOA vacuum	[64]
3	g-C_3N_4 nanosheets	460	2.7	45.7@380nm, 26.1@420nm	H_2:18940, no O_2	300 (Xe)	> 400	0.20 mol K_2HPO_4, vacuum	[51]
4	PTI/Li^+Cl^-	600	2.1	15@400nm, 7@420nm	H_2:8160, no O_2	300 (Xe)	> 420	Vacuum	[52]
5	Heated melamine (salt melt method)	450	2.8	50.7@405nm	H_2:15400, no O_2	300 (Xe)	> 400	0.01 mol K_2HPO_4, vacuum	[65]
6	Cyanamide defects	500	2.5	9.3@400nm	H_2:1235, no O_2	300 (Xe)	AM 1.5	methanol	[53]
7	P-doping	487	2.5	5.8@420nm	H_2:670, no O_2	300 (Xe)	> 420	TEOA	[54]
8	N-doping	477	2.6	N/A	H_2:554, no O_2	300 (Xe)	> 400	TEOA	[55]
9	H_2O_2 treated	498	2.5	N/A	H_2:375, no O_2	300 (Xe	> 420	TEOA	[6]
10	B-doping	600	2.1	N/A	H_2:510, no O_2	300 (Xe)	> 420	TEOA	[56]
11	F-doping	472	2.6	N/A	H_2:130, no O_2	500 (Xe)	> 420	TEA, vacuum	[57]
12	Barbituric acid copolymerisation	486	2.6	N/A	H_2:294, no O_2	300 (Xe)	> 420	TEOA, vacuum	[59]

13	Aminobenzonitrile copolymerisation	525	2.4	N/A	H_2:1470, no O_2	300 (Xe)	> 420	TEOA, vacuum	[58]
14	g-C_3N_4 QDs	650	1.9	N/A	H_2:2757, no O_2	300 (Xe)	> 420	TEOA	[66]
15	Amorphous	682	1.8	N/A	H_2:3158, no O_2	300 (Xe)	> 440	TEOA	[60]
16	Linker controlled	800	1.5	10.3@420 nm, 2.1@500 nm	H_2:1020, no O_2	300 (Xe)	>420, 120 mW/cm^2	TEOA	[67]
17	Formic acid treated	650	1.9	H_2: 8.6%/2.5% at 420/500 nm, O_2: 4.3%/1.0% at 420/500	H_2:772, O_2: 120	300 (Xe)	420-710, 100 mW/cm^2	TEOA	
18	Alkali-Assisted Nitrogen Deficient	525	2.4	N/A	H_2:6900, no O_2	300 (Xe)	>420	25 vol% aqueous lactic acid	[68]
19	Crystalline Nanosheets	435	2.9	8.6@420nm	H_2:1060	300 (Xe)	>420	10% methanol	[69]
20	Steam Reforming nanosheets	441	2.8	11.3@405nm	H_2:5222	300 (Xe)	>420	TEOA, vacuum	[70]
21	Co-condensation and calcination in molten salt	484	2.6	57@420 nm	H_2:3000	50 LED	White LED, >420	TEOA, vacuum	[71]
22	Post-calcination in molten salts	481	2.6	60@420 nm	H_2:11720, O_2:300	50 LED	White LED, >420	TEOA, vacuum, 3 wt % NaCl	[63]

Heterojunctions

Besides extensive work on carbon nitride on its own, there are also a large number of studies in which carbon nitride is combined with a generally inorganic material in the form of a heterojunction or Z-scheme with an aim to reduce charge recombination.[72-89] Compared to proton reduction much less work has been reported on the use of carbon nitride for water oxidation and overall water splitting, something most likely due to the inherent challenges of water oxidation that I discuss in more details below. Work on carbon nitride in this area can be subdivided in two: carbon nitride in combination with an inorganic or polymer material and on itself providing proper cocatalysts.

The major limiting factors affecting the efficiency of g-C_3N_4 and related polymeric photocatalysts involve low carrier mobility and high bulk recombination. Recombination may be suppressed by utilising scavengers, and economically by a heterojunction, whereby charge-carriers are generated in one photocatalyst and subsequently vectorially transferred to the other material (photocatalyst/electrocatalyst) allowing for long-lived electron-hole pairs, mimicking the mechanism exhibited in Photosystem II during artificial photosynthesis (Figure 4).[18] Numerous Type II junctions

involving g-C_3N_4 have been recently summarised in by Ong *et al.*[90] In this section I will describe the most promising heterojunction composites involving g-C_3N_4 for photocatalytic water splitting.

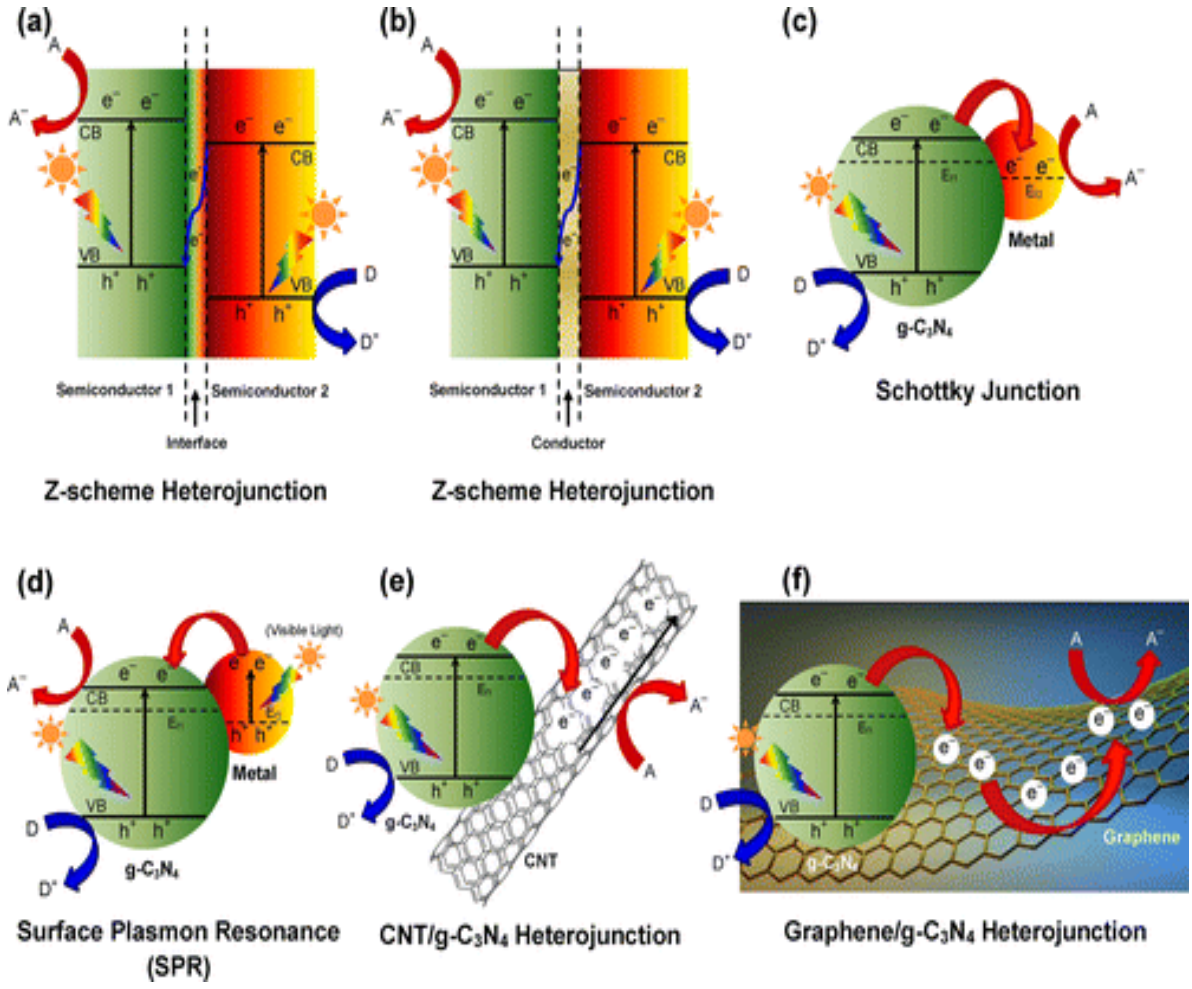

Figure 4. Schematic illustration of the transfer of photoinduced charge carriers for various types of heterojunction nanocomposites: (a) Semiconductor–semiconductor Z-scheme heterojunction, (b) semiconductor–conductor–semiconductor Z-scheme heterojunction, (c) Schottky junction of metal/g-C_3N_4 nanohybrids, (d) SPR in noble metal/g-C_3N_4 nanohybrids, (e) CNT/g-C_3N_4 heterojunction, and (f) graphene/g-C3N4 heterojunction. A, D, and E_f denote electron acceptor, electron donor, and Fermi level, respectively. If one looks closely, the function of (c), (e) and (f) are mostly the same.

A g-C_3N_4/WO_3 junction composite exhibited a remarkable 2-fold increase in efficiency for H_2 evolution from water, attributed to its high surface area and the synergetic effect of both materials which led to charge transfer, akin to a solid-state Z-scheme (Figure 4.a and b).[72] In another report, by combining sulfur-doped g-C_3N_4 with the well-known water oxidation photocatalyst $BiVO_4$, an oxygen evolution rate (OER) of *ca.*750 μmol $h^{-1}g^{-1}$ was exhibited, more than double that of pure $BiVO_4$, however, details of the charge transfer mechanism were not given.[73] As a visible absorber, g-C_3N_4 has been coupled with many wide-bandgap semiconductors to improve solar harvesting. For example, g-C_3N_4–$SrTiO_3$: Rh evolved 223.3 μmol h^{-1} of H_2 under visible irradiation, over three times that of $SrTiO_2$: Rh.[74] A C_3N_4/TiO_2 junction was found to double H_2 evolution compared to pure C_3N_4 under visible irradiation.[75] Because the CB edge of g-C_3N_4 (*ca.* −1.13 eV) is more negative than TiO_2 (−0.29 eV), photogenerated electrons from g-C_3N_4 transfer easily to TiO_2, thus helping charge separation.[76] Visible light-responsive g-C_3N_4/$NaNbO_3$ nanowires exhibited remarkably enhanced visible light-driven activity for CO_2 photo-reduction to CH_4,[91] whilst coupling g-C_3N_4 with plasmatic Au and SnO_2 led to efficient H_2 evolution without any co-catalyst (Figure 4d).[77] Here, photo-electrons

transferred to SnO_2 from g-C_3N_4; the function of the Au was to absorb longer wavelengths of light (up to 520 nm) and inject electrons into SnO_2 for proton reduction. However, the AQY of the ternary system was not reported and nor is plasmatic enhancement generally not well understood; it is unlikely to be cost-effective. Through a similar mechanism, a g-C_3N_4 coated $SrTiO_3$ displayed a high hydrogen evolution rate of 440 $\mu mol\, h^{-1}\, g^{-1}$ under visible irradiation due to electron transfer from the CB of C_3N_4 to that of $SrTiO_3$ followed by migration to the Pt co-catalyst.[78] A 1.1% NiS/C_3N_4 composite has also shown an appreciable activity for H_2 production from water,[79-80] whilst similarly, the use of NiS_2 as co-catalyst for H_2 production on g-C_3N_4 has recently been reported.[81] The coupling of high surface area g-C_3N_4 with Ta_3N_5 has also resulted in enhanced visible light-driven H_2 evolution[82], and g-C_3N_4-CdS QDs composites improved the H_2 production over bare g-C_3N_4 by more than 9 times due to *in-situ* electron transfer to CdS, however the photocurrent recorded was actually quite small,[83] with a similar mechanism reported for C_3N_4/CdS core-shell nanowires.[84] Addition of a bifunctional $Ni(OH)_2$ surface catalyst instead of Pt was found to dramatically increase the HER of CdS/g-C_3N_4 by 26 times due to the electron transfer from g-C_3N_4 to

CdS then to $Ni(OH)_2$ and ability of $Ni(OH)_2$ to accept photogenerated electrons for H_2 evolution easily. [85]

Carbon-based electron acceptors such as graphene, carbon nanotubes *etc.* also facilitate more efficient charge separation due to their high electronic conductivity brought about by their π-conjugated structures (Figure 4 e-f).[88] For example, g-C_3N_4/graphene composites exhibited a 3-fold enhancement in H_2 production under visible light compared to bare g-C_3N_4.[86] Photoluminescence (PL) measurements confirmed quenching of luminescence in the junction; the mechanism for the enhancement was down to the ability of graphene to act as conductive channels to efficiently separate the photogenerated charge carriers, while a similar mechanism was proposed in a red phosphorus/C_3N_4 junction.[92] As indicated by Figure 4 e, multi-walled carbon nanotubes have also been employed in a similar manner with g-C_3N_4 for efficient H_2 evolution, resulting in a 3-fold increase in activity compared to pure g-C_3N_4.[87-88] A quasi-polymeric junctions incorporating a wide bandgap Pt-loaded Zr-based metal-organic framework (MOF) UiO-66 coupled to Pt-g-C_3N_4 exhibited also enhanced visible light-driven H_2 evolution due to efficient electron transfer into the MOF.[89] Furthermore, homojunction incorporating

differing crystal phases of g-C_3N_4 has been proposed however the overall hydrogen evolution rate remains lower than that of the other all-carbon-based junctions already mentioned.[93]

There are main advancements in the field of g-C_3N_4 photocatalysts. However, one of the key issues to fairly assess and compare the activity of a polymer is the measurement of an AQY instead of HER, which is highly influenced by the intensity and spectrum of the light source. Unfortunately, in most cases the AQY was either extremely low or not reported, suggesting more work is still needed to improve the activity, especially into the visible region. Although visible-light absorption increased remarkably in such cases, even into the near-IR, AQY was not reported above 420 nm. Also, despite its popularity, there are very few reports describing the photoelectrochemical properties of g-C_3N_4-based electrodes given the widespread interest in the material for photo-driven fuels synthesis. The fewer reports of g-C_3N_4 electrodes are likely due to the inherent difficulty growing high-quality thin films, as the highest photoanodic currents are only achieving tens of μA/cm^2 at 1.23V *vs* RHE.[94]

2.3. Polymeric photocatalysts for O_2 production half reaction

The O_2/H_2O potential lies at +1.23 V (vs SHE at pH 0). However, due to the required overpotential of the chemical reaction, it usually requires a more positive VBM position such as *ca.*+1.9 V (vs SHE at pH 0) to achieve gaseous oxygen production.[95] Oxygen generation from water splitting is a very slow procedure because it requires four holes to form one molecule of O_2 while H_2 production only needs two electrons. Subsequently, electrons transfer much faster than holes in most oxide photocatalysts which are n-type semiconductors, so the process is much more facile.[96] Therefore, a large driving force has to be provided by a deep VBM of a semiconductor. A consequence of this deep-lying VBM, a problem in the majority of metal oxides, is that this makes the bandgap very large, so a large portion of the visible spectrum from sunlight cannot be sufficiently harvested.[42] Only a few metal oxides have been reported to work under visible irradiation for efficient half reactions (O_2 evolution), for example, monoclinic $BiVO_4$ (~2.4 eV)[97], WO_3 (~2.7 eV)[25] and Ag_3PO_4 (2.6 eV)[98].

Compared to the progress in polymeric photocatalysts for hydrogen production, much fewer polymeric photocatalysts have been reported for oxygen production so far. Generally, polymers hardly produce O_2 in the absence of co-catalyst. The first O_2 production polymer is the pristine graphitic carbon nitride, which was shown to produce oxygen from water under visible light in the presence of sacrificial scavenger and RuO_x cocatalyst as reported in 2009, albeit it less efficiently and overall water splitting was not demonstrated at that time.[22] Zhang *et al.* reported the integration of Co_3O_4 nanoparticles within graphitic carbon nitride to construct a nanohybrid photocatalyst for the photocatalytic generation of oxygen from water, achieving an apparent quantum efficiency of 1.1% at 420 nm for water splitting to oxygen. Perhaps the most remarkable example of pure water splitting is the carbon nitride/carbon quantum dots (QDs) composite reported by Liu *et al.*[99] Because H_2O_2 formation is more thermodynamically favourable on carbon nitride than O_2 evolution,[100] the authors suggested that QDs were needed to facilitate charge separation and decompose peroxide to molecular oxygen, while the carbon nitride can photocatalytically evolve hydrogen. This step-wise two-electron process bypasses the slow four hole kinetics usually attributed to the

OER, leading to a remarkable STH of 2%, although it has been difficult to reproduce this result.[99] Later on, in 2018, Zhang *et al.* reported a carbon nitride treated by post-calcination in molten salts, which produces H_2 at an extremely high quantum yield of 60% under vacuum conditions and also some O_2 (λ>300 nm, LED). The pure visible activity of O_2 production was not reported.

Although extensive efforts have been made to increase the hydrogen production efficiency of polymeric photocatalysts, there are only a few working efficiently for oxygen production. Nitrogen-containing aza-CMP nanosheets are a rare example evolving oxygen from water under illumination in the presence of silver nitrate as a sacrificial acceptor.[101-102] Recently, a combination of aza-CMP and C_2N nanosheets,[103] as well as ethynyl benzene based CMPs (PTEB/PTEPB),[102, 104] have been reported to perform overall water splitting and to evolve hydrogen and oxygen simultaneously in a 2:1 ratio. Repeating these results have proven to be difficult.

As there might be oxygen species on the surface or in the bulk of polymers, it is very crucial to validate that the oxygen is produced from water instead of releasing from the materials or dissolved oxygen in the

water. Regarding the validity of oxygen production, ^{18}O isotopic labelling is a useful method. Alternatively, if the total amount of oxygen produced outnumbers that contained in the material as calculated from characterisations, the oxygen collected is more likely from the water. Silver nitrites are commonly used as an efficient electron scavenger in oxygen production half reactions in the literature. However, the silver metal generated during the process often covers the surface of photocatalysts and hinders the continuous production of oxygen. Sometimes the oxygen production decays and stops. Also, in such a case, it is difficult to prove the stability of polymers because the sample is not reusable. Sodium iodate, another electron scavenger, doesn't suffer from the same issue because it is reduced to I^- and could be used for continuous oxygen production to confirm the stability. However, it must be noted that IO_3^- could produce oxygen under UV light irradiation ($\lambda < 300$ nm). The reaction can be expressed by the following equation: $IO_3^- + hv\ (\lambda < 300\ nm) = I^- + \frac{3}{2}O_2$. Therefore when using $NaIO_3$ as electron scavenger, UV light must be removed adequately.

2.4. Z-scheme systems for water splitting

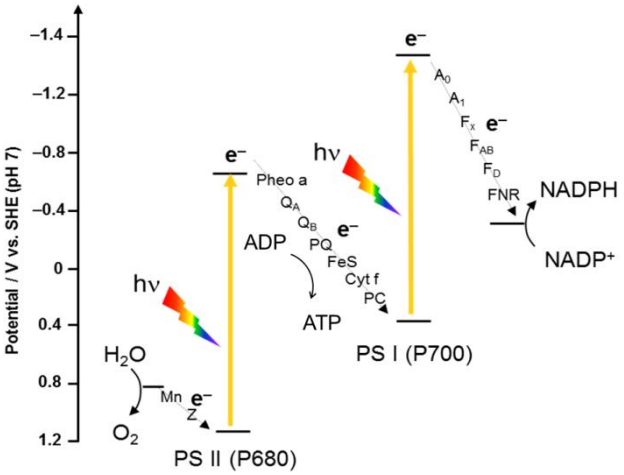

Figure 5. A schematic diagram of a double excitation process on P680 and P700 in natural photosynthesis[105]

Figure 5 shows the double excitation system in natural photosynthesis, along with the electron cascade steps. At certain wavelengths, this system can operate at an AQY over 95%.[106-107] Reaction centres chlorophylls in Photosystem II (PSII) absorb photons ($\lambda \leq 680$ nm), leading to the generation of electron-hole pairs. The photo-induced holes oxidise water to produce oxygen, protons and electrons. The electrons are transferred via the electron transport chain, whereas the protons released are accumulated in one side of the membrane to build an electronic potential to support the conversion

of ADP (adenosine diphosphate) into ATP (adenosine triphosphate). In Photosystem I (PS I), electrons are excited again by photons ($\lambda \leq 700$ nm), the holes are quenched by the electrons produced by PSII, simultaneously elongating the electron lifetime so more reduction reactions can occur. The electrons from PSI are finally used to reduce $NADP^+$ to NADPH, which, together with ATP, provides the reduction power and energy for the conversion of CO_2 to sugars.[30]

Inspired by the natural photosynthesis, an inorganic double excitation system was proposed first by Sayama and Abe *et al.*[108] In such a system, the water-splitting reaction is separated into two reactions O_2 evolution and H_2 evolution. When photons are absorbed by an OEP, electrons on the VB will be excited to CB, leaving holes to oxidise water to O_2. The electrons on the CB first reduce the corresponding electron acceptors (i.e. oxidant: Ox) to the electron donors (i.e. reductant: Red). Then, the electron donors (Red) are converted back to its oxidised form (Ox) by the oxidation by photoholes on the surface of a HEP. Hence, the electrons are transferred between two photocatalysts by the appropriate shuttle redox couple in solution continuously.

Meanwhile, protons are reduced to hydrogen by the photoexcited electrons on the CB of a HEP. As such, the overall water splitting reaction is complete with regeneration of redox mediators (ions or molecules), and light being the only energy input. However, Red can be oxidised by holes from the VB of OEP and similarly the electrons on the CB of HEP can react with Ox, i.e. back reactions take place. Thus, for an efficient Z-scheme system, back reactions should be inhibited (dotted curves shown in Figure 6).

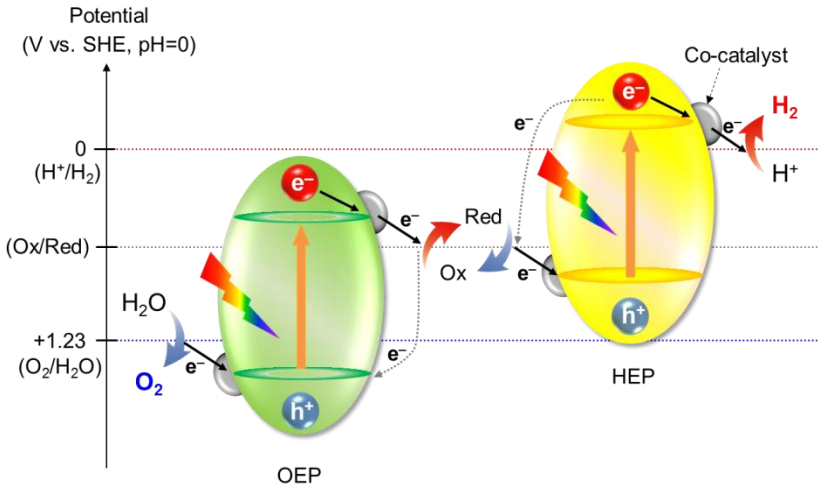

Figure 6. Double excitation system based on a HEP and OEP with a shuttle of Ox: oxidant and Red: reductant molecule. Two dotted curves indicate the back reactions which are not expected.[105]

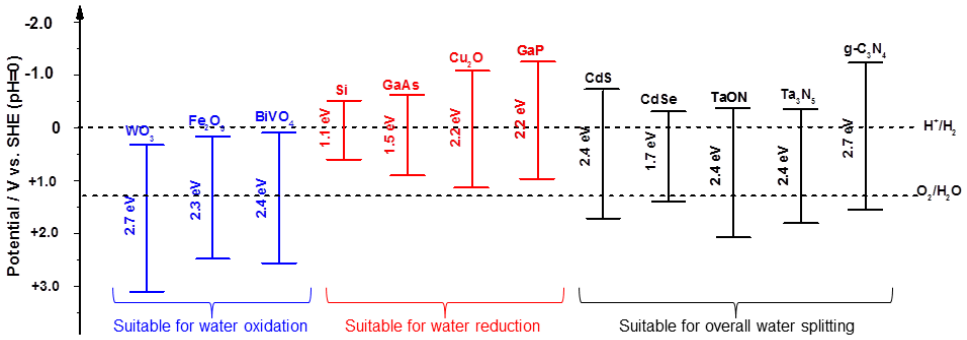

Figure 7. Band edge positions of typical semiconductors for visible light-driven water splitting. [105]

Z-scheme-based on inorganic semiconductors

Water splitting with liquid mediators

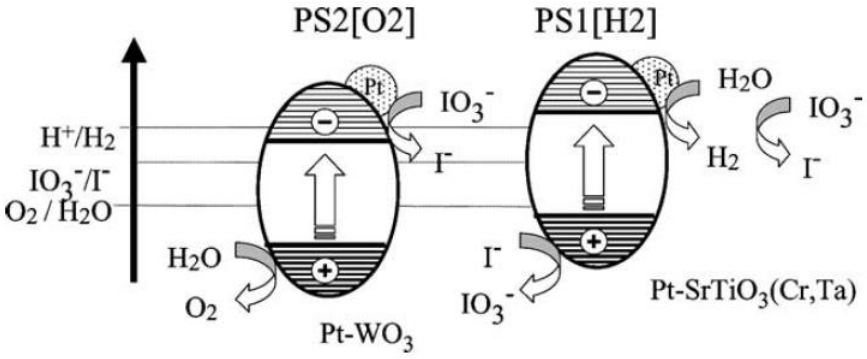

Figure 8. Speculated reaction mechanism using IO_3^-/I^- redox mediator (pH 7).[109] **Reprinted with permission from ref 109. Copyright 2002 Elsevier.**

(Pt/$SrTiO_3$:Cr,Ta)–(IO_3^-/I^-)–(PtO_x/WO_3) system was the first example of visible light-driven overall water splitting reported in 2002, and apparent quantum yield (AQY) of 1% was achieved at 420 nm under optimised conditions in 2005 (Figure 8).[109] For the first time, selective O_2 evolution was achieved on PtO_x/WO_3 even in the presence of a considerable amount of I^-, which was thermodynamically more favourable to be oxidised by holes. The selective redox of shuttle pairs is the key property for the construction of the Z-scheme; the adsorption of IO_3^- anions, instead of I^-, to the photocatalysts' surface was thermodynamically preferable under pH of 7, thus ensuring close contact between shuttle species and charges. H_2 and O_2 could be generated at a ratio of 2:1 when the two half reactions were combined. In this work, the pH of the solution was also important. Alkaline conditions were shown to be more favourable for water splitting, because acidic conditions generate side products such as I_3^- which can be reduced to I^- in place of IO_3^-, breaking the redox cycle. NaI concentration was also tailored to approach the optimum condition to avoid the formation of an oxyanionic tungstate compound or the more likely hydrogen tungstate ion.[110]

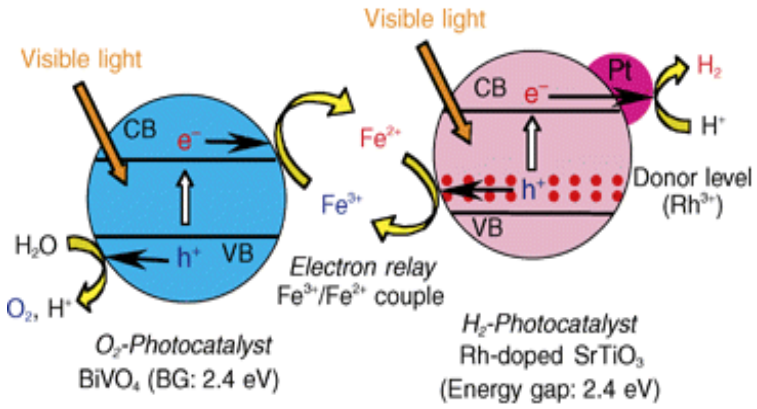

Figure 9. The working diagram of Z-scheme water splitting based on $BiVO_4$.[111] Reprinted with permission from ref 111. Copyright 2004 the Chemical Society of Japan.

The first ($Pt/SrTiO_3$: Rh)–(Fe^{3+}/Fe^{2+})–($BiVO_4$ or Bi_2MoO_6) Z-scheme water splitting system was reported in 2004 (Figure 9).[111] Using Fe^{3+} ($FeCl_3$) as an electron scavenger, $BiVO_4$ could evolve oxygen steadily, while separately, Fe^{2+} ($FeCl_2$) was found to be sufficient as a hole scavenger for hydrogen evolution over $Pt/SrTiO_3$: Rh. After combining the two sides, H_2 and O_2 from overall water splitting were observed steadily even after 158 h. This system worked under wavelengths of up to 530 nm, consistent with the absorption onsets of $Pt/SrTiO_3$: Rh and $BiVO_4$. The AQY of ($Pt/SrTiO_3$:Rh)–(Fe^{3+}/Fe^{2+})–($BiVO_4$) is 0.3% at 440 nm which is higher than both ($Pt/SrTiO_3$:Rh)–(Fe^{3+}/Fe^{2+})–(Bi_2MoO_6) and ($Pt/SrTiO_3$:Rh)–(Fe^{3+}/Fe^{2+})–(WO_3) (0.2%). But the WO_3-based system

showed a higher AQY of 0.5 % than 0.4% of the $BiVO_4$ system at 420 nm.

So far, the highest AQY of a Z-scheme in the presence of a dissolved mediator for overall water splitting was achieved using a ($MgTa_2O_{6-x}N_y$/TaON)–(IO_3^-/I^-)–(PtO_x/WO_3) system.[112] The AQY of 6.8% at 420 nm under optimum conditions was reported in 2015. The band locations ensured an absorption of visible light up to 570 nm as a Type II heterojunction structure.[112] As expected, electron transfer occurs from the CB of $MgTa_2O_{6-x}N_y$ to the CB of TaON, and holes transfer from the VB of TaON to the VB of $MgTa_2O_{6-x}N_y$, thus the recombination of charge carriers was effectively suppressed by the heterostructure, as confirmed by the prolonged charges' lifetime from time-resolved infrared spectra (TRIR). When irradiated by light with a wavelength above 520 nm, the junction still produced H_2 while TaON alone did not. The gas evolution rate was even higher than that of Pt/$MgTa_2O_{6-x}N_y$ only with a wavelength > 420 nm, revealing a spatially separated charge transfer mechanism that was responsible for the enhancement of photocatalytic activity at a longer wavelength. Pt metal was observed to be photoreduced on the surface of TaON instead of $MgTa_2O_{6-x}N_y$,

which confirmed photoexcited electrons were transferred from $MgTa_2O_{6-x}N_y$ to TaON. The one-pot synthesis method of ammonia treating $MgTa_2O_6/Ta_2O_5$ provided a more intimate interfacial contact and fewer defects than a simple mechanical mixture of $MgTa_2O_{6-x}N_y$ with TaON. Although heterojunction structures were widely used in photocatalysts, this was the first time to be applied as a HEP in a Z-scheme system. This work demonstrated the possibility of using heterostructured photocatalysts for half reactions in overall water splitting.

Water splitting with solid redox mediators

A simple solid electron shuttle instead of the redox pairs should be more favourable as it rules out the redox diffusion process,[48] which could also be facile and appropriate to the practical use.[113] Dissolved ions redox-mediated systems are easily investigated by half reaction tests for either H_2 or O_2 with an appropriate sacrificial reagent, following pure water splitting by the coupled pairs. However, in solid shuttle system, one has to synthesise the HEP/shuttle/OEP double junction first before testing the gas evolution activities. Another

obstacle to solid junctions is the charge recombination between layers.[114]

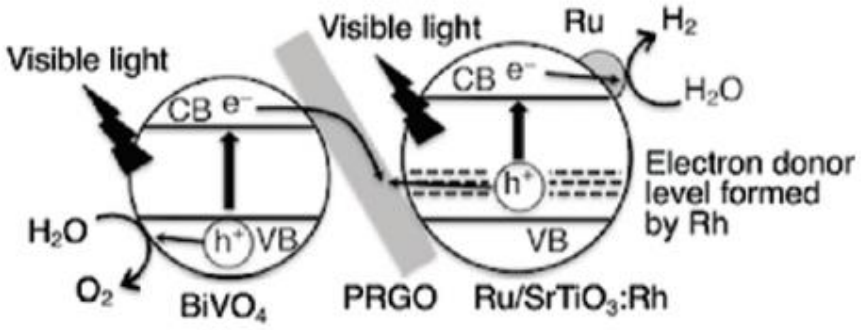

Figure 10. Mechanism of water splitting in a Z-scheme photocatalyst system consisting of Ru/$SrTiO_3$: Rh, and $BiVO_4$ under visible-light irradiation using RGO as a mediator.[113] Reproduced with permission from ref 113. Copyright 2011 American Chemical Society.

The first visible light-driven solid mediator Z-scheme for overall water splitting by Iwase *et al.* is illustrated in Figure 10 where photoreduced graphene oxide (PRGO) was used as the electron shuttle in a system composed of $BiVO_4$ and Ru/$SrTiO_3$: Rh. Doped $SrTiO_3$ acted as the HEP and $BiVO_4$ as the OEP, which were the most commonly used two photocatalysts in a dissolved mediate system. The highest rates achieved were 11 and 5.5 μmol h^{-1} for H_2 and O_2 production, respectively, indicating pure water splitting. Different from other "dissolved redox mediators", PRGO was a conductor and transferred electrons freely between semiconductors. But the back pathway was suppressed because the photoexcited electrons in $BiVO_4$ cannot reduce

proton and the positive charges (i.e., Rh^{4+} species) in Ru/$SrTiO_3$: Rh cannot oxidise water at the same time.[114] PRGO was photo reduced on $BiVO_4$ instead of on Ru/$SrTiO_3$: Rh, which could help the electron relay. Both the reduced GO on Ru/$SrTiO_3$: Rh and hydrazine-reduced GO failed to perform overall water splitting.

An efficient Z-scheme system using Au as a solid shuttle ($SrTiO_3$: La, Rh/Au nanoparticle/$BiVO_4$: Mo photocatalyst sheets) was reported (Figure 11).[115-116] On the photocatalyst sheet, HEP and OEP particles were physically embedded into the gold layer. The STH energy conversions efficiency reached 1.1% with an AQY of 33% at 419 nm, which were both nearly one order of magnitude higher than that reported in the liquid mediator system and became a benchmark result in the Z-scheme systems.[116] Unlike GO used in the previous section, the underlying gold layer provided a much better charge transfer for the embedded photocatalysts via a particle transfer method. The contact resistance of the Schottky barrier, which is the most common problem in solid state Z-scheme systems and also the strongest dependency in this work, between the metallic gold layer and semiconductors, was reduced by controlling the annealing time and temperature. The extended

annealing temperature and duration enhanced the contact between them, probably due to crystallinity, while too high temperature or too long durations decreased the activity considerably, which was attributed to the volatilisation of V_2O_5.[97] The back reaction, which was a crucial factor in other Z-scheme systems, was considered in this work as well, as H_2 and O_2 formed at sites in proximity to each other. Protection layers of Cr_2O_3 and amorphous TiO_2 were applied, effectively capping the surface, and suppressing back reactions.[117]

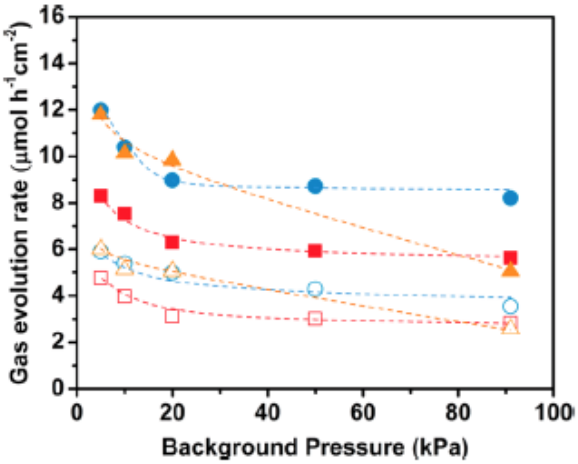

Figure 11. Squares (□), circles (○), and triangles (△) stand for Ru-loaded $SrTiO_3$:La,Rh/C/$BiVO_4$:Mo, Cr_2O_3/Ru-loaded $SrTiO_3$:La,Rh/C/$BiVO_4$:Mo, and a-TiO_2/Cr_2O_3/Ru-loaded $SrTiO_3$:La,Rh/Au/$BiVO_4$:Mo, respectively. Closed and open symbols represent hydrogen and oxygen, respectively. Photodeposition from $RuCl_3 \cdot 3H_2O$ (0.2 μmol), K_2CrO_4 (0.2 μmol), Ti peroxide (1.3 μmol) and the overall water-splitting reaction were carried out under Xe lamp (300 W) illumination (λ > 420 nm) at 288 K. The area of the photocatalyst sheets was 7.5 cm^2. [118] Reproduced with permission from ref 118. Copyright 2017 American Chemical Society.

Very recently, the same research group successfully introduced a conductive carbon as an efficient electron mediator to a particulate photocatalyst sheet. The unfavourable occurrence of the backward reaction was effectively suppressed, thereby affording efficient Z-scheme water splitting even at ambient pressure.[118] The $SrTiO_3$:La,Rh/C/$BiVO_4$:Mo sheet was demonstrated to split pure water (pH 6.8) with an STH energy conversion efficiency of 1.2% at 331 K and 10 KPa while retaining 80% of this efficiency at 91 KPa. Other metals including Ag were also reported to work as shuttles in Z-scheme water splitting systems, such as $ZnRh_2O_4$/Ag/$Ag_{1-x}SbO_{3-y}$ by Kobayashi *et al.*,[119] where electrons are transferred from the CB of $Ag_{1-x}SbO_{3-y}$, via the solid-state mediator Ag, to the VB of $ZnRh_2O_4$.

Water splitting without mediators

Further to simplify a Z-scheme structure for water splitting, a system based on inter-particle electron transfer could be developed as mediator-free Z-scheme systems. Compared with Z-scheme containing dissolved redox mediator and solid mediator systems, the mediator-free Z-scheme system is very challenging and was reported very

recently, *e.g.* ($BiVO_4$)–(Ru/$SrTiO_3$:Rh) or (Ir/CoO_x/Ta_3N_5)–(Ru/$SrTiO_3$:Rh) systems as illustrated in Figure 12.[120, 121]

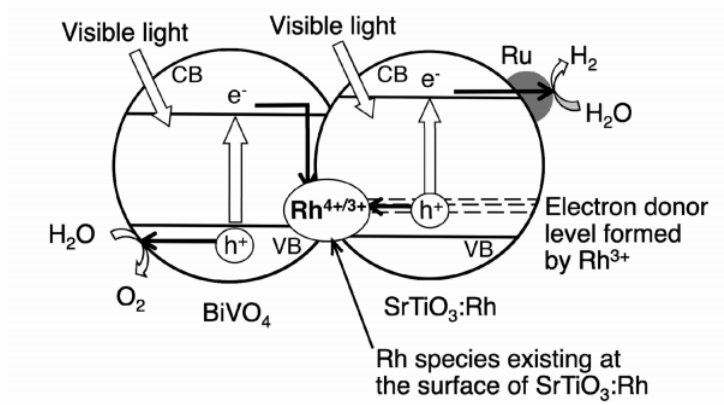

Figure 12. Scheme of photocatalytic water splitting in the absence of mediators.[114] Reproduced with permission from ref 114. Copyright 2011 Cambridge University Press.

The reversibility of an oxidation state between Rh^{3+} and Rh^{4+} is the benefit side in this Z-scheme charge transfer process. Ru/$SrTiO_3$:Rh has two absorption onsets, one at 520 nm due to the donor level formed by Rh^{3+} to CB and the other at 580 nm assigned to the VB to acceptor level by Rh^{4+}. The 520 nm band was responsible to the H_2 evolution while the band at 580 nm was inactive. The H_2 reduction under different temperatures was tested to clarify the details of Rh oxidation reversibility. The Rh^{3+} of $SrTiO_3$:Rh under 473 K and below was able to be reversibly oxidised but the one reduced at 573 K was quite stable. The characterisations of the samples treated at lower temperatures

were similar to the non-reduced compounds, while the high temperature appeared to reduce the reversible oxidation state significantly. It was concluded that the surface Rh ions, with reversible oxidation state, served for the electron transfer process as the role of a shuttle.[118]

In the ($BiVO_4$)–(Ru/$SrTiO_3$:Rh) system, the AQY was reported to be 1.7% at 420 nm, and the STH conversion efficiency reached 0.12%. Two systems denoted as a separation system, and a mixed system composed of the same materials were compared to prove there was an electron relay between two photocatalysts. When the two photocatalysts located at different regions in the reactor (separation system), overall water splitting was not observed, because there was no physical contact or conductive/redox species in this system so that the charge transfer could not proceed through aqueous media. Water splitting only followed if the powders were mixed (mixture system), indicating the electron transfer between particles happened to realise the overall water splitting in this dual excitation system. The pH of the system influenced the activity mainly due to a zeta potential effect whereby the overall charge upon Ru/$SrTiO_3$:Rh caused aggregation, the

highest degree when pH was 3.5, while $BiVO_4$ was found not to be influenced by pH value.

Z-scheme based on graphitic carbon nitride

Overall water splitting by polymers remains a big challenge due to the limiting factors mentioned earlier. Remarkably, g-C_3N_4 is the first polymer to be used for Z-scheme pure water splitting which was reported by us, where g-C_3N_4 and $BiVO_4$ powders were used as reduction and oxidation photocatalysts respectively using the redox mediators $Fe^{2+/3+}$. Furthermore, WO_3 was used to replace $BiVO_4$ and coupled with g-C_3N_4 in the presence of the mediator I^-/IO_3^-, resulting in a further 3-fold increase in activity for pure water splitting.[18] Later, Zhao *et al.* reported a Pt-loaded g-C_3N_4/WO_3 that possessed an intimate interfacial contact aided by the introduction of reduced graphene oxide (rGO) as a linker, resulting in a 2:1 ratio of evolved H_2 to O_2 under visible light from the pure water.[122] More recently, pure water splitting on g-C_3N_4 has achieved by the careful addition of dual co-catalysts of Pt/PtO_x or Pt/CoP that function as either reduction or oxidation sites although the optimisation of dual co-catalysts onto a

single polymer is extremely challenging and difficult to control.[35, 123] Perhaps the most striking example of pure water splitting is the g-C_3N_4/carbon quantum dots (QDs) composite reported by Liu *et al.*.[99] Importantly, because H_2O_2 formation is more thermodynamically favourable on g-C_3N_4 than O_2 evolution,[100] a co-catalyst is needed to affect charge separation and decompose peroxide to molecular oxygen, whilst the g-C_3N_4 can photocatalytically evolve H_2. This step-wise two-electron process bypasses the slow four hole kinetics usually attributed to the OER, leading to a remarkable STH of 2%. However, it is difficult to reproduce this figure.[99]

In total, in the urea-derived g-C_3N_4 based Z-scheme system, both Pt-g-C_3N_4-IO_3^-/I^--Pt-WO_3 and Pt-g-C_3N_4- Fe^{3+}/Fe^{2+}-$BiVO_4$ represented to split water continuously, with an initial gas evolution rate of H_2 and O_2 at 74 and 37 μmol g^{-1} h^{-1}, 15 and 8 μmol g^{-1} h^{-1}, respectively. The systems worked under both full arc and visible, yielding reproducible H_2 and O_2 for over 24 h. The VB of g-C_3N_4 lied as deep as +1.5 eV (vs SHE at pH 0), which is suitable for the mediators' redox potential (IO_3^- /I^- at 1.085 – 0.059pH eV and Fe^{3+}/Fe^{2+} at 0.77 eV). One thing to note was that only urea-derived g-C_3N_4 was active in these systems.

Thiourea and dicyandiamide did not work here although they could photocatalytically produce H_2 from water.[18] Their unsatisfying band positions and the surface conditions could be the reason for the phenomena, but it could also be that they are not efficient enough to generate a detectable amount of hydrogen. As for urea-derived g-C_3N_4, the lower degree of surface protonation was more favourable for the adsorption of I^- or Fe^{2+} ions on the photocatalyst surface, thus making the cycle reaction easy to facilitate.

2.5 Photocatalytic CO_2 conversion

Given the consumption of fossil fuels has been increasing the level of atmospheric CO_2 and consequently causing the imminent climate change, the neutral-carbon economical approach by conversion of CO_2 by inexhaustible solar energy is urgently desired.[124-126] Natural photosynthesis supplies sustainable energy for all lives and maintains an ecological balance on this planet, by CO_2 fixation into sugar and O_2 production from water.[127] To reproduce this essential solar energy storage reaction, continuous efforts have been put as a promising solution to address the current energy and environmental issues. Particularly, the past few years have witnessed several benchmark

materials reported for photocatalytic CO_2 conversion to CO, methane, formic acid or their mixtures.[128-133]

For example, Yang *et al.* used *moorella thermoacetica* with cadmium sulfide nanoparticles to reduce CO_2 to acetic acid in the presence of cysteine, resulting in a 2.4% quantum yield under stimulated one sun irradiation.[128] Robert *et al.* used an iron tetraphenylporphyrin complex functionalized by trimethylammonio groups to convert CO_2 to methane in the presence of triethylamine, resulting into 82% selectivity and 0.18% quantum yield.[129] However, the activities of these materials highly depend on the efficiency of electron donors/sacrificial scavengers to prevent electron/hole recombination losses. In these studies, the use of expensive sacrificial scavengers was essential to achieve the photocatalytic CO_2 reduction. Without these scavengers, the photocatalysts did not work or worked much less efficiently. Such processes are thus unsustainable and economically unfavourable due to the necessity of adding the sacrificial donor. A preferable, yet more challenging process is to couple photoreduction of CO_2 by electrons to water oxidation by holes, thus utilising water to reduce CO_2 and simultaneously generating fuels and oxygen.

Furthermore, methanol is a more favourable product than CO, methane or formic acid, as it is more convenient to store, transport and use. Therefore, a desirable one-step photocatalytic system should preserve methanol production with a focus on high selectivity for water oxidation. However, this conversion is more challenging due to a kinetically unfavourable six-electron process and high volatility of methanol.

Table 2 summarises the reported methanol production examples from photocatalytic carbon dioxide reduction.

Table 2. A literature review of CO_2 reduction to MeOH under visible light in aqueous environments.

	Photocatalyst	AQY@420nm if not specified	Activity as the production of MeOH µmol/g	^{13}C isotopic	O_2 gas measurement	Selectivity	Reference
1	AgBr/TiO_2 nanocomposites	-	73.42	×	×	31.3%	[134]
2	CoPc loaded titania	-	Trace	×	×	-	[135]
3	CdS(Bi_2S_3)/TiO_2 nanotubes	-	44.92	×	×		[136]
4	anatase–brookite TiO_2 composite	0.0717	0.478	×	×		[137]
5	NiO–InNbO4	-	1.577	×	×		[138]
6	NiO/InTaO4	2.45 (internal QY)(500 W halogen lamp)	1.394	×	×		[139]
7	NiO/InTaO4	0.063	11.1	×	×		[140]
8	N-doped $InTaO_4$		160	×	×		[141]
9	monoclinic $BiVO_4$		9	×	×	44%	[142]
10	Bi_2WO_6 hollow microspheres		32.6	×	×		[143]
11	Bi_2S_3/CdS		74.6	×	×		[144]

12	$Cu_xAg_yIn_zZn_kS_m$ solid solutions		118.5	×	×		[145]
13	mesoporous flake g-C_3N_4	0.18	6.3	×	×	58.3	[146]
14	Graphene oxide		0.172	√	×		[147]
15	rGO–CuO	1.3 (visible LED)	53.4	×	√		[148]
16	(CQDs)/Cu_2O		55.7	×	×		[149]
17	Ag/TiO_2		29.9	×	×		[150]
18	graphene− TiO_2 a	2.3 (internal QY) (670 nm)	8	×	×		[151]
19	$BiVO_4$ (0.2g)	0.22 (visible) 0.24 (full sepectrum)	3.76 27.6	×	√		[152]
20	ZIF-8/Zn_2GeO_4 nanorods		1.43	×	×		[153]
21	$InTaO_4$		2.8	×	×		[154]
22	g-C_3N_4/WO_3		34.72	√	×		[155]

As listed in the above table, so far most of the publications didn't use earth-abundant low-cost carbon-based catalysts, and very few reported a complete chemical cycle with full consideration of the literature. In the whole cycle, the catalyst should not only reduce CO_2 but also oxidise water as proved by the stoichiometric reduction product methanol and oxidation product oxygen gas. Also, the selectivity of methanol, the confirmation of carbon source by C-13 isotopic labelling and AQY were hardly provided in these publications. When using carbon-based catalysts for CO_2 conversion, isotopic measurement is crucial to avoid misleading information, because organic impurities in carbon materials (which cannot be avoided due to its preparation procedure) can be oxidised to some hydrocarbons (*e.g.* CH_4, methanol). So ^{13}C isotopic measurement is extremely important in such a chemical process.

Regarding the polymer-based CO_2 conversion system, limited examples could be found for methanol production from the literature. Ohno *et al.* reported a visible, active photocatalyst for CO_2 reduction

to methanol by mixing g-C_3N_4 and WO_3 with planetary milling.[156] The 13-C measurement has been carried out. However, no oxygen or long-term stability was reported in this work. Ong *et al.* developed a CQD/g-C_3N_4 junction for CO_2 reduction to CH_4 and CO. However, no 13-C labelling and oxygen were reported. The CQD prepared from sonication of glucose acted as an electron acceptor and reduction cocatalysts.

2.6 Summary

Polymeric catalysts have been identified as efficient HEP photocatalysts recently. Besides, their advantages of low-cost and good tunability are beneficial for the strategy bandgap engineering. Although many efforts have been made to increase the light absorption as well as inhibit the rapid charge recombination, there hasn't been one example to achieve both targets at the same time. On the one hand, highly efficient polymer examples are mainly responsive to light below 470 nm and mainly active for H_2 production half reaction. Furthermore, water oxidation polymeric photocatalysts have been less developed

and reported compared to the hydrogen production polymers. Motivated by the potential of polymeric photocatalysts, I plan to design a series of polymeric photocatalysts with extensive absorption as well as high AQY by altering their structure via careful control of polymerisation process for both proton reduction and water oxidation half reactions.

One of the most promising artificial photosynthesis systems is visible light-driven Z-scheme system. Among them, most reports focus on liquid mediator systems, but the STHs are still moderate. The solid mediator one has achieved the benchmark STH efficiency so far due to the short charge transfer process as discussed above. Besides the mediator, the unsatisfactory utilisation of visible light photons is another issue hindering the STH increasing due to the relatively wide bandgap of HEP and OEP.

Up to now none of these solid-state Z-scheme systems involves narrow bandgap photocatalysts with light absorption above 550 nm, in particular, polymeric photocatalysts. Therefore, I would construct polymer based visible light-driven Z-scheme systems which could harvest a large portion of visible photons (400 – 750 nm). This would rely on the development of efficient and narrow bandgap HEP and OEP

photocatalysts. Hence I have chosen to develop a strategy to tune the band positions of the polymeric photocatalyst to meet the position requirement while maintaining a high activity.

Last but not the least, CO_2 photoreduction has recently been substantially investigated but mainly on inorganic photocatalysts with the major products of CO, methane *etc.* Solar-driven CO_2 fixation to methanol fuel is not only a way to utilise CO_2 as a feedstock but also store H_2 produced by water splitting into organic compounds, thus more attractive while much more challenging. Polymeric photocatalysts have seldom been used in CO_2 conversion to methanol. The CO_2 conversion will be investigated using the developed new polymeric photocatalysts and cocatalysts. The reaction mechanism will also be discussed in detail.

3. Experimental development

This chapter will describe the facilities and methodologies used to characterise materials prepared in the project.

3.1 Material preparation

DCDA-derived graphitic carbon nitrides (g-C_3N_4), the reference material, was synthesised as reported, which was calcined at 550 ^oC for 4 hours at a ramp rate of 2.3 ^oC/min.[157] In a typical oxygen-nitrogen linked heptazine (ONLH) synthesis, 80-120 g of semicarbazide hydrochloride was put in a lidded high-quality alumina crucible, then placed inside a furnace and heated at a ramp rate of 5^oC/ min, and finally held at 600^oC for four hours. The samples were ground and washed by water, HCl, NaOH and water again to remove all unreacted and potentially detrimental surface species. The products were denoted as ONLH and g-C_3N_4. Other preparation details are listed below in each Chapter.

3.2 Material characterisation

3.2.1 Powder X-ray diffraction (PXRD)

Powder X-Ray Diffraction (PXRD) measurements were taken using a Bruker D4 diffractometer, a voltage of 40 kV, at 30 mA, using a Cu source with Kα1 = 1.540562 Å and Kα2 = 1.544398 Å, accompanied by a nickel filter. X-ray diffraction peaks occur when Bragg's equation is satisfied for constructive interference for planes with spacing d. Where d is the spacing between different planes, θ is the incident angle, n is an integer, and λ is the wavelength of the X-ray.

Bragg's equation: $2d \sin\theta = n\lambda$

3.2.2 UV-Vis

UV-Vis absorption spectra were performed on a Shimadzu UV-Vis 2550 spectrophotometer fitted with an integrating sphere. A standard barium sulphate powder was used as a reference. The reflection spectrum was collected between 325 nm and 825 nm with a scan rate of medium speed. Absorption spectra were achieved from the converted reflection measurements via the Kubelka-Munk transformation.

3.2.3 Fourier transform infrared spectroscopy

ATR-FTIR spectroscopy was collected using a Perkin-Elmer 1605 FT-IR spectrometer in the wavenumber range from 500 – 4000 cm^{-1} with a resolution of 0.5 cm^{-1}.

3.2.4 Raman spectroscopy

Raman spectroscopic measurements were performed on a Renishaw InVia Raman Microscope, using a 325 nm excitation laser and a wavenumber range from 100–2000 cm^{-1}.

3.2.6 Brunauer–Emmett–Teller (BET)

Specific surface area measurements were taken using the BET method (N_2 absorption, TriStar 3000, Micromeritics). Typically, the sample was added to a glassware and then degassed at 120 ^oC under the protection of N_2 gas overnight. After degassing, the weight of the sample and glassware was recorded before putting into the BET machine for surface area measurement under the liquid nitrogen environment.

3.2.5 Scanning Electron Microscopy (SEM)

Scanning Electron Microscopy (SEM) images were gained from a JEOL JSM-7401F high-resolution Emission SEM operating at 2-3 kV. Due to the low conductivity of the semiconductor materials, Au coating was applied to the samples to improve the image quality.

3.2.7 X-ray photoelectron spectroscopy (XPS)

XPS measurements were done on a Thermoscientific XPS K-alpha surface analysis machine using an Al source. AnalThe analysis performed on the Thermo Advantage software. Each sample was scanned at least 3 times at 3 points on the surface or in the ion-etched mode to eliminate point error and create an average. Specific elemental peaks were then identified and analysed further.

3.2.8 Elemental Analysis (EA)

Elemental Analysis (EA) was performed on a Micro Elemental Analyzer (CE-400 CHN Analyser, Exeter Analytical Instruments). Accurate (± 0.1%) weight percentages of carbon, nitrogen, hydrogen and trace elements were converted to atomic percentages before analysis.

3.2.9 Transient Absorption Spectroscopies (TAS)

TAS can enable the direct observation of the dynamics of trapped carrier populations.[158-160] TAS data were acquired on home-built setups. 355 nm laser excitation was generated from an Nd:YAG laser (OPOTEK Opolette 355 II, 7 ns pulse width). The 355 nm excitation fluence was set to 460 μJ/cm2 for the GCNN and CQD/GCNN samples and 680 μJ/cm2 for the CQD samples. The probe light was generated from a quartz halogen lamp (Bentham IL1). Long pass filters (Comar Instruments) were placed between the lamp and sample to minimise short wavelength irradiation of the sample. A 5 cm path length cuvette filled with DI water was also placed in the beam path as an IR filter to avoid heating effects. A long pass filter positioned between the sample and a monochromator was used to block scattered laser light. The probe wavelength was selected by the monochromator and, the light relayed to a Si photodiode detector (Hamamatsu S3071). Data on the sub-ms timescale were conditioned by an electronic amplifier box (Centronics) and recorded on an oscilloscope. Data on the ms timescale was simultaneously recorded on a National Instruments DAQ card. Acquisitions were triggered by a photodiode (Thorlabs DET10A)

exposed to laser scatter. Data from at least 32 laser pulses were acquired and processed using home-built software written in the Labview environment to obtain the kinetic traces presented.

A typical transmission setup was used in the case of the homogeneous CQD samples (0.6 mg/mL aqueous solution) where the change in transmitted light intensity is measured. A diffuse reflectance setup was used in the case of the scattering GCNN and CQD/GCNN samples (2 mg/mL aqueous dispersion). Here the diffusively reflected light is collected by a 2″ diameter, 2″ focal length lens and relayed to the monochromator, and the change in reflected light taken as the change in absorption (i.e. Absorption + Reflectance = 1 – Transmission = constant).

We convert the absorbance signal to relative change in the detected light intensity (in transmission mode) by using:

$$\Delta OD_t = -\log\left(\frac{T_t}{T_0}\right); 10^{-\Delta OD_t} = \frac{T_t}{T_0}$$

$$10^{-\Delta OD_t} - 1 = \frac{T_t}{T_0} - \frac{T_0}{T_0} = \frac{T_t - T_0}{T_0}$$

$$\%Absorption_t = 100 \times \frac{-\Delta T_t}{T_0} = 100 \times \frac{-(T_t - T_0)}{T_0}$$
$$= -100 \times (10^{-\Delta OD_t} - 1)$$

ΔOD is the change in absorbance (in absorbance units), T is the transmission (in decimal units), $\%Absorption$ is the relative change in absorbance (in percentile), and the subscripts 0 and t indicate either the initial value or the value at time t.

3.3 Activity evaluation

In a typical H_2 production reaction, 10 mg photocatalyst with a certain w.t.% of Pt (H_2PtCl_6 as a precursor) was well dispersed in 50 ml aqueous solution containing 10 vol.% TEOA as a sacrificial electron donor and all together were added into a 130 ml reactor. The reactor was sealed, purged with Argon gas for 1 hour and then irradiated under full arc to perform the photodeposition of Pt co-catalyst using a 300 W Xenon light source (Newport 66485-300XF-R1, Research Arc Lamp

Source, 300 W Xenon Ozone Free, Aspheric Lens F/1.). The reactor was then re-purged before irradiation under either full arc or visible irradiation with different filters (Comar Optics). In a typical quantum yield measurement, 100 mg photocatalyst was used with an additional $K_2HPO_4 \cdot 3H_2O$ (2.28 g, 0.01 mol) to mimic the natural environment.[65]

Apparent quantum yield (AQY) (Φ) was calculated by using the following formula:

$$\mathrm{AQY} = \frac{2 \times \text{the number of evolved Hydrogen molecules}}{\text{the number of incident photons}} \times 100\%$$

The measurements were taken by an optical power meter (Newport Spectra) installed with an appropriate bandpass filter (420, 500, 600, 700, 800 nm, λ ± 10 nm at 10% of peak height, Comar Optics) inserted between a 300 W Xe light source (Newport 66485-300XF-R1) and reactor. After the photodeposition and re-purging, GC injections were made to detect the H_2 produced from the following procedure.

The process of water splitting often yields two gases – oxygen and hydrogen, and being able to calculate the amount of each produced is vital. Gas chromatography is used to analyse concentrations and amounts of gas in each atmosphere, often to a great resolution. A

sample of gas is injected; the elements of the gas (mobile phase) are separated by a stationary phase 'column' (often stainless steel tubing, densely packed with diatomaceous earth), compounds elute at different times and pass through the detector where a signal is generated and data can be produced.

Gas Chromatography (GC) is usually fitted with either a Thermal Conductivity Detector (TCD) or a Flame Ionisation Detector (FID). The most suitable detector for simultaneous hydrogen and oxygen detection would be a TCD. As the name suggests, the TCD detects changes in thermal conductivity produced by the sample from a standard gas flow (carrier gas). Popular carrier gases are hydrogen, nitrogen, helium and argon. Argon is ideal for hydrogen and oxygen detection since it has a thermal conductivity lower than the respective gases[161]. Helium could be used, however, due to its similar thermal conductivity to hydrogen, it would be unfavourable. Furthermore, argon is excellent at purging systems and is cheap and readily available.

There are two types of analysis associated with GC's; qualitative and quantitative. Data is represented as a graph of retention time (x-axis) and detector response (y-axis); the retention time is specific to each compound (qualitative), and the detector response is dependent

(with a TCD) on the thermal conductivity or amount of each element (quantitative). Chromatographic data, therefore, yields a spectrum of 'peaks' separated only by time. The area under each peak represents the amount of substance present. By using a calibration curve (responses from a series of known concentrations/amounts), one can then determine the amount of substance present, and correctly identify the element/compound by its distinct retention time.

For H_2 and O_2 measurements, a Varian 430-GC was used, with optimum settings for discovering both gases. 'Zero Grade' Argon was used as a carrier gas at 40 ml min^{-1}. The column was a molecular sieve 5A (heated in an enclosed oven to 50 °C), and the detector attached was a Varian TCD (at 200 °C, filament at 240 °C). The column prevented water vapour and CO_2 encountering the TCD. Hamilton side port 1ml 'Gas Tight' syringes were used for injections (from Sigma-Aldrich UK),. During typical experiments, a 0.5 ml sample was taken from the reactor and injected into the GC. A typical run would take 10 minutes and would show separate peaks for H_2, O_2, and N_2 where N2 was used as an inner reference to indicate there is not leaking from the air.

The procedure of the polymeric photocatalysts for CO_2 photoreduction was detailed in Chapter 6 as it is more complicated than water splitting.

4. Oxygen and nitrogen linked heptazine polymers (ONLH) for highly efficient H_2 production from water

This chapter would mainly discuss the development of novel polymeric photocatalyst, oxygen-nitrogen linked heptazine (ONLH), synthesised via a linker-controlled polymerisation process. This new polymer exhibits excellent hydrogen production ability with a benchmark AQY in the long wavelength region (500 – 800 nm) and works in a Z-scheme system for water splitting. Some contents in this chapter are reproduced with permission from my own published work ref. 67. Copyright 2017 The Royal Society of Chemistry

4.1 Introduction

To build up a Z-scheme, Search for efficient half reaction photocatalysts remains the crucial targets, which should meet the band position requirement for water splitting, and also possess the ideal properties of being efficient, robust and low-cost.[18] As reviewed in Chapter 2, since the demonstration of stable, visible light-driven H_2 production from water on polymeric graphitic carbon nitride (g-C_3N_4) in 2009, polymeric photocatalysts have attracted much attention, and

have stimulated recent studies of covalent organic frameworks and porous organic polymers.[22-23, 162-163] Among these polymers, g-C_3N_4 is arguably the most stable photocatalyst thermodynamically and optically for H_2 production and solar energy storage.[164] Very recently it has been demonstrated that with proper co-catalysts, g-C_3N_4 could split water into H_2 and O_2.[35, 99] However, the current energy conversion efficiency on g-C_3N_4 is moderate due to its large band gap and fast charge recombination.[165] Thus many efforts have been made to improve the performance of g-C_3N_4 for H_2 production, which can be incorporated in a Z-scheme for pure water splitting. Some successful examples of efficient g-C_3N_4 for H_2 production includes g-C_3N_4 nanosheets, crystalline g-C_3N_4, cyanamide-defected g-C_3N_4 and highly-polymerised g-C_3N_4, which all still possess relatively wide band gaps near 2.7 eV, limiting the light absorption to just a small portion of visible photons (< 460 nm).[38, 51, 53, 65] Other approaches such as element doping, reduced crystallinity, copolymerisation, introduction of carbon quantum dot sensitisers and nitrogen defects were reported to shift the overall absorption towards longer wavelengths. [6, 46, 48, 54-56, 59-60,68] However the AQY was still not satisfactory, which might be due to defect-based recombination centres induced by the doping. Therefore

an effective strategy to both improve the utilisation of visible light photons combined with excellent charge separation is urgently needed.

In the rational design of materials, theoretical prediction is widely used to facilitate the experimental research by providing beneficial guidance. For example, the density of states (DOS) calculations indicated that substitutional doping of N into TiO_2 instead of interstitial doping is effective for photocatalysis and hence these target materials were successfully synthesised accordingly.[36, 166] Calculations of functionalised surfaces also directed a synthetic route for producing high-energy facets, which already influenced photocatalytic activities.[167-168] Although doping is an efficient approach to manipulate the band structure of a semiconductor, different doping positions always cause different consequences for the final physical and chemical properties. For example, as mentioned above, substitutional doping by N in TiO_2 generates an efficient photocatalyst driven by visible light, but interstitial doping by N does not have a positive effect.[166] Another example is Cr-doped $SrTiO_3$. $(Sr_{0.95}Cr_{0.05})TiO_3$ exhibited 100 times higher activity than $Sr(Ti_{0.95}Cr_{0.05})O_3$.[169] Extending this approach from crystalline semiconductors to polymeric materials and

developing the strategy of controlling doping position for a polymer based on the benchmark photocatalyst g-C_3N_4 are both novel and challenging. In this study, modelling was first used to predict the effect of doping position in g-C_3N_4 on light absorption and charge separation. The calculation results indicate that the band gap and band positions of the polymer are determined by the nature and distribution of the linker species between heptazine units. The linking of heptazine units can be controlled during the polymerisation process.[2, 90] Inspired by such knowledge, I have been experimentally successful in controlling the linker species in a polymer via a monomer-directed polymerisation strategy in this chapter. This oxygen and nitrogen linked heptazine-based polymer (ONLH) exhibits an outstanding response to UV up to near-IR irradiation (~800 nm) which clearly distinguishes it from other reported polymers and leads to a 25 times higher HER than my reference polymeric photocatalyst g-C_3N_4 under visible irradiation (λ > 420 nm) together with a high AQY of 10.3 % at 420 nm.

4.2 Methodology

4.2.1 Materials Synthesis

In a typical ONLH synthesis, 80-120 g of semicarbazide hydrochloride was placed in a lidded high-quality alumina crucible, then placed inside a muffle furnace and heated at a ramp rate of 5^{o}C/ min, and finally held at 500, 550 and 600^{o}C for four hours. The products were denoted as ONLH-500, ONLH-550 and ONLH-600. For comparison of photocatalytic activity, the widely used dicyandiamide-derived g-C_3N_4 was synthesised according to the literature by heating dicyandiamide (DCDA) at 550^{o}C for 4 hours at a ramp rate of 2.3 ^{o}C/min.[157] Water, HCl, and NaOH were used to wash the produced powders to remove all unreacted and potentially detrimental surface species.

4.2.2 Photocatalytic analysis

In a typical H_2 evolution reaction, a certain amount of photocatalyst with 5 w.t.% of Pt (H_2PtCl_6 as a precursor) was well dispersed in a 50 ml aqueous solution containing 10 vol.% TEOA as a sacrificial electron donor which was combined inside a 130 ml

top-irradiated photoreactor. The reactor was sealed, purged with Argon gas (99.99%) for 1 hour and then irradiated using a 300 W Xenon light source (Newport 66485-300XF-R1) to photodeposit the Pt co-catalyst. During the photodeposition, periodic measurements were taken to determine if hydrogen was produced at a stable rate to make sure the photodeposition occurred correctly. The reactor was then re-purged with Argon before irradiation under either full arc or visible irradiation with different filters (Comar Optics).

4.2.3 Computational method

Candidate structures for g-C_3N_4 and ONLH were modelled as three-dimensional periodic structures, using density-functional theory calculations as implemented in the CRYSTAL09 software by my collaborator Dr Natalia Martsinovich at the University of Sheffield.[170-171] The hybrid B3LYP exchange-correlation functional was used, together with all-electron basis sets: 6-21G* for C and N,[172] 6-31G* for O,[5] and 31G* for H.[173] Dispersion interactions between the layers were described using Grimme's D2 correction.[174] A 2×2×2 **k**-point grid (8 **k**-points) was used in all

optimisation calculations, while an 8×8×8 **k**-point grid (reduced by symmetry to 260 **k**-points) was used in all density of states (DOS) calculations. Full cell optimisation was performed for all structures; no symmetry was applied. Vibrational frequencies and infrared (IR) intensities were calculated using CRYSTAL14 software,[175-176] for g-C_3N_4 and the proposed model of ONLH. IR absorption spectra were simulated from these frequencies and intensities by superposition of Lorentzian peaks. The damping factor (the parameter characterising peak width) was chosen as 50 cm^{-1} in the region 500-2500 cm^{-1}, and 200 cm^{-1} in the region 2500-4000 cm^{-1}. Molecular orbital plots were calculated using CP2K software for structures optimised using CRYSTAL09, using the same B3LYP functional, auxiliary density matrix method (ADMM) method for calculating Hartree-Fock exchange part of the hybrid functional, with Goedeker-Teter-Hutter pseudopotentials, double-zeta valence polarised (DZVP) scalar-relativistic basis sets and auxiliary pFIT3 basis sets for the Hartree-Fock exchange calculations. [177-180]

4.3 Results and discussion

4.3.1 Theoretical prediction

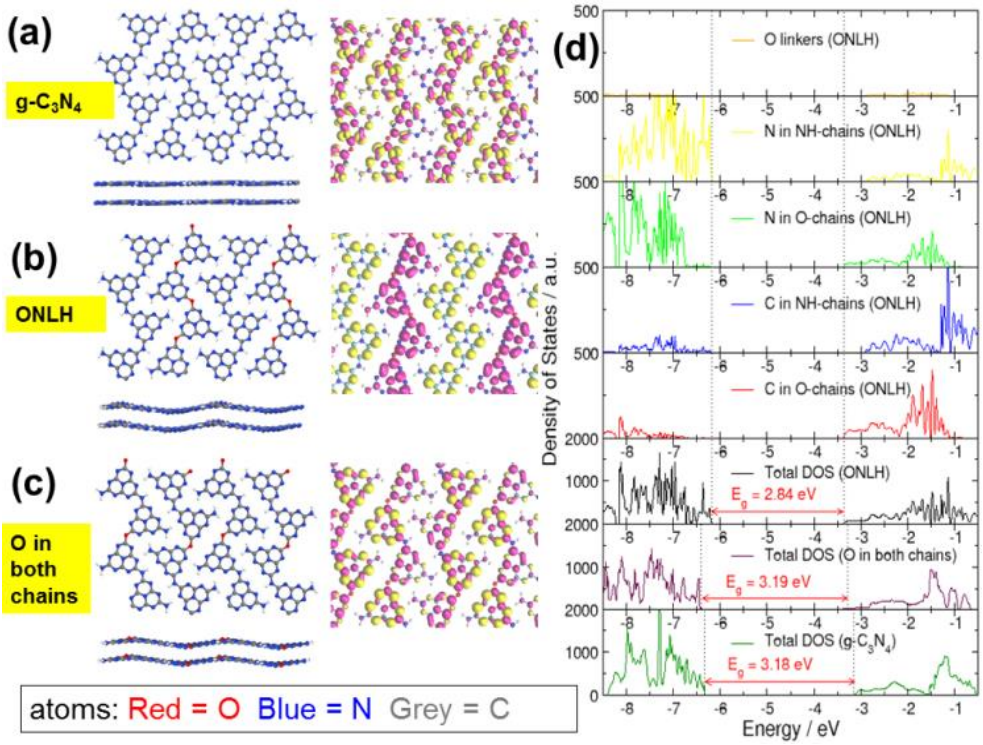

Figure 13. (a-c): g-C_3N_4, ONLH and the structure with O linkers in both chains. Left: proposed structures of g-C_3N_4 and ONLH according to DFT calculations (front and side views). Middle: their highest occupied molecular orbitals (yellow) and lowest unoccupied molecular orbitals (pink), (d) total density of states of g-C_3N_4 (lowest panel), oxygen-containing material with O atoms placed equally in both chains (second-lowest panel) and ONLH (third-lowest panel) and density of states projected on N, C and O atoms in different chains in ONLH (upper 5 panels).

As outlined in the Introduction, doping can have a dramatic effect on the electronic structure and optical absorption of host materials, and computational modelling can be used to explore

hypothetical doped structures before attempting to synthesise them. Here, DFT calculations were performed to predict the effect of oxygen doping in g-C_3N_4, the layered two-dimensional polymeric heptazine-based material (see computational details). The calculations indicate an oxygen-doped structure containing two types of heptazine chains linked by oxygen linkers (O-chain) and nitrogen linkers (NH-chain). Only the doped structure with both O-chain and NH-chain is stable, non-planar and has a reduced band gap compared to g-C_3N_4 (Figure. 13a-c). Density of states (DOS) plots (Figure. 13d) explain the origin of the band gap narrowing: in this O and NH co-linked structure, the top of the valence band (VB) and the bottom of the conduction band (CB) are spatially separated: the VB top is dominated by heptazine N atoms of the NH-chains, while the CB bottom is composed of nitrogen and carbon states of the O-chains and is shifted to more negative energies (lower CB position) compared to the CB of pure g-C_3N_4. This means that the O-chains overall have an acceptor character, while the NH-chains have a donor character (similar to the recently reported polymeric donor-acceptor photocatalysts).[181] Oxygen atoms themselves make negligible

contributions to the VB and CB (Figure. 13d) but cause the down-shift of the CB edge. This gap narrowing and charge separation is not observed if O atoms are placed equally in both chains (Figure. 13c and d). Thus, it is the co-existence of the two types of chains (or distinct N-rich and O-rich regions), rather than O atoms themselves, that give rise to the gap narrowing.

Furthermore, molecular orbital plots in Figure. 13 illustrate this principle: in g-C_3N_4 and the O-doped structure with O placed equally in both chains, the highest occupied molecular orbital (the HOMO, or the top of the VB) and the lowest unoccupied molecular orbital (LUMO, or the bottom of the CB) are spread equally over all chains. In contrast, in the ONLH structure with two inequivalent chains, the HOMO is localised on the NH-linked chains, and the LUMO is localised on the O-linked chains. Therefore, apart from the reduced band gap, the spatial separation of photogenerated electrons and holes in ONLH is likely to reduce electron-hole recombination. In other words, ONLH has the potential to solve the key drawbacks existing in the benchmark g-C_3N_4. Also, it is statistically unlikely that some chains will contain only oxygen linkers and others only nitrogen linkers; it

is, on the other hand, likely that many O-linked and N-linked regions are formed in a disordered manner, and act as electron-accepting and electron-donating regions. Again, the donor-acceptor nature of ONLH is expected to give rise to separated photoelectron and photohole states, which should lead to a dramatic enhancement in charge separation efficiency and visible light utilisation.

According to the theoretical prediction, such as oxygen and nitrogen co-linked heptazine polymer is a promising candidate for photoredox reactions. Therefore, I need to design a polymerisation pathway to prepare such a material carefully.

4.3.2 The synthesis and characterisations of the predicted polymer

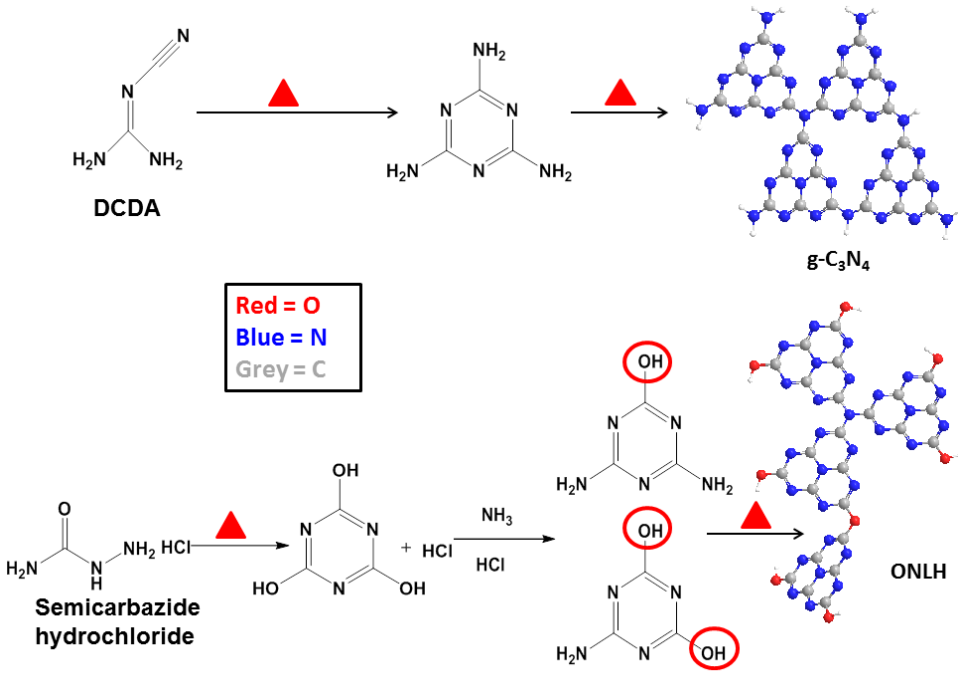

Figure 14. Proposed mechanism of the reaction paths for the formation of polymeric g-C_3N_4 and ONLH

Inspired by theoretical predictions, I controlled the polymerisation pathway and succeeded in synthesising the oxygen and nitrogen co-linked heptazine (ONLH) from semicarbazide hydrochloride ($NH_2CONHNH_2HCl$), via a one-pot polycondensation route (Figure 14). Samples synthesised at different temperatures (500, 550 and 600 °C) are noted as ONLH-500, ONLH-550 and ONLH-600. For comparison, the widely used

dicyandiamide-derived g-C_3N_4 was synthesised according to the literature.[157] To confirm the structure of my new polymer, a systematic process of material characterisation was undertaken. From elemental analysis (EA), the bulk atomic stoichiometry of ONLH was found to be $C_3N_{4.4}O_{0.3}H_{2.1}$(ONLH-500), $C_3N_{4.3}O_{0.4}H_{1.9}$(ONLH-550) and $C_3N_{4.3}O_{0.5}H_{1.8}$(ONLH-600), while g-C_3N_4 was noted as $C_3N_{4.5}O_{0.1}H_{1.6}$ (Table 3), showing less nitrogen and much more oxygen in the new polymer. As the polymerisation temperature increases, the amount of O in ONLH goes up, indicating more O species exist in the polymers' structure at high temperatures.

Table 3. Summary of the properties of ONLH and g-C_3N_4 measured at atmospheric pressure under 120 mW/cm^2 Xe irradiation

Samples	Composition	Surface area / $m^2\ g^{-1}$	Bandgap / eV	HER/μmol h^{-1}	
				>420 nm	Full arc
ONLH-600	$C_3N_{4.3}O_{0.5}\ H_{1.8}$	32.9	1.55	10.2	25.79
ONLH-550	$C_3N_{4.3}O_{0.4}\ H_{1.9}$	16.7	1.65	2.44	7.5
ONLH-500	$C_3N_{4.4}O_{0.3}H_{\ 2.1}$	14.6	1.80	1.00	3.9
g-C_3N_4	$C_3N_{4.5}O_{0.1}H_{\ 1.6}$	13.8	2.72	0.4	2.0

Powder X-ray diffraction (PXRD) (Figure 15. a) was used to compare the crystal structure of ONLH-500, -550, -600 and reference g-C_3N_4. The peaks at 13.0° in ONLH samples, attributed to the approximate dimension of heptazine units, exist at the same

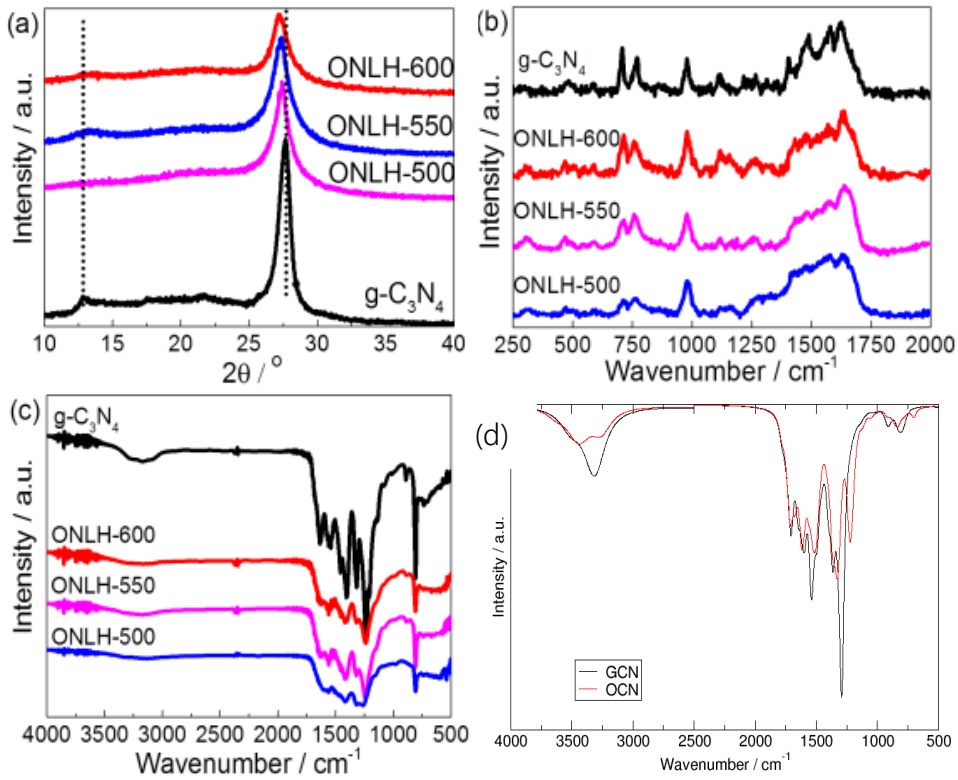

Figure 15. Characterisation of ONLH and g-C_3N_4: (a) powder XRD pattern, (b) Raman spectra (325 nm excitation), (c) FT-IR spectra, (d) Calculated IR spectra of ONLH and g-C3N4, with the low-frequency region (below 2500 cm-1) broadened with the Lorentzian parameter 50 cm^{-1}, and the high-frequency region (above 2500cm^{-1}) broadened with Lorentzian parameter 200 cm^{-1}. The large broadening for the N-H stretch region is probably due to a variety of arrangements available to the NH_2, NH and OH groups, while the C-N framework is more rigid..

position as that in g-C_3N_4 but are generally much weaker, inferring the conjugated system in ONLH polymers might not be as well-defined as that in g-C_3N_4.[68] The peak at 27.4° for g-C_3N_4 is

assigned to the interlayer stacking distance (0.326 nm).[68] As the oxygen concentration in ONLH goes up, this peak shifts left and reached 27.1° (0.329 nm) in ONLH-600, indicating the oxygen species account for the enlarged space between ONLH layers. The widened layer-to-layer distance is consistent with the distorted structure inferred from modelling of g-C_3N_4[22] and of ONLH. Through Raman spectroscopy (Figure 15.b), the heptazine structural backbone was confirmed in ONLH polymer. The main peaks in the Raman spectra (from 1200 to 1700 cm^{-1}) correspond to the dominant C-N stretching vibrations. The peaks at 980 cm^{-1} and 690 cm^{-1} matches well to the symmetric N-breathing mode of heptazine units, and the in-plane bending vibrations of the tri/heptazine CNC linkages, respectively.[61] The ONLH structure appears a little more disordered because the peaks are not as

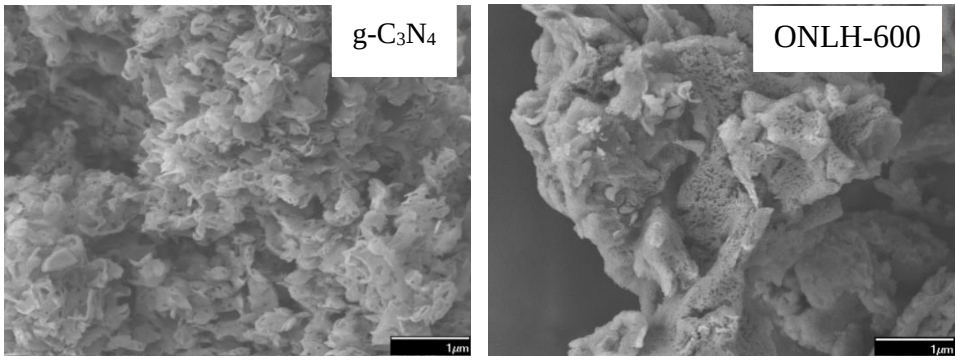

Figure 16. SEM images of g-C_3N_4 and ONLH-600. Both are porous and sheet-like materials.

intense as those of g-C_3N_4, correlating with the XRD results. Scanning electron microscopy (SEM, Figure 16) indicates a sheet-like structure for both materials, however, ONLH appears more porous, consistent with its high surface area(Table 3).

Furthermore, the FT-IR spectra (Figure 15.c) support the assignment of the ONLH structure. The peaks of ONLH are generally much broader and less sharp than for g-C_3N_4 due to having more C-O bonds in addition to C-N and due to a greater disorder in the structure. This difference between g-C_3N_4 and ONLH is consistent with the modelling results of IR spectra (Figure 15.d). The most solid evidence concerns the peaks between 3000-3300 cm^{-1} in g-C_3N_4, assigned to the stretching modes of the -NH_x moieties,[38] which transforms into a very broad low-intensity band assigned to -OH species in ONLH samples. Moreover, the C-N peaks at 1202 and 1455 cm^{-1} in g-C_3N_4[182] (Figure 15. c) are much less prominent in the FT-IR spectra of ONLH samples, indicating less C–NH_x bonding in ONLH. This is consistent with two intense peaks (1290 and 1540 cm^{-1}) in the calculated IR spectrum of g-C_3N_4, whose intensity is greatly reduced in ONLH (Figure 15.d). All these FT-IR features confirm that there are fewer

C–NH_x species and more C-O and C–OH species in the ONLH samples compared with those in g-C_3N_4. The FT-IR spectra also rule out some alternatives, such as C=O groups, because no sharp peak is observed in the ~1700 cm^{-1} region of the spectrum shown in Figure 15.c.

X-ray photoelectron spectroscopy (XPS) was used to investigate the chemical states of the elements in these materials (Figure 17 and 18.a). Consistent with the EA results, higher O and

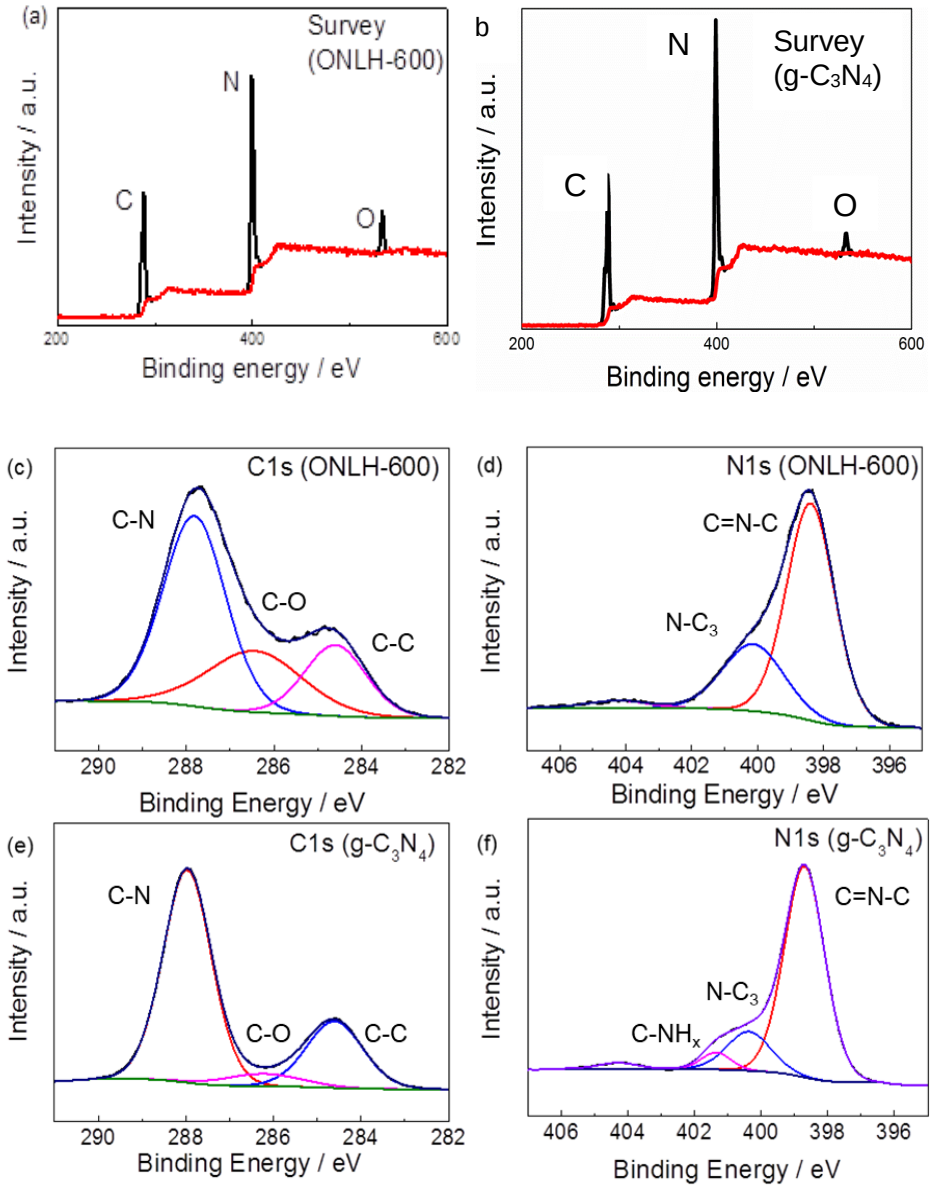

Figure 17. XPS spectra: C1s and N1s spectra (a)-(d) and survey spectra (e-f) of ONLH-600 and g-C_3N_4.

lower N percentages were found in ONLH samples compared to g-C_3N_4 according to the survey spectra of the etched samples (Figure 17. a and b). No chlorine content was observed, meaning no residual Cl species from the precursor remain in ONLH. In the O1s XPS spectra of ion etched g-C_3N_4, the only obvious peak at 532.5 eV is assigned to adsorbed H_2O.[22, 38] In etched ONLH, two new peaks at 531.5 eV and 533.2 eV are observed, which were attributed to C-OH and C-O-C species (Figure 18.a).[4-5] The C1s spectra for both samples (Figure 17. c and d) exhibit 3 main peaks

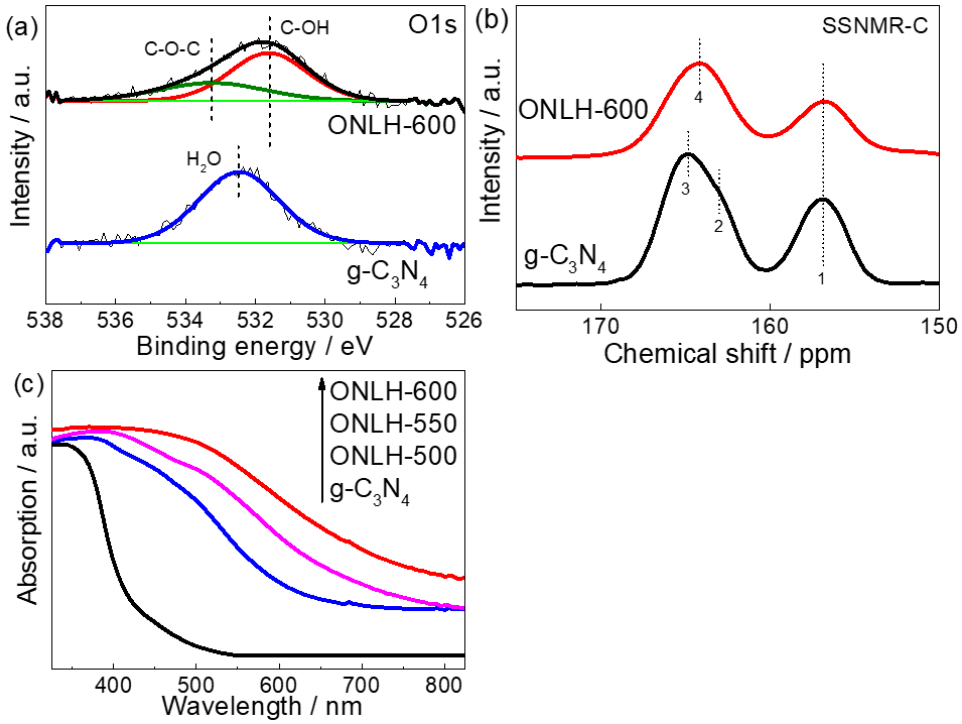

Figure 18. Characterisation of ONLH and g-C_3N_4: (a) O1s XPS spectra of etched samples, (b) 13C solid state nuclear magnetic resonance (ssNMR) spectra, (c) UV-vis spectra.

at 288.0 eV (N=C-N), 286.2 eV (C-O) and 284.6 eV (C-C).[38] Specifically, the peak at 286.2 eV (attributed to C-O)[183] is very weak in g-C_3N_4, suggesting only slight contamination with oxygen groups, but is much more intense in ONLH, indicating that a large number of carbon atoms are bonded to O atoms, forming C-O bonds. By comparison, C=O bonds cannot be responsible for the increased peak at 286.2 eV, because they are expected to give C1s peaks at higher binding energies (287.0-288.0 eV) than C-O (285.5-287.0 eV)[184-185] in a similar range to N=C-N.[183] The N1s spectra illustrate the bonding situation of N in g-C_3N_4, with peaks at 398.7 eV, 400 eV, 401 eV and 404 eV which are assigned to heptazine C=N-C, N-$(C)_3$, -NH_x and π excitation of the C-N conjugated structure, respectively (Figure 17 e and f).[22, 38] However in ONLH there are only 3 obvious N1s peaks, while the NH_x peak at 401 eV becomes very small. No new N1s peaks appear in ONLH, inferring that no new chemical state of N appears, i.e. N is not directly bonded to O. This decrease of terminal and linking -NH_x species, together with increasing C-O, indicates that the oxygen moiety in ONLH (C-OH and C–O-C) might be located at the -NH_x positions of g-C_3N_4. In other words, there are many –OH terminals

and C-O-C linkages in the new polymer, resulting in an O/N-linked structure of ONLH (i.e. a mixture of both O and N linkers instead of all N linkers), similar to the computational model. The possibility of O-doping into the heptazine unit which was proposed/ hypothesised before,[6] is excluded since the features of heptazine remain unchanged, both in the Raman, XRD and XPS characterisation, and the only remarkable difference is that ONLH exhibits decreased -NH_x groups and emerging C-O signals. On the other hand, doping into heptazine might result in issues concerning the stability of the polymer, which should be avoided.

Carbon-13 solid-state nuclear magnetic resonance (^{13}C ssNMR) was used to identify the structural differences (Figure 18.b). The signals at 157 ppm in both samples were assigned to CN_3 moieties.[39] However, the low field signals related to $CN_2(NH)$ and $CN_2(NH_2)$ at 163 and 165 ppm for g-C_3N_4 (C bonded to linker N)[39] shifted to 164 ppm in ONLH. Moreover, both high and low field signals in ONLH are broadened compared to g-C_3N_4. These changes are indicative of increased disorder in the system; especially the shift in the high field signal indicates a change in the nature of the linker atoms – this is attributed to fewer NH_x species

and to the presence of additional O linkages and terminal groups in ONLH, which influences the chemical environment of carbon.[39]

The UV-vis spectra of the ONLH samples reveal a dramatically strong red-shift into the IR region (Figure 18.c). Compared with typical g-C_3N_4 with a bandgap of 2.7 eV, much narrower band gaps were determined for ONLH using a Tauc plot (Figure 19 a and Table 3). The band gap narrowing is consistent with the theoretical modelling results, which predict band gap reduction in ONLH due to the NH-linked and O-linked regions respectively, and a consequent down-shift of the CB (Figure 13 d). In the UV-vis absorption spectrum of g-C_3N_4, the band gap absorption around 400 nm is assigned to the characteristic π-π* transitions in heterocyclic aromatics, while the long wavelength absorption is due to the n-π* electronic transitions involving lone pairs of electrons, which is forbidden in a planar structure but allowed in distorted polymeric units.[61] Therefore, the ONLH material has a disordered nature as demonstrated by all my characterisation results. This disorder is also likely to give rise to separated electron and hole states with energies in the band gap, leading to the Urbach tail in the optical absorption spectrum which further

broadens the absorption. My calculations, which were performed in a periodic unit cell, cannot fully capture this disorder and the sub-band states, and therefore are unable to reproduce the Urbach tail; therefore, the ONLH absorption is expected to be red-shifted compared to the calculated gap. A higher concentration of oxygen in ONLH results in more distorted structures, and thus narrower band gaps (Table 3), again indicating the oxygen moieties are responsible for the shift in absorption.

The increased interlayer distance seen in the XRD pattern of ONLH (Figure 15.a) can be ascribed to the O linkers being away from the planar structure, causing structural distortion. The lower intensity of the peaks of ONLH in the XRD and Raman spectra (Figure 15. b) is also due to the disruption of conjugation between

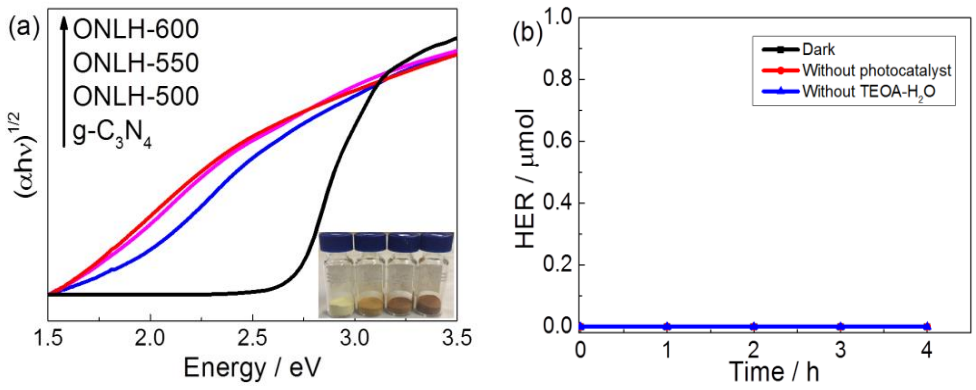

Figure 19. (a) Tauc plot of ONLH samples. (b) Hydrogen evolution rate under control conditions (> 420 nm) of ONLH. No activity is detected under dark condition or without photocatalyst or without sacrificial regent. (c) Hydrogen evolution rate under control conditions (> 475 nm) of ONLH-600 and g-C_3N_4.

neighbouring heptazines, caused by oxygen linkers. From FT-IR (Figure 15.c) and XPS spectra on etched samples (Figure 17 and Figure 18 a), the decrease of $–NH_x$ is confirmed, and the oxygen species in bulk ONLH are identified to be C-OH and C-O. The much broader absorption of ONLH polymers in the UV-vis spectrum (Figure 18 c) is due to more distorted structures caused by the new oxygen linkers. Considering the heptazine backbone similarity confirmed by XRD and Raman together with the information from XPS, NMR and FTIR, one can conclude that the structure of the synthesised ONLH material corresponds to the computationally proposed structure shown in Figure 13b, in which oxygen and nitrogen species link together the heptazine units. This structure has C–O bonds present as ether-type (C–O–C) linkages, replacing some of the –NH– linkers and thus causing a reduction in the number of $–NH_x$ groups, while the heptazine rings are preserved intact.

4.3.3 The evaluation and original of superior H_2 evolution

Following the successful preparation of the predicted materials, their photocatalytic hydrogen evolution rates were

tested in the presence of a Pt co-catalyst (5%) and TEOA sacrificial electron donor, which is widely used to assess the activity of polymeric photocatalysts. No hydrogen was detected in the dark or without photocatalyst or TEOA (Figure 19.b). It is noted that the H_2 evolution rate measured here on g-C_3N_4 is smaller than reported in a few papers, [65, 69] which is due to a closer to practical environmental condition used in the study (*e.g.* 1 bar pressure of inert gas in the reactor instead of vacuum conditions and weak while close to one sun intensity (120 mW/cm^2). The majority of studies reported on H_2 evolution by polymeric photocatalysts were carried out under circulation-vacuum conditions (~0.1 bar) which would dramatically improve the energy conversion efficiency by suppressing the back reaction.[116] Under the ambient condition, ONLH-600 exhibits *ca.* 25 times higher activity under

visible light irradiation (>420 nm) than g-C_3N_4[157] (Figure 20.a and Table 3). Furthermore, when a 475 nm bandpass filter was used (Figure 20.c), ONLH-600 shows good photocatalytic activity, however, the benchmark g-C_3N_4 is not active at all. It is also found that ONLH synthesised at different temperatures, and compared to g-C_3N_4, exhibit a positive correlation between O amount and HER as shown in Figure 20.a and Table 3. Under these ambient and fairly practical reaction conditions, the measured, stable AQY of ONLH-600 calculated after five runs is 10.3% (at 420 nm),

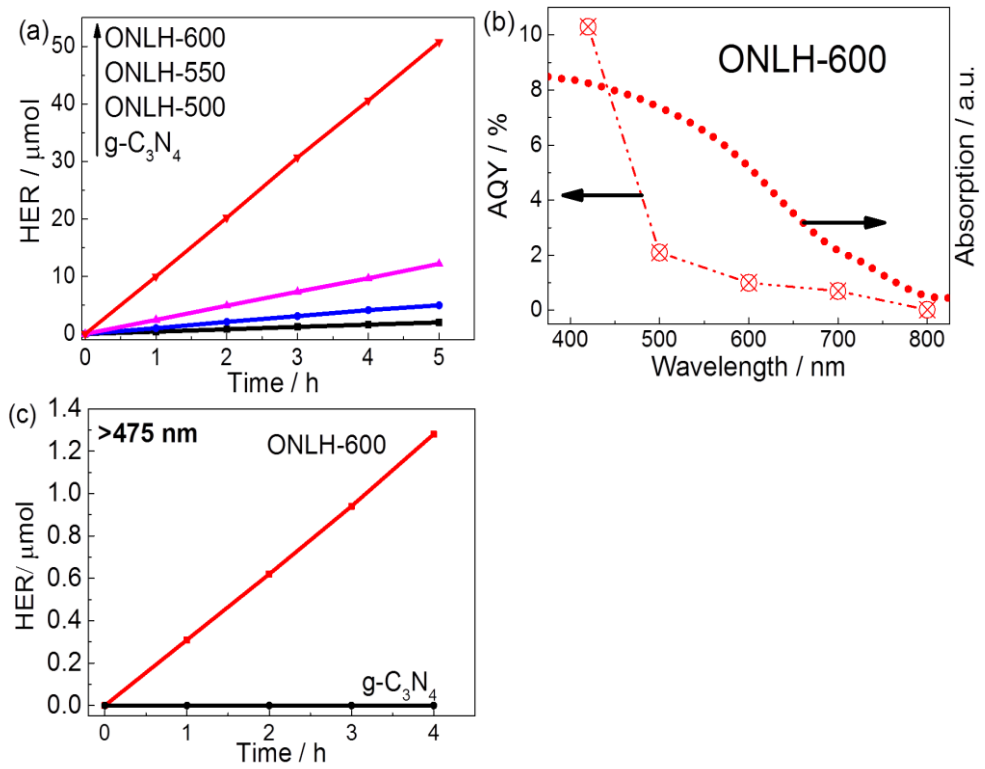

Figure 20. (a) Hydrogen evolution rate (HER) and (b) apparent quantum yield (AQY) of ONLH-600 measured at atmospheric pressure under nearly one sun irradiation condition.

corresponding to one of the highest AQYs reported for polymeric photocatalysts measured under 1 atmospheric bar pressure (Table 1).[25, 53-54] An unprecedented AQY of 2.1% at 500 nm has also been achieved and the polymer even shows activity at long wavelengths extending into the IR region (Figure 20.b).

It is proposed that the pathway of O-terminal/linker formation is related to the acidity of the precursor material $NH_2CONHNH_2HCl$. As shown in Figure 14, during the thermal polymerisation process, $NH_2CONHNH_2HCl$ forms cyanuric acid and liberates ammonia gas.[2] Normally, the next step of melamine formation is a dehydration process by replacing –OH species at monomer terminals by NH_3.[2] However, during the polymerisation of $NH_2CONHNH_2HCl$, HCl gas is also evolved in the thermal condensation process and can react with NH_3, thus competing with the –OH terminals for NH_3. Because of the interrupted ideal melamine formation (due to lack of NH_3), a certain amount of -OH terminals remains connected to the monomers. Some –OH terminals on heptazine units react with each other to release H_2O and form C-O-C linkages, still forming a polymeric system but with a distorted structure instead of a planar one. The hydrochloric

acid released in-situ is the key to protect the –OH species during the process. The pathway should be an oxygen-maintaining process rather than a subsequent replacement process because these O species exist in the precursor. The proposed mechanism leads to the structure of ONLH which agrees well with all of my experimental characterisations and computational modelling.

Thus the doping position is controlled as shown in ONLH in Figure. 13, which is very challenging, resulting in higher photocatalytic activities compared to other polymeric photocatalysts reported in the literature (see Tables 1). Any doping into the heptazine ring either makes only small changes to the bandgap or causes concern over the stability of the modified polymer, as proven by recent reports from different groups, summarised in Table 1. The importance of the doping position is again emphasised by comparison with another O-containing carbon nitride polymers, obtained by H_2O_2 post-treatment of g-C_3N_4.[6] In those reports, oxygen doping was believed to occur in the heptazine units, rather than in the linker positions, as in ONLH. As a result, its electronic properties (band gap *ca.* 2.49 eV) exhibited only a moderate narrowing compared to pristine g-C_3N_4

(2.70 eV).[6] The prominent differences between the band gaps of H_2O_2 treated g-C_3N_4 and ONLH (1.55 eV) strongly suggest that the oxygen linkers in the bulk of the material are essential for achieving a narrow bandgap and more efficient visible light-driven photocatalytic activity.

To further investigate the reasons for the dramatic increase in H_2 evolution by ONLH, photoluminescence (PL) spectroscopy was undertaken using a 325 nm laser probe (Figure 21.a). The PL signal peaks around 450 nm and 500 nm are assigned to the π-π* transitions and n-π* emission, respectively.[61] Strikingly, the PL intensity of ONLH is roughly two orders of magnitude lower than that of g-C_3N_4 in this region, which indicates that radiative electron-hole recombination is dramatically suppressed in ONLH, consistent with the DFT results. This, to some extent, explains the higher HER of ONLH, caused by the spatially separated electron

donor and acceptor regions brought about by the N- and O-linked regions.

To determine the CB and VB positions for the polymers and their thermodynamic driving force for water splitting, valence band XPS measurements were carried out (Figure 22.b). The spectra of ONLH and g-C_3N_4 are similar in shape. However, the edge of ONLH shifted to lower binding energy compared to g-C_3N_4. Using evidence from both the valence band XPS and UV-vis absorption spectra, one can see that the VB of ONLH shifts

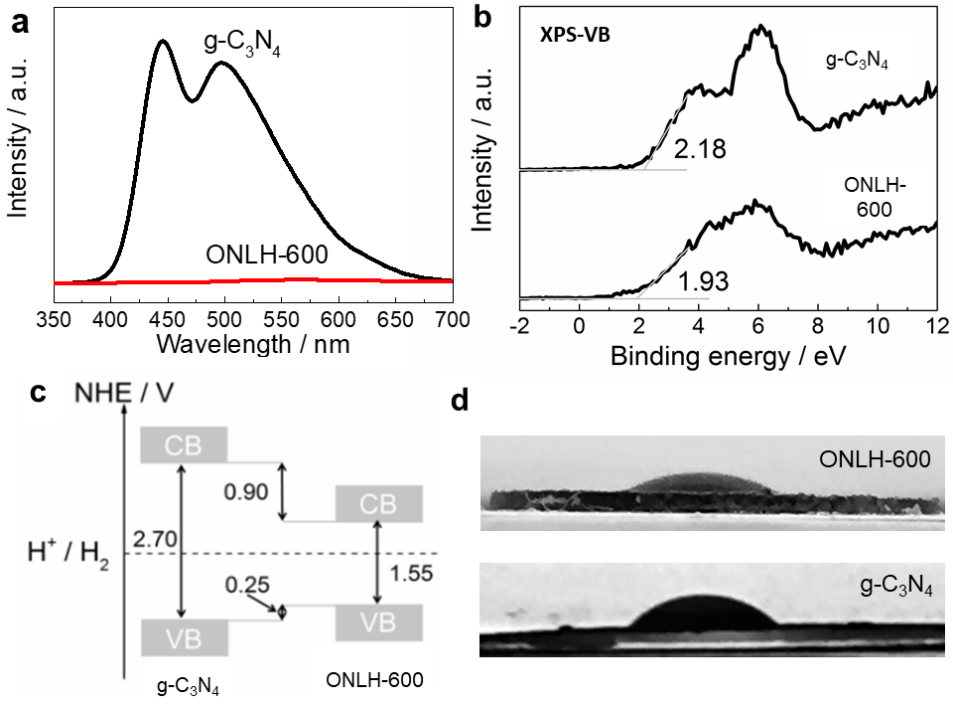

Figure 21. (a) Photoluminescence spectra (325 nm laser excitation) and (b) band alignment of both g-C_3N_4 and ONLH; (c) the differences in hydrophilicity between ONLH and g-C_3N_4 using contact angle measurements. (d) Valence band (VB) XPS spectra of ONLH-600 and g-C_3N_4

upward (more negative potential) by 0.25 eV and CB moves downward (more positive potential) by 0.9 eV compared to pristine g-C_3N_4 (Figure 22.c). This narrowing of the band gap ensures greater solar absorption but still exhibits sufficient overpotential to drive proton reduction to H_2. This is in addition to the improved charge separation illustrated by PL measurements and theoretical modelling.

I also tested the surface hydrophilicity of the new polymer ONLH-600. Interestingly the active polymer shows a contact angle of 32^o compared with 57^o measured on g-C_3N_4, indicating a more hydrophilic surface brought about by OH groups on the new polymer ONLH (see photos in Figure 22.d), which will improve water adsorption and subsequent proton reduction. Regarding the influence of surface area, ONLH-600 only shows twice higher surface area than the others, but HER activity is 4 to 25 times higher (Table 3). Also, the surface area of ONLH-500 and ONLH-550 is close to g-C_3N_4, but they are much more active. Therefore, surface area plays a role but is not a dominating factor in HER activity of the polymer.

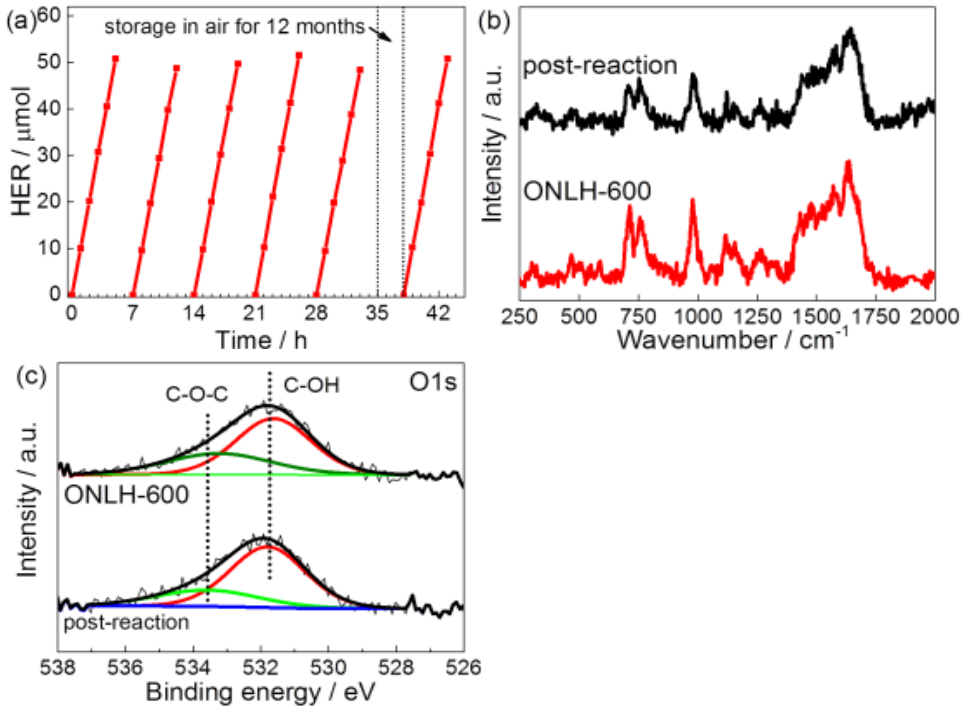

Figure 22. (a) Stability test of ONLH-600. The first five cycles were typical stability tests and the last run was measured after the sample being stored under ambient conditions for 12 months. (>420 nm irradiation) (b) Raman and (c) O1s XPS spectra of ONLH before and after photocatalytic reaction.

Stability of a photocatalyst is a key factor in determining its long-term application. I assessed the new polymers' stability in two ways. One is the widely used multi-run test, as shown in Figure 26. a. The activity of hydrogen evolution stably maintains at *ca.* 10 μmol/h. The other method is to store the polymer under ambient conditions for a year, then to evaluate its activity. It was found that the activity remains the same as the fresh sample (Figure 22.a). Post-testing characterisation further proves the stability of the

new polymer as shown by Raman and XPS spectroscopies in Figure 22.b and c.

4.3.4 Overall water splitting via Z-scheme

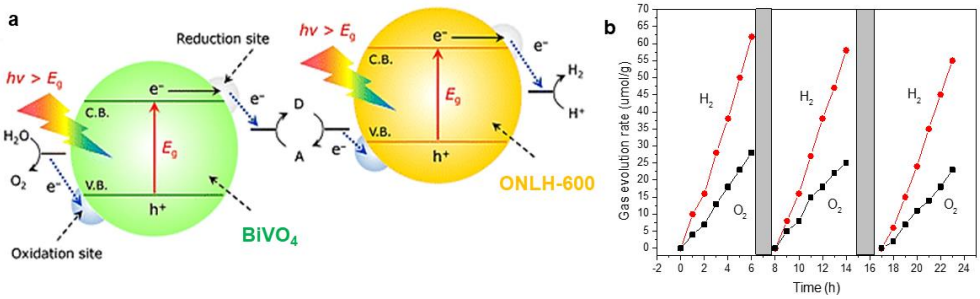

Figure 23. (a). Schematic of Z-scheme water splitting based on $BiVO_4$ and ONLH. (b). Stoichiometry H_2 and O_2 production from water splitting.

As discussed above, the final goal of artificial photocatalysis is to perform overall water splitting or CO_2 conversion. Since the developed novel polymeric photocatalyst ONLH only works for efficient H_2 production, one needs to apply another photocatalyst $BiVO_4$, for the evolution of O_2 via Z-scheme water splitting. In such a system, the holes of $BiVO_4$ oxidise water to O_2 while the electrons of ONLH reduce protons to H_2. Meanwhile, the electrons left on $BiVO_4$ transfer via the redox mediator $Fe^{2+/3+}$ to neutralise the holes on ONLH, thus completing the reaction (Figure 23 a).

50 mg 3 w.t. % Pt-loaded ONLH-600, 50 mg $BiVO_4$, Fe^{3+}/Fe^{2+} mediator (2mM, pH 2.7) was added into the 130 mL reactor and the 2:1 ratio of H_2 and O_2 was detected by GC under the 300 W Xenon lamp irradiation with a light intensity of 100 mW/cm^2. This H_2 and O_2 evolution rates are 10 μmol/gh and 4.8 μmol/gh (Figure 23 b), respectively. The STH is very moderate (approximately 0.01%). As this is a preliminary proof-of-concept system, further careful tailor of co-catalysts and surface modifiers to suppress backward reactions would be useful to improve the efficiency. The detailed characterisation of materials after the reactions also should be investigated in the future work.

4.4 Summary

In summary, an innovative strategy of linkage controlling polymerisation, predicted by DFT calculation, has been developed to synthesise a highly active, robust and narrow band-gap ONLH polymer, which addresses the key challenges facing the benchmark photocatalyst g-C_3N_4: its small optical operation window and fast charge recombination hamper its efficiency in photocatalytic H_2

evolution. Also, for the new polymer, the OH terminal groups increase hydrophilicity, overcoming one of the drawbacks of other polymeric photocatalysts. The novel ONLH exhibits *ca.* 25 times higher HER than g-C_3N_4 under visible light (> 420 nm) at atmospheric pressure and moderate light intensity. For the first time, efficient and stable photocatalytic H_2 evolution has been observed on a single polymeric photocatalyst using even near-IR excitation, resulting in a record AQY of 10.3% at 420 nm measured in harsh conditions. More importantly, and to the best of my knowledge, this is the first report of a single polymeric photocatalyst which can produce H_2 in such a wide operation window without the need of a sensitiser or a complicated junction structure, *e.g.* AQY of 2.1% at 500 nm. Importantly, its activity is highly reproducible after storage under ambient conditions for over one year. These excellent properties of the polymer are a result of reduced charge recombination, enhanced hydrophilicity and narrowed bandgap induced by oxygen linkers and OH terminals which were introduced via a well-designed synthetic pathway. ONLH is further applied in Z-scheme systems for overall water splitting to prove the concept.[14, 67, 186-187] This polymer can also be used in environmental purification. These findings not only prove the feasibility of polymers'

modification for wide spectrum photon absorption for efficient H_2 fuel synthesis but also stimulate fundamental research on the design and tunability of the photophysical properties of polymers through careful control of the polymerisation process.

5. Bandgap engineering of heptazine-based polymeric photocatalysts via linker/terminal controlling strategy

Following the development of efficient ONLH polymers for water reduction reaction, one can raise another question that how to fine control the band gap/band position of the heptazine-based polymer. This chapter further applies the linker/terminal control strategy to stepwise tune the band gap of heptazine based polymers by altering the ratio between O-linked chains and N-linked chain via a novel polymerisation process. These new polymers are fully assessed and characterised to attain a correlation between oxygen concentration, band position and photocatalytic activity.[188] Some contents in this chapter are reproduced with permission from my own published work ref. 188. Copyright 2018 Wiley-VCH Verlag GmbH & Co. KGaA, Weinheim.

5.1 Introduction

Compared with the progress in bandgap engineering of inorganic photocatalysts, there have been limited reports of the emerging organic photocatalysts (*e.g.* heptazine-based polymers and covalent organic frameworks), which are known for their suitable band positions for water splitting, low-cost, chemical stability and good tunability of their framework and electronic structures.[22-23, 71, 162-163, 189-190] Currently, the majority of organic/polymeric photocatalysts still suffer from an intrinsic wide band gap (*e.g.* ~2.7 eV for g-C_3N_4) and only responds to a limited region of the solar spectrum (< 460 nm), not matching with the strongest portion of 450~700 nm in sunlight (2.7~1.8 eV photons).[11, 38] The lack of facile bandgap engineering methods has inhibited the application of organic/polymeric photocatalysts to potential applications including the construction of Z-scheme water splitting systems. Therefore, an effective and rational polymerisation strategy to stepwise engineer precisely the electronic structure of polymers is a real need scientifically and technically.

Taking graphitic carbon nitride (g-C_3N_4 or GCN), the most widely-reported heptazine-based polymers, as an instance, the conduction

band (CB) is considered to consist of conjugated C and N 2p orbitals in the heptazine while the VB is mostly composed of the 2p orbitals of edge N atoms, resulting in a π-π* excitation band gap of over 2.7 eV.[61, 191] A disordered framework could allow n-π* excitation of the lone pair electrons on edge N atoms that is forbidden in a planar structure, which would result in a photon energy that is smaller than 2.5 eV and was reported to aid the visible light absorption.[71, 192] The previous chapter has theoretically and experimentally proved that the oxygen and nitrogen linker-controlled heptazine-based chains highly influence the polymer's electronic structure.[67] The band positions of O-linked chains are relatively more positive than those of N-linked chains. Hence the hybrid polymer consists of a lower CB contributed by the introduced O-linked chains, and a VB contributed by N-linked chains, resulting in one narrowed band gap. More importantly, the electron acceptor-donor nature between O-chains and N-chains promotes the physical charge separation for enhanced efficiency.[181] Also, the selective doping into the linker position instead of heptazine units in the polymer maintains an integrated conjugated framework and avoids additional defect-based recombination centres. However, this modified polymer

is only active for H_2 production with no activity for water oxidation under visible light irradiation.

In this chapter, based on the previous work, I developed a new approach to control precisely the band gap of organic photocatalysts, resulting into stepwise bandgap changes from 2.7 to 1.9 eV, by carefully tailoring the linker and terminal atoms among donor-acceptor domains. This fine control of band positions has been achieved by adding a different amount of formic acid as an important precursor and an innovative stoichiometry-tuned polymerisation, which provides an effective way to synthesise a series of polymeric photocatalysts with controlled electronic structures. Furthermore, this approach allows us to observe the correlation between the band positions and photocatalytic activities of polymeric semiconductors. The resultant polymers work stably and efficiently for H_2 and more importantly O_2 evolution at ambient conditions under visible light irradiation (420 nm $< \lambda <$ 710 nm). More importantly, these activities are well correlated with the band position changes of the polymers.

5.2 Methodology

5.2.1 Materials preparation

In a typical formic-acid-treated (FAT) polymer synthesis, 2 g (23.8 mmol) dicyandiamide (DCDA) (Fisher Scientific Ltd.) was firstly dissolved in 40 mL deionised (DI) water under strong stirring at 25 ^{o}C. Then a certain amount (*e.g.* 0, 0.1, 0.2, 0.5, 0.8, 1.0, 1.5 and 2.0 equivalent mol ratio to 23.8 mmol) of formic acid (Sigma-Aldrich) was added into the DCDA solution, and the solution was kept at 130 ^{o}C for 6 hours before drying overnight under violent stirring. The resultant white crystalline precursor was transferred into a lidded high-quality alumina crucible, then placed inside a muffle furnace and heated at a ramp rate of 2 ^{o}C/ min, and finally held at 550 ^{o}C for 4 h unless otherwise noted. The products were denoted as FAT-0, FAT-0.1, FAT-0.2, FAT-0.5, FAT-0.8, FAT-1.0, FAT-1.5 and FAT-2.0. FAT-0 is typical DCDA-derived g-C_3N_4. DI water, 0.1 M NaOH (Sigma-Aldrich) and HCl (Sigma-Aldrich) were used to wash the produced powders adequately to remove all unreacted and potentially detrimental surface species.

The FAT-based electrodes were prepared as below: 50 mg FAT polymer powder was added into a solution composed of 750 µL H_2O, 250 µL 2-propanol (Fisher Scientific Ltd.) and 10 µL Nafion (Fisher Scientific Ltd.) and the mixture was sonicated for 15 min. 100 µL of the resultant suspension was slowly dropped on an FTO glass. After drying under ambient conditions at 70 ^oC, it was calcined at 400 ^oC for 1 hour in a muffle furnace.

5.2.2 Photocatalytic analysis

The photodeposition of co-catalysts on photocatalysts was carried out before each photocatalytic analysis. A certain amount of photocatalysts with 3 w.t. % co-catalysts (using H_2PtCl_6 as a precursor for both half reactions) was dispersed in aqueous solution with a proper electron donor (TEOA) in a 130 mL reactor. Then the reactor was sealed, purged with Argon gas for 30 min and then irradiated using a 300 W Xenon light source (Newport 66485-300XF-R1). During the photodeposition, periodic measurements were taken to determine if hydrogen was produced at a stable rate to make sure the photodeposition occurred correctly. The sample could be directly used for hydrogen production measurement after photodeposition. In a

typical H_2 evolution reaction, 50 mg of photocatalyst with 3 w.t. % of Pt co-catalyst was well dispersed in a 50 mL aqueous solution containing 10 vol. % TEOA as electron donor inside a 130 mL top-irradiated reactor. For oxygen production, the sample is washed thoroughly until no hydrogen is produced from the suspension to remove TEOA. Then, the sample is collected by centrifuge and transferred to 50 mL of 5 mM $NaIO_3$ aqueous solution, purged, sealed and irradiated until stable O_2 evolution is observed. In a typical O_2 evolution reaction, 20 mg of photocatalyst with 3 w.t. % of PtO_x co-catalyst was well dispersed in a 5 mM $NaIO_3$ aqueous solution as electron acceptor inside a 130 mL top-irradiated reactor. The light intensity under working conditions is ~100 mW/cm^2 with a 420 nm long pass and a 710 nm short pass filter (420 nm < λ < 710 nm).These reaction conditions have been optimised including the number of powder photocatalysts, cocatalysts and solution.

Photoelectrochemical Analysis

The photocurrent of samples was measured in 0.1M Na_2SO_4 aqueous solution (pH = 6.5). Samples were illuminated from the back side (FTO substrate), and the mask-off irradiated area was 0.28 cm^2 .

Cyclic voltammetry measurements were performed at a scan speed of 10mV s^{-1}. The potentials of the working electrodes can be calculated by the formula $V_{RHE}=V_{Ag/AgCl} + 0.059pH + 0.1976V = V_{Ag/AgCl} + 0.58V$ when the pH of Na_2SO_4 was measured to be 6.5, where V_{RHE} is a potential vs. a reversible hydrogen potential, $V_{Ag/AgCl}$ is a potential vs. Ag/AgCl electrode. The Mott–Schottky curves were measured at a certain DC potential range with an AC amplitude of 5 mV and a frequency of 500, 1000 and 2000 Hz under dark condition.

5.2.3 Computational methods

All calculations have been performed, in collaboration with Fabrizio Silveri and Prof. C. Richard A. Catlow at University of Cardiff, within the DFT framework as implemented in the VASP (Vienna Ab-initio Software Package) code.[193] The electronic energy was obtained using PAW (projected augmented wave) potentials[194] and plane-wave basis set respectively for core and valence electrons, using the Perdew–Burke–Ernzerhof (PBE) functional.[195] Corrections were added to account for long-range interactions by semiempirical Grimme D3 dispersion method[196] and non-spherical contributions to the PAW potentials as natively built in the code. All energies are converged within a cutoff of

520 eV and a self-consistent electronic field (SCF) threshold of 10^{-5} eV. Convergence was determined using the tetrahedron method, implementing Blochl corrected smearing[197] and in all cases spin polarisation was disabled. The reciprocal lattice matrix was generated using a 5x5x5 K-points grid, using the Monkhorst-Pack method. The minimum energy structures were found using a built-in DIIS algorithm with a convergence force threshold of 10^{-3} eV/Å.

The band gap for the non-doped system is calculated as 1.01 eV, which underestimated the experimental value. Such results are to be expected when using a GGA level of theory such as the one employed by the PBE functional [54] and are consistent with previous literature [55]. The analysis does not, therefore, make use of band structure but focusses on the charge distribution which is expected to be reliable at this level of theory.

The unit cell for g-C_3N_4 was derived from the previous literature[198] through the Inorganic Crystal Structure Database. Each unit cell is organised in two planar layers accounting for a total of 4 linear organic chains, each composed of 2 tri-s-triazine units, 2 linker groups and 2 terminal groups. In the g-C_3N_4 (FAT-0) model, all 16 groups contain nitrogen, being modelled as -NH- for linkers and -NH_2 for terminals. In

the oxygen-doped (FAT) models, 4 such groups are modified to introduce oxygen, replacing the previous linker and terminal groups with -O- and -OH respectively. In each of the different FAT models, different groups are modified, to highlight the effect of local oxygen arrangement on the electronic properties of the material.

The definition of formation energy contributes to the understanding the energy change between graphitic carbon nitride and its O-modified homologues: it is the difference between the energy of the cell and that of its components, largely influenced by the stability of the reference systems. In particular, the N_2 bond is much stronger than the C-N bond in the polymer, resulting in positive formation energy for g-C_3N_4. On the contrary, the C-O-C and C-O-H bonds in the FAT models appear to correspond to a deeper energy well than the O_2 reference molecule, balancing the effect of N and giving a slightly negative (up to -0.11 eV/atom) formation energy to the FAT models. Ultimately, the formation energy is not a measure of the stability of the polymers relative to each other, but a measure relative to the elemental components of a system. However, it is the only way to compare the stabilities of unit cells comprising different numbers of atoms and gives a sensible reference point for the relative stabilities of the FAT polymers,

which are shown to be very similar due to the identical bonds they are comprised of, but still dependent on the O substitution due to inter-chain H-bonds.

The formation energy for each unit cell has been calculated as the difference between the energy of the supercell and the energy of the compound elements divided by the number of atoms, via the formula:

$$\Delta_f E = \frac{E_{polymer} - \sum E_i n_i}{N}$$

In which $E_{polymer}$ is the energy of the polymer supercell, E_i and n_i represent respectively the energy of an atom of each element present in the polymer in its elemental state and the number of atoms of that element in the supercell, and N is the total number of atoms in the supercell, 144 for g-C_3N_4 and 140 for all FAT models. The elemental states considered are graphite for C and their respective diatomic molecules in vacuum for H, N and O. Their energies have been calculated within suitable unit cells using the same parameters as described above for the polymers supercells.

5.3 Results and discussion

5.3.1 Material design and characterisation

The design of polymerisation pathway

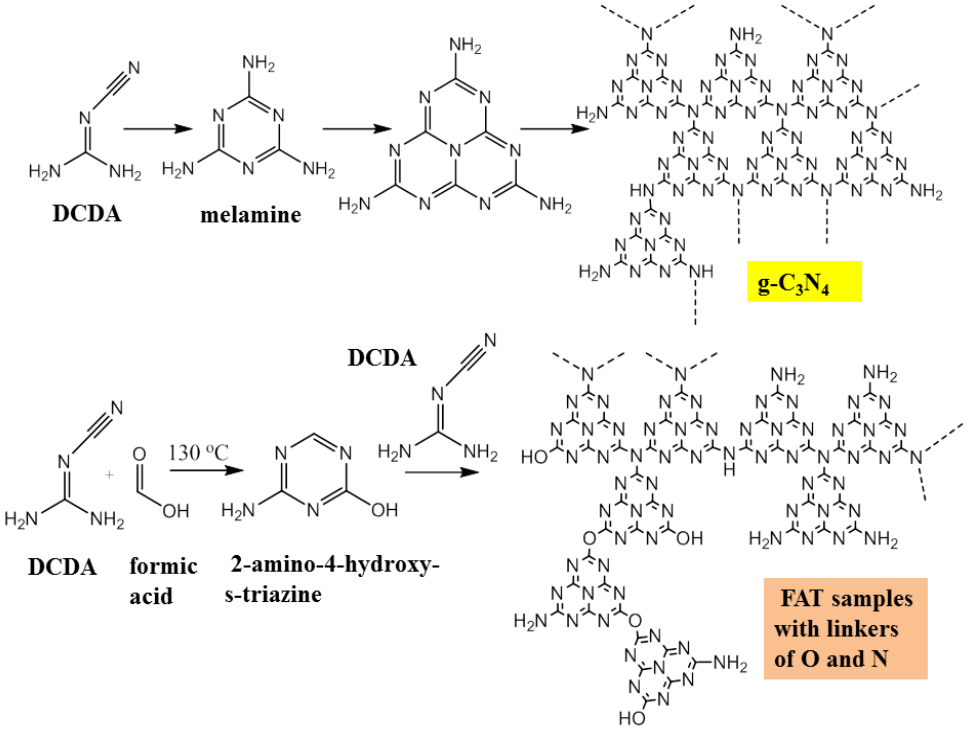

Figure 24. Polymerisation pathways of N-linked heptazine (FAT-0, g-C_3N_4) and O,N co-linked heptazine (FAT) samples [1-2]

A novel polymerisation pathway was carefully designed and controlled to engineer the band gap of the heptazine-based polymers as shown in Figure 24. As reported before, the band position shift originates from the existence of O-linked chains connected to N-linked domains, which have lower (more positively orientated) CB with an

electron acceptor nature as illustrated in the last chapter.[67, 181] The total electronic structure of such hybrid polymers consists of CB contributed by O-chains and VB contributed by N-chains, resulting in a narrow band gap. Therefore, it is very crucial to control the O-terminated heptazine monomers during the polymerisation to tailor the band gap. Different from DCDA precursor which undergoes a widely-accepted melamine-melem-melon-g-C_3N_4 pathway (Figure 24, the upper),[22] the formic acid treated precursor involves additional intermediates including hydroxyl- and amine-terminated heptazine (Figure 24, the lower) as monomers,[1-2] resulting in O-linked heptazine in the following process. Also, some unreacted DCDA molecules would form ordinary N-linked heptazine, which polymerises together with O-linked ones. By controlling the formic acid amount in the pre-treatment, the ratio between O-linked and N-linked chains and the extent of CB shift in the final produced polymers could be stepwise changed; hence the properties including the electronic structure of polymers could be tuned reproducibly and reliably.

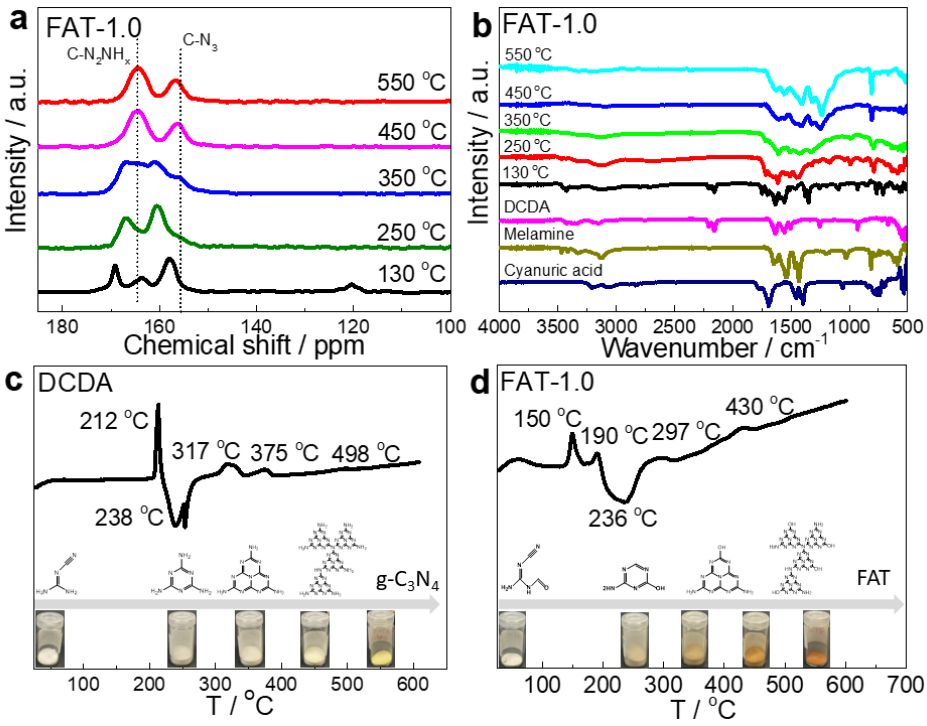

Figure 25. The characterisations of intermediates during polymerisation. (a) Carbon-13 solid-state nuclear magnetic resonance spectra, (b) FT-IR spectra of intermediates at different synthetic temperatures. Thermogravimetric analysis of (c) FAT-0 (g-C_3N_4) and (d) FAT-1.0 samples during the thermal condensation.

Such proposed polymerisation routine has been examined in detail by characterisation of intermediates. The Carbon-13 solid-state nuclear magnetic resonance (^{13}C ssNMR) of intermediates obtained at different temperatures during the polymerisation of acid-treated precursors was shown in Figure 25 a. For example, at 130 °C, the two peaks at 120 (cyano group) and 164 ppm are from the residual DCDA while those at 170 and 158 ppm are related to carbon atoms in O containing intermediates.[199-201] No polymerisation was expected at 130 °C. Thus NMR spectra show the mixture of unreacted and formic acid treated

DCDA. The composition is further confirmed by FTIR which shows the features of both DCDA and cyanuric acid. As the temperature rises from 130 °C to 350 °C, the precursor transforms from a triazine like structure to heptazine like structure because the 158 ppm peak submerges in NMR at 350 °C, indicating the inner circle carbon formation in heptazine[39] and the heptazine C-N vibration peaks (1350~1200 cm^{-1} in FT-IR Figure 25 b).[67] In the final product formed at 450~550 °C, the oxygen characters are less obvious due to a low concentration and an overlap with other species, but the broader peaks due to a disordered structure are similar to the previously reported.[67]

Thermogravimetric Analysis (TGA) and Differential Scanning Calorimetry (DSC) analysis support the proposed pathway (Figure 25 c and d). With the DCDA representing the same as the reported during thermal condensation,[22] the acid-treated precursor has two melting points at 150 °C and 190 °C corresponding to the mixture compositions in the acid-treated precursor. The FAT intermediates went through triazine around 236 °C and formed heptazine after 300 °C.[1] As observed, the polymerisation behaviour of the FAT sample is alike to g-C_3N_4 but at a lower temperature, likely owing to the pre-cyclization

at a lower temperature (Figure 24 lower) which aids the next-step polymerisation.[1] Notably, the colour of FAT intermediate starts changing from white to brown during polymerisation around 250 ^{o}C while DCDA remains white until the final step to yellow after 450 ^{o}C. Such an obvious colour change of FAT intermediates indicates that the bandgap shift due to the oxygen-containing groups appears at relatively lower temperatures in the polymerisation process.

Table 4. Summary of the properties of FAT samples measured at atmospheric pressure

Samples	Composition	N content/%	O content/%	Surface area / $m^2\ g^{-1}$	Bandgap / eV	HER / μmol $g^{-1}h^{-1}$
FAT-0	$C_3N_{4.51}H_{1.6}O_{0.07}$	49.1	0.76	5.5	2.74	44
FAT-0.1	$C_3N_{4.50}H_{1.7}O_{0.07}$	49	0.76	5.6	2.72	103
FAT-0.2	$C_3N_{4.49}H_{1.6}O_{0.07}$	49	0.76	6.7	2.69	114
FAT-0.5	$C_3N_{4.48}H_{1.6}O_{0.07}$	49	0.77	6.9	2.66	192
FAT-0.8	$C_3N_{4.44}H_{1.7}O_{0.09}$	48.1	0.98	9.9	2.06	456
FAT-1.0	$C_3N_{4.43}H_{1.8}O_{0.15}$	47.7	1.62	12.1	1.92	772
FAT-1.5	$C_3N_{4.40}H_{2.0}O_{0.25}$	45.5	2.67	16.4	2.01	656
FAT-2.0	$C_3N_{4.33}H_{2.0}O_{0.26}$	45.2	2.71	40.0	2.05	556

Characterisations of novel organic semiconductors

These bandgap tuneable polymers are synthesised at 550°C for 4 hours, and the final products are noted as FAT-X with X representing the stoichiometric ratio of formic acid to DCDA in the precursors. FAT-0 is the reference DCDA-derived g-C_3N_4. The properties of the synthesised polymers with different formic acid amounts in precursors were investigated via extensive and thorough characterisations. From elemental analysis (EA), the bulk atomic stoichiometry of eight FAT samples was found to be: $C_3N_{4.51}H_{1.6}O_{0.07}$ (FAT-0), $C_3N_{4.50}H_{1.7}O_{0.07}$ (FAT-0.1), $C_3N_{4.49}H_{1.6}O_{0.07}$ (FAT-0.2), $C_3N_{4.48}H_{1.6}O_{0.07}$ (FAT-0.5), $C_3N_{4.44}H_{1.7}O_{0.09}$ (FAT-0.8), $C_3N_{4.43}H_{1.8}O_{0.15}$ (FAT-1.0), $C_3N_{4.40}H_{2.0}O_{0.25}$ (FAT-1.5) and $C_3N_{4.33}H_{2.0}O_{0.26}$ (FAT-2.0) (summarised in the Table 4). As the formic acid amount increases in the precursors, the polymers show decreasing nitrogen with increasing oxygen amount, indicating more O species exist in the polymers' bulk structure. Unlike some recently reported copolymerisation polymers with slightly different features from g-C_3N_4, the FAT samples exhibit distinct and stepwise changes.

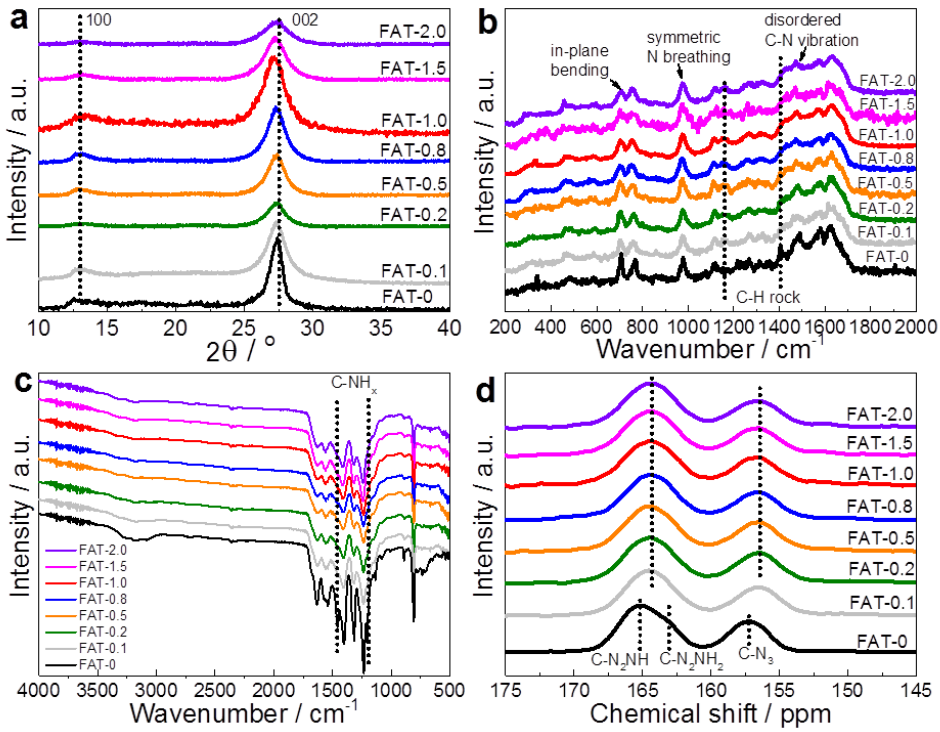

Figure 26. (a) X-ray diffraction patterns (b) Raman spectra (c) FT-IR spectra (d) ^{13}C solid-state nuclear magnetic resonance (ssNMR) spectra of different FAT samples.

Powder X-ray diffraction (PXRD) patterns of the samples were measured (Figure 26. a) to obtain the crystallinity information of FAT polymers. At the first glance, the patterns of the FAT samples are similar to FAT-0 (g-C_3N_4) in shape, which has two peaks locating at 13.0° and 27.4° assigned to the (100) and (002) planes, respectively, corresponding to intralayer packing size of 6.82Å and an interlayer distance of 3.26 Å.[68] A close examination shows that the (100) peak of the other FAT samples becomes weaker and slightly right shifts to 13.4°, indicating a reduced intralayer crystallinity and a closer crystalline

distance of 6.67 Å probably due to small polymer size and the shorten bond lengths in the presence of oxygen.[201] It is more evident that (002) peaks shift left, suggesting an enlarged layer-to-layer distance up to 3.30 Å due to a variation in structure, such as distortions in the FAT samples or the oxygen species between layers.[67] The width of the (002) peak becomes broadened as the formic acid amount increases, which also suggests that the crystallinity size of the polymers is smaller than FAT-0 (g-C_3N_4). The shifts of peak positions are consistent with the change in the formic acid equivalent, suggesting the higher number of O-containing groups, the larger shift of peak positions. Both the highest peak density and largest shift distance is found on the sample FAT-1.0.

Further increasing formic acid concentration causes the peak shift to become small. One can see formic acid in the precursor first results in a decline of polymerisation degree (Figure 26.a, FAT-0.1). As its amount further increases, relatively well-crystallised product gradually forms because the XRD patterns are getting sharper from FAT-0.2 to FAT-1.0. After that, the extra formic acid in the precursor leads to poor polymerisation again. Therefore, FAT-1.0 and FAT-0 (g-C_3N_4) could be two relatively highly-crystallised polymers.

Raman spectroscopies were used to detect the backbone of the FAT polymers (Figure 26.b). From the spectra, the heptazine based structure could be confirmed as most of these characteristic peaks appear at the same positions. The peaks in the 1200-1700 cm^{-1}, 980 cm^{-1} and 690 cm^{-1} regions represent the disordered graphitic carbon-nitrogen vibrations, the symmetric N-breathing mode of heptazine and the in-plane bending, respectively.[202-203] Notably, the peak at 1406 cm^{-1} in FAT-0 (g-C_3N_4) becomes negligible while the one at 1170 cm^{-1} emerges as the formic acid amount goes up. These two modes are both in-pane C-H rock and semicircle stretching but in different directions.[203] Such a change towards disordered structure could be assigned to the oxygen-linked chains. Similar to the intensity trend of XRD patterns, the intensity of signals from FAT-0 to FAT-1.0 and FAT-2.0 show a volcano curve. As discussed above, this is resultant from the differences in the degree of crystallinity induced by oxygen amount.

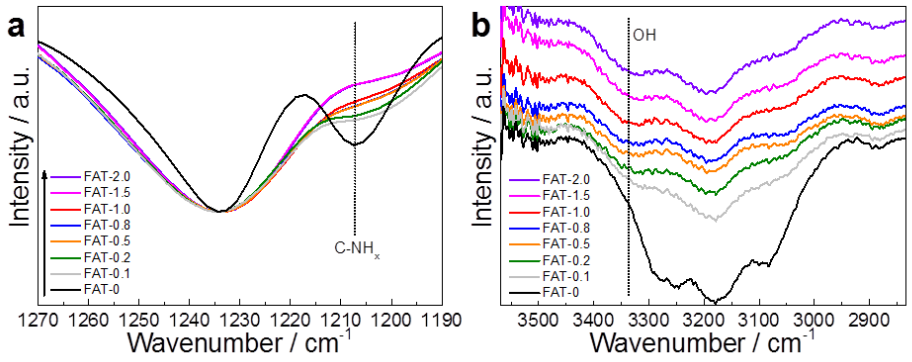

Figure 27. Zoomed-in FT-IR spectra of regions (a) 3500-2900 cm^{-1} and (b) 1270-1190 cm^{-1}

FT-IR spectra of FAT polymers were also compared to confirm the difference in structure. Generally, FAT samples have similar but broadened and less sharp peaks, owing to the incorporation of oxygen species into the structure (Figure 26.c).[67] As no peaks show up in around 2200 cm^{-1} and 1700 cm^{-1} region, the existence of C=O from formic acid and cyano groups from DCDA has been ruled out, indicating these precursors were converted during polymerisation.[204] As the formic acid amount increases, peaks of all other FAT samples at 1207 and 1455 cm^{-1} (indicated by dotted line in Figure 26.c) related to C-NH_x are gradually getting weaker than those of FAT-0 (g-C_3N_4) (Figure 27.a),[182] while identical peaks of NH_x around 3000-3300 cm^{-1} in other FAT samples decline and an additional peak assigned to –OH emerges at 3340 cm-

1 (Figure 27.b), altogether verifying the decline of NH_x groups and the formation of -OH species.[67]

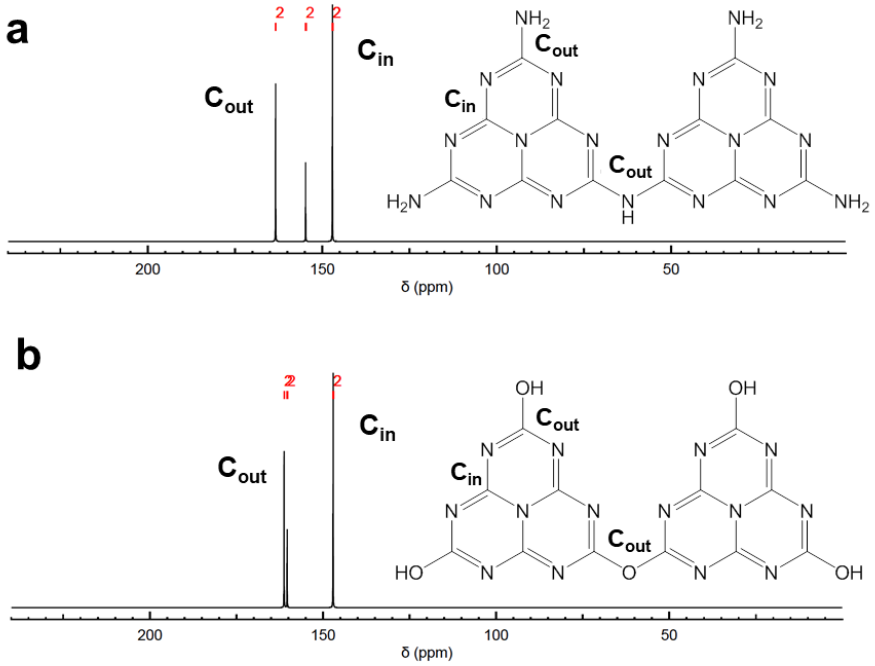

Figure 28. Modelled NMR carbon spectra of N-linked and O-linked heptazine. According to the structure and the predicted NMR spectrum, there are three types of carbon environments in N-linked heptazine (a. FAT-0, g-C_3N_4): C_{in}-N_3, N_2-C_{out}-NH_2, N_2-C_{out}-NH. While in O-linked heptazine (b. FAT-1.0) sample, there are also three types of carbon environments: C_{in}-N_3, N_2-C_{out}-OH, N_2-C_{out}-O. The C_e peaks of O-linked heptazine (FAT-1.0) merged into one signal and located between the ones of N-linked heptazine, which is consistent with the signal observed in the experimental ssNMR spectrum.

^{13}C ssNMR was used to illustrate such a structural change in detail (Figure 26.d). The characteristic peaks of FAT-0 (g-C_3N_4) around 166, 163 and 157 ppm are assigned to external circle carbons (C_{out}: CN_2NH and CN_2NH_2) and inner circle carbons (C_{in}: CN_3), respectively (Figure 26.d and 28).[39, 199] The overall NMR chemical shift suggests FAT polymers consist of a mixture of N linked heptazine (melem) and O linked heptazine. The observed right-shifted peaks in FAT samples by about 1 ppm with weakening NH_x related signals are resultant from the substitution of N linkers by oxygen bridges and terminals, which also

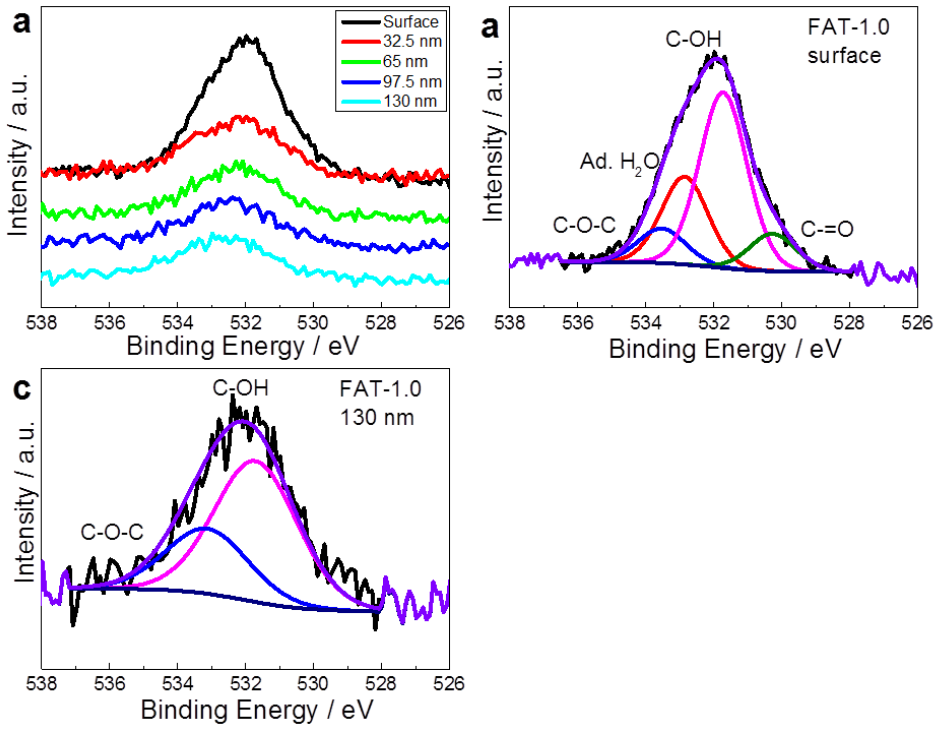

Figure 29. O 1s XPS spectra of etched FAT-1.0 samples of (a) different depths and de-convoluted analysis of (b) surface and (c) 130 nm depth of XPS spectra.[3-7]

matches the trend obtained from the NMR prediction software (Figure 28).[205-207]

Table 5. Compositions of C 1s XPS spectra for samples used in this study

Sample	C=O (289 eV) / %	C-N (287.5 eV) / %	C-O (286.2 eV) / %	C-C (284.6 eV) / %	C-O/C-N / %
FAT-0	2.47	63.13	3.59	30.81	0.057
FAT-0.1	10.62	58.43	4.96	25.99	0.085
FAT-0.2	7.81	68.62	6.46	17.11	0.094
FAT-0.5	6.23	68.18	6.99	18.6	0.103
FAT-0.8	2.54	74.53	8.74	14.2	0.117
FAT-1.0	4.62	54.52	6.8	34.06	0.125
FAT-1.5	3.94	60.88	8.67	26.51	0.142
FAT-2.0	1.62	74.51	10.8	13.07	0.145

X-ray photoelectron spectroscopy (XPS) was also undertaken to investigate the chemical states in these materials (FAT-1.0 as one example as shown in Figure 29 and 30). According to the depth profile of O 1s XPS spectra, the spectra peak shifts from 531.8 eV to 533.2 eV as the etching goes deeper from 0 nm to 130 nm (Figure 29 a). As observed, there are four types of O species on the surface of FAT-1.0 , which are surface oxides C=O (530 eV)[3], C-OH bond (531.5 eV)[4], adsorbed water (532.5 eV)[6, 208] and C-O-C bond (533.2 eV) (Figure 33 b).[5] After etching to 130 nm, only two obvious peaks of C-OH and C-O-C are detected (Figure 29 c), confirming the existence of oxygen

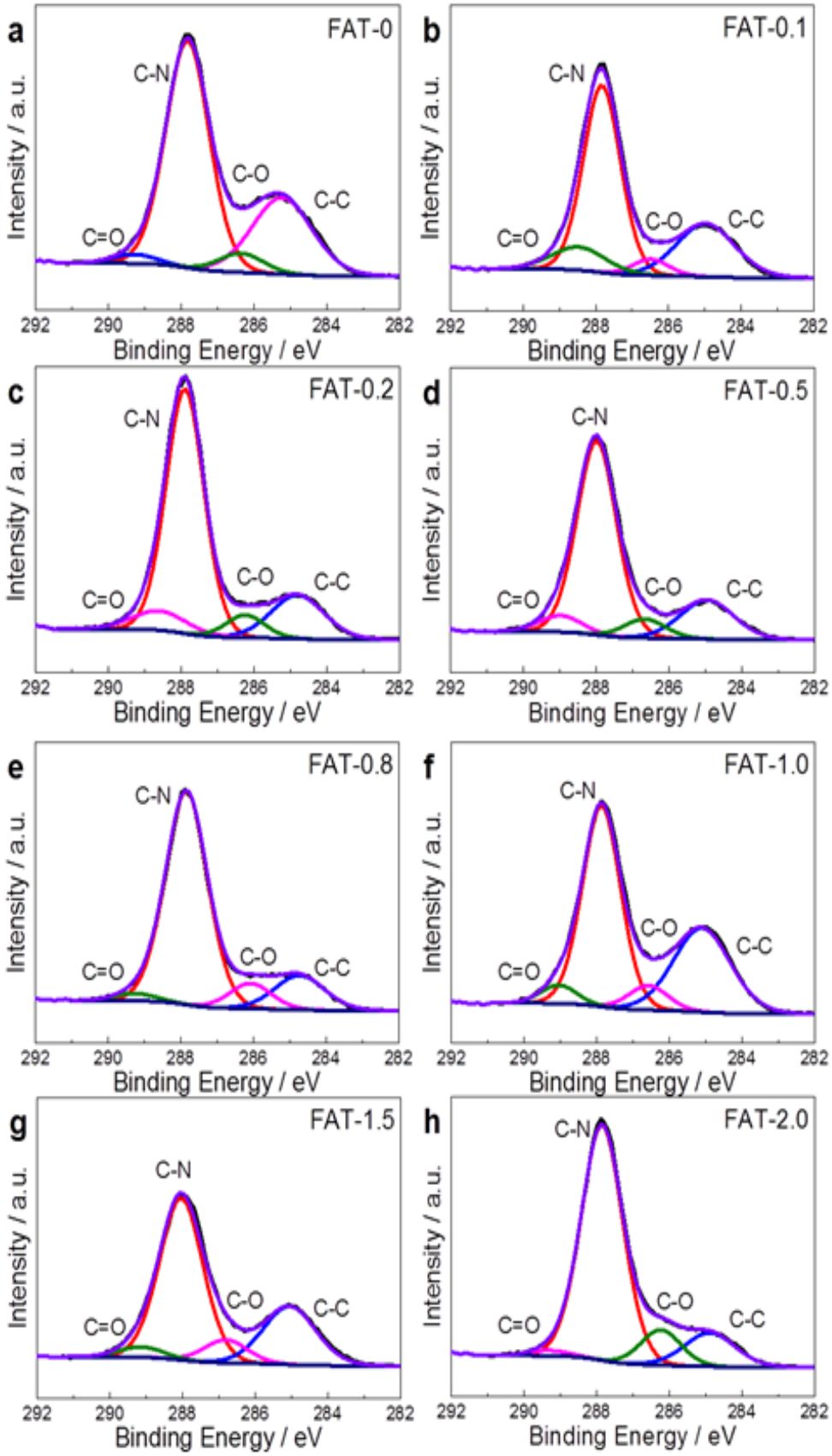

Figure 30. C 1s XPS spectra for samples used in this study: (a)-(h): FAT-0 to FAT-2.0.

during the etching is assigned to the decline of surface species (C=O, some C-O and water). According to C1s XPS spectra, the ratio of compositions of C-O to C-N (C-O/C-N) keeps going up with an increasing amount of formic acid (Table 5, Figure 30), indicating a decreased amount of N and an increased amount of O species in these polymers.[67] These results confirm oxygen linker (and OH terminals) in the structure, which should affect the properties of FAT polymers.

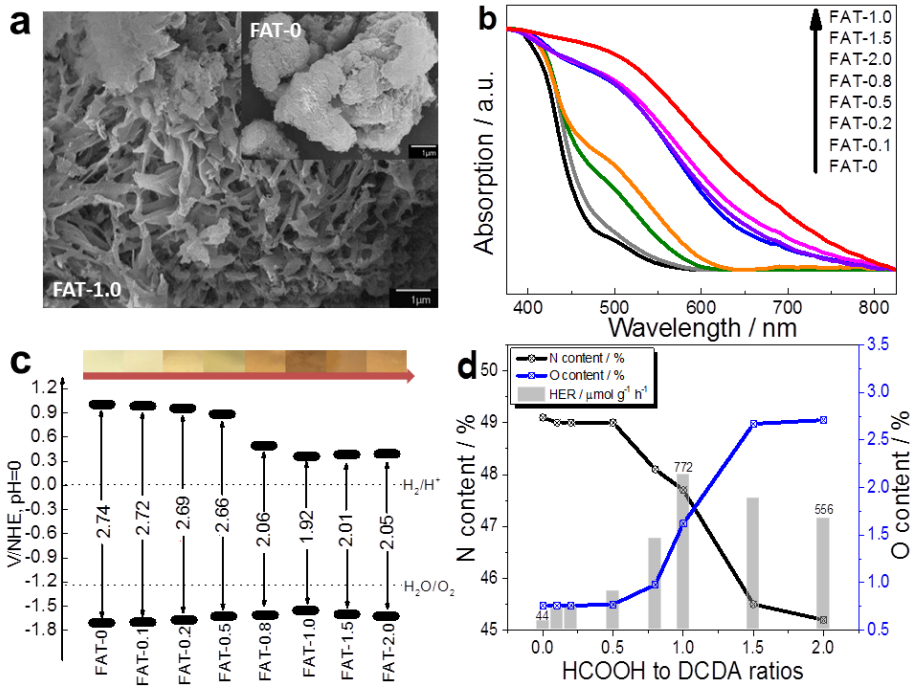

Figure 31. (a) SEM images of the FAT-1.0 and FAT-0 (g-C_3N_4) (inset) (b) UV-vis spectra (c) band alignment (V/NHE, pH = 0) (top: color photos) of FAT samples and (d) N contents, O contents and hydrogen evolution rates (HER) under visible light irradiation (420 nm < λ < 710 nm) of FAT samples.

Comparing the scanning electron microscopy (SEM) images between FAT-0 (g-C_3N_4) and FAT-1.0 (Figure 31 a), it is observed that the former has a layered stacking structure while the latter shows a ribbon-like structure.[50] Such structure is consistent with the less crystallised structure inferred from XRD patterns and Raman spectra. The hierarchical network/ribbon-like the structure of FAT-1.0 samples is also different from the previously reported polymer due to a new synthetic protocol.[67] The distortions in FAT samples allow more n-π* transitions from the edge N atom to the CB, which might also aid the visible photon absorption.[61] The fibre-like structure of FAT-1.0, instead of the packing plane-like FAT-0, should possess a higher surface area and a better contact with water.[64] Brunauer–Emmett–Teller (BET) surface area measurements were carried out to investigate the influence of surface area (Table 4). Consistent with the differences in SEM images, the surface area continuously increases from 5.5 m^2g^{-1} to 40 m^2g^{-1} from FAT-0 to FAT-2.0 samples, probably due to the releasing of oxygen-containing species during the polymerisation of oxygen precursors, similar to the thermal exfoliation of graphene oxide.[209-211] Therefore, the characterisations of PXRD, Raman, SEM, FT-IR NMR and XPS have altogether confirmed the proposed framework of FAT

polymers composed of distorted oxygen and nitrogen co-linked heptazine units.

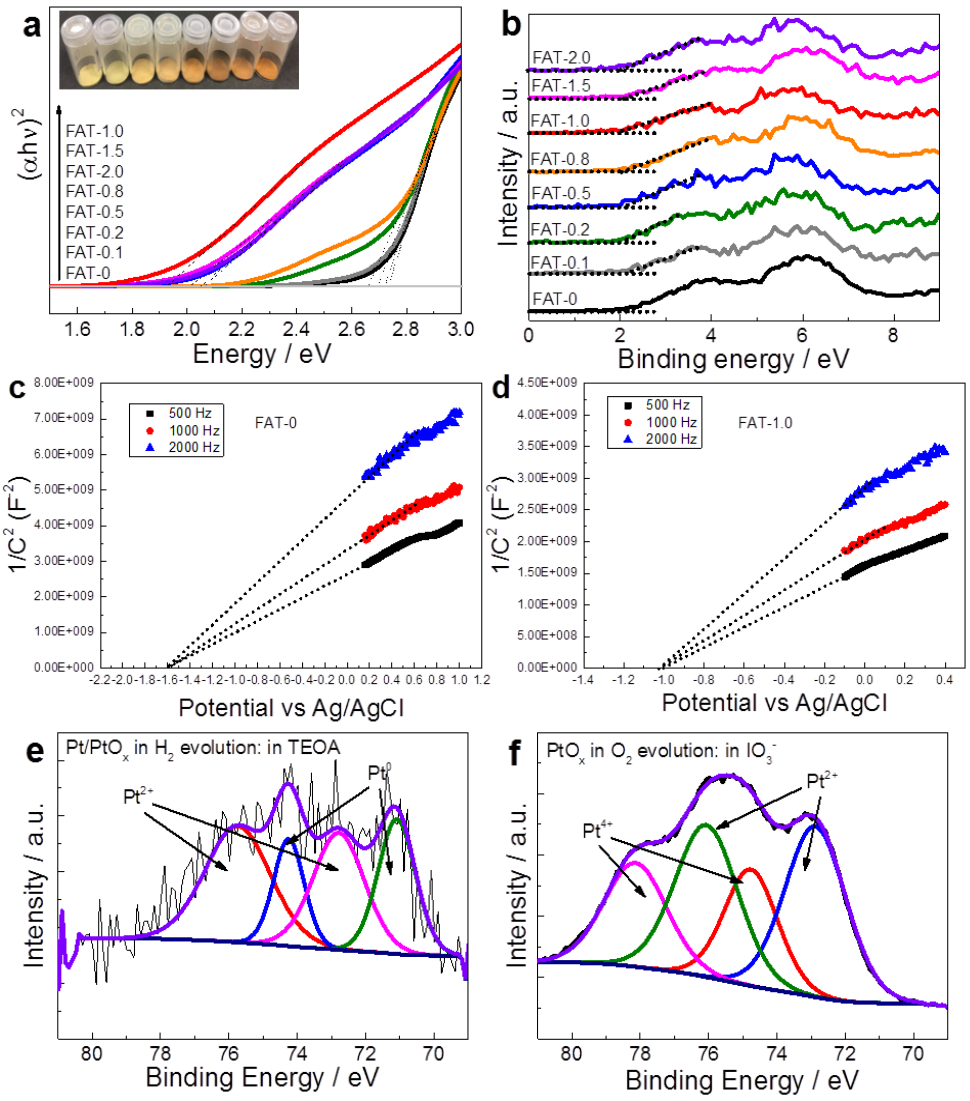

Figure 32. (a) Tauc plot with photographs (inset) and (b) valence band XPS spectra of FAT samples. Mott-Schottky plots of (c) FAT-0 and (d) FAT-1.0 at 2k, 1k and 0.5 k Hz frequencies. (e) Pt 4f XPS spectra of Pt-FAT-1.0 for H_2 evolution and (f) PtO_x-FAT-1.0 for O_2 evolution. The species of Pt in H_2 evolution are Pt metal and Pt^{2+} while the species of Pt in O_2 evolution are Pt^{2+} and Pt^{4+}.[8]

An apparent visual difference among FAT-0 (g-C_3N_4) to FAT-1.0 samples is the colour changes step-by-step from pale yellow to dark brown (Figure 31.b and photos in Figure 32.a). As mentioned above, the band gap engineering of photocatalysts could directly influence the harvest of visible photons, the driving force as well as the charge transfer behaviour. The band gaps of FAT samples were determined as by Tauc plot calculated from UV-vis spectra (Figure 31.b and Figure 32.a). Such stepwise band gap change from 2.7 eV (FAT-0) to final 1.9 eV (FAT-1.0) is clearly due to increased oxygen amount in the polymers (Table 4, Figure 31.c). A gap between the absorption curves of FAT-0.5 and FAT-0.8 divides the samples into two groups. Further increasing the acid amount in the precursor doesn't result in the narrower band gap. In contrary, the band gaps of FAT-1.5 and 2.0 are slightly wider than FAT-1.0, which might be due to the excess amount of introduced O atoms which could fragment the structure.

XPS valence band spectra (Figure 32.b), Mott-Schottky plots (Figure 32.c and d) along with Tauc plot (Figure 32.a) were used to determine the band alignment as shown in Figure 31.c. With the VB of FAT samples slightly changing, the narrow band gaps of FAT samples

mainly result from the downshift of CB. From FAT-0 to FAT-0.5, the CB position only moves moderately. From FAT-0.8 to FAT-2.0, the CB moves downwards (more positive) but still stays sufficient to drive proton reduction, attributed to the cooperation of O-linked chains. While O-linked chains create defects and distortions in the low concentration polymers (FAT-0 to FAT-0.5) which allows n-π* transition, the CB shift is more distinct in samples with more O-linked chains (FAT-0.8 to FAT-2.0).

5.3.2 H_2 and O_2 production

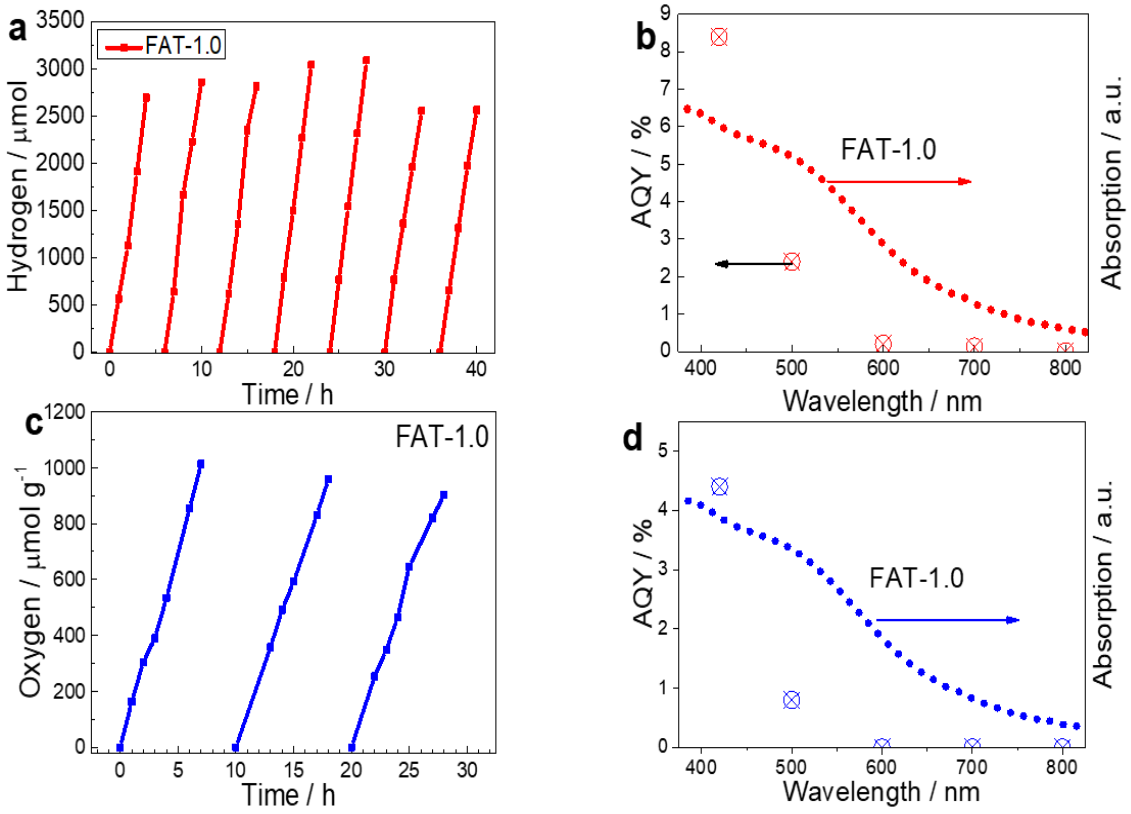

Figure 33. (a) Hydrogen evolution rates (HER) stability tests (420 nm < λ < 710 nm) for 30 hours and (b) apparent quantum yield (AQY) measurements of H_2 at different wavelengths on Pt-FAT-1.0 samples in presence of 10% TEOA as hole scavenger. (c) Oxygen evolution rates (OER) stability tests (420 nm < λ < 710 nm) for 25 hours and (d) apparent quantum yield (AQY) measurements of O_2 at different wavelengths on PtO_x-FAT-1.0 samples in presence of 5mM $NaIO_3$ as electron scavenger.

After successful synthesis of bandgap tuneable FAT polymers and illustration of their framework and electronic structures, the photocatalytic capabilities of FAT samples were fully evaluated. The H_2 evolution rates (HERs) were measured in the presence of 3 w.t. % Pt co-

catalyst (Figure 32 e) and 10% TEOA solution under 1 bar pressure and the visible irradiation (420 nm < λ < 710 nm) of 300 W light source (Newport-66485-300XF-R1, *ca.* 100 mW/cm^2). No activity was detected in the absence of light, photocatalysts or electron donor. As the nitrogen amount declines and oxygen amount rises due to an increased amount of formic acid in precursors, the HERs show a volcano-like trend peaking at FAT-1.0 (Figure 31.d). From FAT-0 (g-C_3N_4) to FAT-1.0, the HER gains an 18-fold increase from 44 μmol▪g^{-1}▪h^{-1} to 772 μmol▪g^{-1}▪h^{-1} and then decreases from FAT-1.0 to FAT-2.0. Such dramatically enhanced performance on FAT-1.0 is believed to be related to the narrowest band gap which utilises maximum visible photons, and the HER trend supports such relationship (Figure 31.c and 31.d). A further excess amount of formic acid probably shields the amine groups in precursors too much and results in the low degree of polymerisation (*e.g.* FAT-1.5 and FAT-2.0 samples), thus slightly decreasing the activity due to defects as a recombination centre. The HER of FAT-0 to FAT-0.5 only increases moderately but exhibits a sharper increment after FAT-0.8, indicating a good correlation between the bandgap and photocatalytic activity.[61] The synthesised FAT polymers also maintain a highly reproducible activity during the thirty-hour run (or seven cycles,

Figure 33.a), proving the incorporation of O at the linker/terminal positions instead of into heptazine units doesn't affect the stability. The apparent quantum yield (AQY) of hydrogen production measured on the optimum FAT-1.0 sample was determined to be 8.6 % at 420 nm and 2.5 % at 500 nm and it also shows small activity at 600 nm and 700 nm (Figure 33), following the same profile of the UV-Vis absorption spectrum and indicating a light-driven reaction (Figure 33.b). As FAT-0 doesn't work beyond 460 nm, the superior activity of FAT-1.0 in the visible region is again attributed to the narrowed band gap.

As N-linked heptazine polymers (FAT-0 or g-C_3N_4) have also been reported to achieve water oxidation although its activity is very moderate[22], I also examined whether the highly active FAT samples would show an enhanced performance of the water oxidation reaction. Surprisingly, the PtO_x-FAT-1.0 exhibited OER of 145 μmol▪g^{-1}▪h^{-1}, which is 19 times higher than that of PtO_x-FAT-0 (7.5 μmol▪g^{-1}▪h^{-1}) (Figure 33.c) under 5 mM IO_3^- aqueous conditions (Figure 33.c and Figure 32.f) under ambient conditions and visible light irradiation (420 nm < λ < 710 nm). The electron acceptor used here is IO_3^- because the commonly used Ag^+ would shield the surface of a photocatalyst hence its activity

cannot be continuously tested.[212] In Figure 33.d, the long period stability also validates that the oxygen is produced from water. Moreover, the oxygen content contained in 20 mg FAT-1.0 is 14.4 μmol according to the elemental analysis (Table 4), while the total amount of oxygen produced during the three cycles reached 57.5 μmol (Figure 33.d) which is much more than 4 times of the oxygen amount contained in materials, thus clearly demonstrating the oxygen production is derived from water oxidation.[22] FAT-1.0 also displays a high apparent quantum yield (AQY) of 4.3 % and nearly 1.0 % at 420 and 500 nm for water oxidation (Figure 33.d), respectively, surpassing the previous OER on g-C_3N_4 (1.1% and 0 at 420 and 500 nm in 10 mM Ag^+).[212] The superior performance for both H_2 evolution and O_2 evolution on the band gap tuneable FAT samples makes them promising candidates for the construction of Z-scheme water splitting.

5.3.3. The origin of superior performance

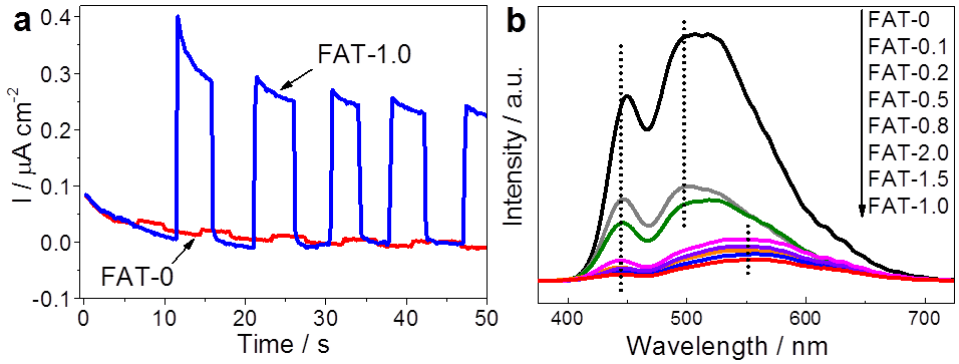

Figure 34. (a) Periodic on/off photocurrent response of FAT-0 and FAT-1.0 electrodes in 0.1 m Na_2SO_4 with 0.6 V bias versus Ag/AgCl. (b) Photoluminescence spectra (325 nm) of FAT samples.

To interpret the trend of enhanced activity as well as the structural change of FAT polymers, I refer to both experimental and theoretical approaches. Photoelectrochemical properties were investigated to compare the significant enhancement in photocatalytic performance on the FAT samples. As shown in Figure 34.a, the photocurrent performance on the FAT-1.0 sample and FAT-0 shows a nearly 26 fold difference, consistent with the measured HER.[67] Photoluminescence (PL) measurements were used to compare the charge separation capability on the FAT samples using a UV laser (325 nm, Figure 34.b). The peak near 420 nm is assigned to emissions from band edges involving π-conjugated states. The larger portion of recombination signals are the ones around 500-600 nm corresponding to the intra-

states including n-π* transition and defect-based states.[165, 213] From FAT-0 to FAT-2.0, PL peaks gradually decreases and the peak intensity trend reversely agrees with the HER on FAT polymers, indicating a stepwise enhanced charge separation was obtained on the doped samples. The optimum sample FAT-1.0 shows about two magnitudes lower intensity than FAT-0. Moreover, with the band edge peaks anchoring at 420 nm, the intra-state peaks move from 500 nm to 600 nm as the formic acid amount goes up, verifying the process of the band structure narrowing due to additional oxygen-linked chains.[213] Therefore, less radiative electron-hole recombination and extensive light harvest ability due to narrow band-states of FAT samples would altogether promote their photoactivity. Other factors might influence the performance to some extent, such as surface area (Table 4). However, FAT-1.0 (12.1 $m^2 g^{-1}$) instead of the samples with the larger surface area (FAT-1.5, 16.4 $m^2 g^{-1}$ and FAT-2.0, 40.0 $m^2 g^{-1}$), achieves the highest HER, so the enhancement in activity cannot be directly attributed to the surface area. It should be noted that the PL signals slightly rise again in samples from FAT-1.0 to FAT-2.0. Similarly, the trend of structural characterisations and gas evolution measurements

also peak at FAT-1.0 while more oxygen content doesn't contribute further to the enhancement.

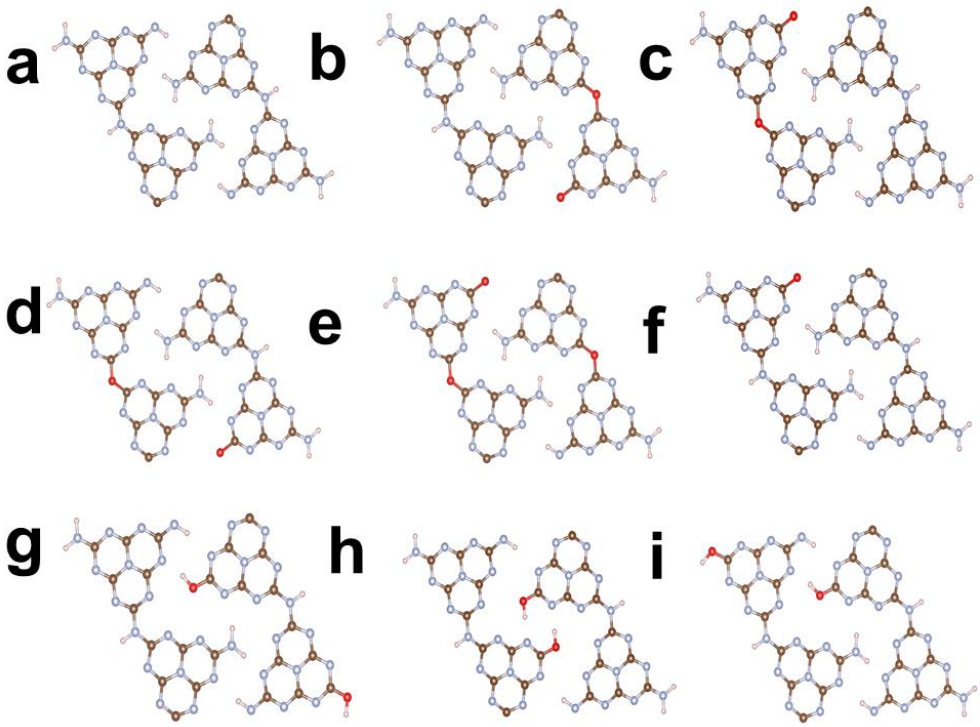

Figure 35. Oxygen arrangement configurations in the modelled polymers. All tested unit cells, except for the reference g-C_3N_4, have the same amount of oxygen: each consists of two of the layers above and has four oxygen atoms out of 140 in the unit cell (2.9%). O-linked chains (Conf 1-5) are composed of layers b-f, while O-terminated (Conf 6 – 9) chains are composed of layers a, g and f. The table below shows which models are used in each unit cell.

Table 6. Oxygen arrangement configurations in the modelled polymers

configuration	Layer #1	Layer #2	O-containing chains
g-C_3N_4	a	a	0%
1	b	b	50%
2	b	c	50%
3	b	d	75%
4	e	f	75%
5	d	d	100%
6	g	g	50%
7	h	h	100%
8	i	i	100%

Further explanation for this phenomenon comes from the results of computational work conducted on the system, which show a direct relationship between the incorporation of the oxygen within the framework and the electronic structure and hence the predicted performance of polymers. As previously showed, the oxygen content is incorporated in the framework outside the heptazine (tri-s-triazine) rings, replacing an –NH– group either by linking two rings or by terminating a chain (Figure 35, Table 6). The models, shown in detail in Figure 35, are composed of 4 linear chains organised in 2 layers, with a total of 8 tris-triazine rings. In g-C_3N_4, this configuration would correspond to 8 -NH_2 terminal groups and 8 -NH- linker groups in a

unit cell. To model the high oxygen content FAT polymers (FAT-0.8 and over), 4 of those groups are substituted with either -OH terminals or -O- linkers. This set up allowed us to investigate the different oxygen configurations that can be found locally within the polymer, which will be proved to have a major effect on the performances of the material.

Table 7. Summary of the structural and electronic properties of the computationally modelled systems. The structures related to each of the systems are shown in Figure S5. All structures with 50% or 75% of O-containing chains show a spatial separation between VB and CB, as shown in Figure 36 a, b and c.

Model name	Oxygen type	O-containing chains / %	Bandgap / eV	Formation energy / kJ/mol
g-C_3N_4	None	0%	1.01	+13.05
Conf. 1	-O- linker	50%	2.13	-8.83
Conf. 2	-O- linker	50%	2.11	-9.06
Conf. 3	-O- linker	75%	2.14	-9.01
Conf. 4	-O- linker	75%	2.13	-8.98
Conf. 5	-O- linker	100%	2.33	-9.05
Conf. 6	-OH terminal	50%	1.77	-9.96
Conf. 7	-OH terminal	100%	2.24	-10.43
Conf. 8	-OH terminal	100%	2.27	-10.33

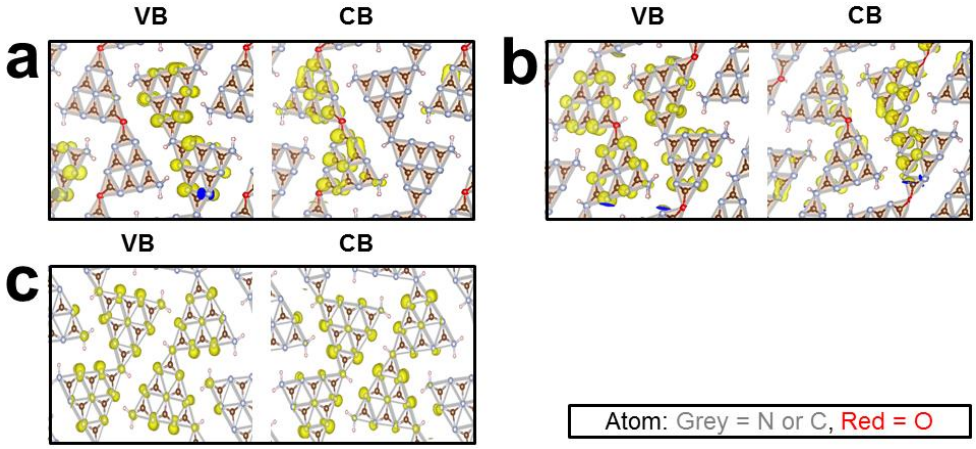

Figure 36. The highest occupied molecular orbitals (VB, left) and lowest unoccupied molecular orbitals (CB, right) (grey: N or C atoms, red: O atoms and yellow: orbitals) of (a) highly ordered structure with O linkers and N linkers separately placed in different chains and (b) disordered structure with O linkers and N linkers randomly placed in all chains. (c) shows the VB and CB of non-doped g-C_3N_4, showing no spatial separation.

The Density Functional Theory (DFT) calculations show how the substitution of –NH– groups is favourable, as the formation energy goes from +13.05 to -10.33 kJ/mol for the modelled O-linked polymers. The stability increases even further when oxygen is incorporated as -OH linkers (Table 7), but the electronic effect of the two substitutions appears to be similar. Density of State (DOS) calculations have also been performed. The calculated band gaps present a smaller than expected band gap for g-C_3N_4 (see the Computational Methodology section for more detail), although this underestimation of the bandgap is expected. Interestingly, the calculated gaps for the FAT samples compare reasonably with experiment, but given the known inadequacy

of PBE-DFT in calculating band gaps, no further use of calculated band gaps is made in my analysis. However, a subtle difference between the oxygen arrangements seems to drive the electronic structure, as shown by the decomposed charge density of the valence and conduction bands. According to the EA (Table 4) of FAT samples, the oxygen content increases and the nitrogen content declines as more formic acid is added in the precursor, corresponding to the gradual substitution of –NH– groups with oxygen in the polymer. The co-existence of N-containing chains and O-containing chains in the FAT polymers can drastically improve the charge separation due to the N-chains' electron donor nature and O-chains' electron acceptor nature: when the oxygen is distributed in a well-ordered fashion – at least locally – with adjacent N-containing and O-containing chains, the difference in electronic behaviour results in a spatial separation of the VB and CB, which appear to be located on the two chain types, respectively (Figure 36.a). Such spatial separation might arise from a change in the electrostatic potential of the O-containing cells due to the presence of polar covalent bonds, as shown in the previous literature,[214-215] although the modelling could not find solid evidence due to the complexity of the problem and the polymeric nature of the

system. However, this finding is in good agreement with the experiments, as it relates the increase in performance up to FAT-1.0 to an increase in charge separation, as photoexcited electrons are gathering on O-containing chains and holes on N-containing ones, therefore slowing down the charge recombination and improving the performances. However, little control can be achieved in how the oxygen is arranged, and a more uniform distribution of oxygen among the chains improve the charge separation only marginally concerning pristine g-C_3N_4 (Figure 36. b and c).

It is, therefore, reasonable to propose that the performance trend as the amount of formic acid in the precursor increases depends on the local distribution as well as on the amount of oxygen introduced in the g-C_3N_4 chains: while a reasonable amount of formic acid will benefit the performances of the polymer by reducing the band gap and, in some areas of the polymer, create a spatial separation between the VB and the CB that improves the e^--h^+ lifetime, a concentration of O-linkers and OH terminals that is too high would lower the probability of having this separation, leading to the decreased performances of FAT-1.5 and FAT-2.0. Therefore, a peak in performance is to be expected, as

the control of the arrangement of oxygen within the framework is very difficult.

5.4 Summary

In summary, a novel strategy has been successfully developed to synthesise band gap tuneable, highly efficient and robust organic semiconductor photocatalysts with an enlarged optical window and suppressed charge recombination, thus addressing the two major challenges in photocatalysis. By controlling the polymerisation process, the framework and electronic structure could be carefully tailored via incorporation of oxygen and nitrogen linkers as well as terminals between the heptazine units. When the ratio of formic acid to dicyandiamide increases, more oxygen linkers and OH terminals are incorporated into the heptazine-based polymers, increasing the interlayer distance and the distortion in the structure as well as narrowing the bandgap, consequently enhancing the photoredox activity. Moreover, the optimum FAT-1.0 sample exhibits 18 times higher H_2 evolution activity than reference g-C_3N_4 under visible light, resulting in high AQY of 8.3% and 2.5% at 420 nm and 500 nm.

Surprisingly, it achieves 19 folds enhancement in O_2 evolution, leading to an AQY of 4.3% and about 1.0 % at 420 nm and 500 nm. The excellent performance and band structure flexibility make the FAT polymers a group of promising semiconductors for potential applications including the construction of Z-scheme water splitting and photoelectrodes. Experimental and theoretical results have rationalised the observations regarding a narrowed bandgap and enhanced charge separation, which is due to the oxygen incorporation into the linker/terminal position and reasonably higher amount of oxygen, narrower bandgap, leading to higher activity. Further increasing the oxygen content will result in a bandgap increase. These findings pave a new approach to modifying the properties of polymers for efficient solar energy conversion through careful control of the polymerisation process.

6. Photocatalytic CO_2 conversion on CQD/polymer junctions

After the successful development of polymers for visible light-driven water splitting (including half reactions), I further applied this new group of polymers in a more challenging multi-electron photochemical process of CO_2 conversion. I first synthesised two kinds of carbon quantum dots (CQD) as cocatalysts. One was obtained through a novel microwave-assisted method (noted as CQD), and the other was a reference material fabricated through the sonication of glucose (noted as ^{red}CQD) as reported. Secondly, I coupled both co-catalysts with a widely reported DCDA-derived graphitic carbon nitride nanosheets (GCNN) to form the photocatalyst junctions. Then these junctions were evaluated in CO_2 conversion, and the charge transfer functions of two types of CQD were investigated by TAS. Then the properties of two junctions consisting of CQD coupled with the new polymer reported in Chapter 5 (FAT) were compared for further optimisation of efficient CO_2 conversion to methanol.

6.1 Introduction

Conversion of carbon dioxide to high-value chemicals not only provides a renewable energy source,[128-129, 216-220] but also mitigates climate change due to anthropogenic CO_2 emission. Nature employs very effective strategies to convert CO_2 to biomass by utilising catalysts composed of abundant and low-cost elements such as C, N and so on. It is highly desirable to drive CO_2 reduction by renewable and low-carbon energy sources, such as solar energy and low-cost catalysts to avoid additional CO_2 generation. The past few years have witnessed several benchmark materials reported for photocatalytic CO_2 conversion. The latest examples include CO_2 conversion to acetic acid by bacterial hybrid photocatalyst (Moorella thermoacetica, with cadmium sulfide nanoparticles)[128] and to methane by iron tetraphenylporphyrin complex functionalized with trimethylammonio groups with a molecular sensitiser.[129] These breakthroughs are exciting while the presence of an efficient hole scavenger (electron donor, *e.g.*, sulfite, TEOA) is crucial, which makes the developed system less sustainable and economically unfavourable. A preferable, yet more challenging process is to achieve a complete redox cycle by combining

photocatalytic CO_2 reduction by electrons with water oxidation by holes to generate renewable fuels, thus making the chemical process sustainable. While in most cases of reported CO_2 reduction, water oxidation to O_2 was hardly experimentally proved. Furthermore, such a process could be more economical than others (photoelectrocatalysis and PV-powered electrocatalysis) when carried out in a suspension system.

Among the major products of CO_2 reduction, *e.g.* CO, CH_4, formic acid or mixtures of these,[221-226] methanol is one of the most attractive as an easy-to-handle liquid fuel compatible with current infrastructure. On the other hand, water oxidation proceeds via a four-hole process,[96] and hence is kinetically slow. CO_2 conversion to methanol is a six-electron process[227] and consequently is even more challenging. Therefore, the key in the process is to achieve a sufficiently long lifetime of excitons, or both electrons and holes, through efficient charge separation. It is thermodynamically easier to oxidise methanol than water by photogenerated holes; thus conventionally methanol is produced via a two-step process from CO_2 (CO_2 to syngas and then methanol). A desirable one-step photocatalytic system should preserve

methanol production with a focus on high selectivity for water oxidation.

A nature-inspired catalytic system is highly desired which is composed of earth-abundant carbon and nitrogen and separates charges effectively and more importantly selectively oxidises water rather than methanol. Since the preliminary demonstration of CO_2 conversion to chemicals via photocatalysis by semiconductors in the 1970s, considerable efforts have been devoted to developing efficient photocatalysts.[228] Among those, polymeric graphitic carbon nitride (GCN), a layered polymer[223, 229-230] composed of heptazine units with a visible-light-responsive bandgap and appropriate band edge positions, has demonstrated promising photocatalytic activity for water splitting as well as CO_2 capture and photoreduction,[38, 60, 99, 231-232] while not efficiently for methanol production from CO_2. Considering the rapid recombination of exciton pairs due to the charge-localised nature of GCN,[38, 165] it is necessary to seek for selective charge acceptors to improve the electron-hole separation and prolong their lifetime in GCN photocatalysts and to enable the use of abundant water as the electron donor. Carbon quantum dots (CQD), an emerging class of carbon

nanomaterials (< 10 nm in diameter) with reported excellent properties in photoinduced electron transfer reactions, have recently been used to enhance visible light absorption of photocatalysts and more importantly as an electron acceptor for reduction reaction.[99, 113, 149, 233-234] Although the exciting function of CQD for enhanced reduction reaction has been demonstrated in the majority of publications,[235-240] CQD as a hole acceptor for water oxidation process has seldom been reported and proved experimentally, while it is the key for sustaining highly selective methanol production during CO_2 conversion.

In Chapter 4 and 5, the electronic structure of organic photocatalysts could be facilely controlled by selective doping into linker positions, thus developing new groups of metal-free candidates for junction construction.[67, 210] Based on previous findings, for the first time, this chapter demonstrates a scalable junction system based on pure organic semiconductors for artificial photosynthesis from CO_2 and water. When carbon quantum dots is paired with oxygen and nitrogen co-linked heptazine polymer (FAT polymer) or GCNN under visible irradiation (420 nm < λ < 710 nm), CO_2 with water could be selectively

converted to methanol and O_2 in a stoichiometric ratio of 2:3. The reason behind this novel properties is investigated and discussed later.

6.2 Methodology

6.2.1 Synthesis techniques

Materials

All chemical reagents were analytical grade and were used without further purification. Citric acid, N, N-Dimethylformamide (DMF), urea, DCDA (Dicyandiamide), methanol, dichloromethane were purchased from Sigma-Aldrich Company Ltd. Deionised water used in all the experiments has a resistivity of 18.1 MΩ·cm.

Synthesis of pure g-C_3N_4 Nanosheets (GCNN)

2 g DCDA in a closed crucible was heated at 500 ^oC for 4 h in static air with a ramp rate of 5 ^oC /min. The yellow solid agglomerates were milled into powders using an agate mortar. 0.5 g of this as prepared powders was placed on a ceramic plate and heated at 500 ^oC for 4 h in the air with a ramp rate of 10 ^oC /min.[50] Then, the g-C_3N_4 nanosheets with light yellow colour were finally obtained. This g-C_3N_4 nanosheets sample was named as GCNN.

Synthesis of microwave-assisted carbon quantum dots (noted as CQD)[241]

Citric acid (3 g, 15.6 mmol) and urea (1 g, 16.7 mmol) were added into 8 ml deionised water and vigorously stirred to form a transparent solution. This solution was then heated in the microwave oven for 200 seconds under 300 W power beaker model. During the reaction, the solution was changed from a colourless liquid to a dark brown porous solid, which indicated the CQD were finally produced.[241] The solid product was then put into the oven and dried at 80 ^{o}C for 10 h to remove the residual molecules. The suspension of the crude CQD was purified in a centrifuge at 8000 r/min for 1 h to remove large or agglomerated particles. The final brown aqueous solution was eluted with a mixture of methanol and dichloromethane at ratios of 1:2 and 1:1 (v/v) to obtain CQD. At last, the resulting CQD was dried into solid powders.

Synthesis of CQD/GCNN nanocomposite

2 g of DCDA and x mg of carbon quantum dots obtained above (x = 30, 50, 70 and 90, equal to w.t. 1.5%, 2.5%, 3.5% and 4.5% to DCDA precursor) were added to 10 mL of DMF and stirred for 1 h, then the liquid was dried at 60 ^{o}C for 10 h to evaporate DMF completely. The

resulting mixture was placed into a crucible with a cover and annealed at 500 ^{o}C in the air for 4 h with a ramping rate of 5 ^{o}C /min. The brown solid was washed with DI water and dried at 80 ^{o}C, then milled into powders with an agate mortar. 0.5 g of powders was placed on a ceramic plate and heated at 500 ^{o}C for 4 h in the air with a ramp rate of 10 ^{o}C /min. Finally, the CQD/GCNN nanocomposite was obtained. The samples were denoted as CQD(n)/GCNN (n = 1.5, 2.5, 3.5 and 4.5) by the percentage of carbon dots density in the precursor.

Synthesis of reduction function CQD (^{red}CQD) [240]

The ^{red}CQD was reported before and synthesised via a modified method as reported. ^{Red}CQD was fabricated by the alkali-assisted ultrasonication treatment of glucose. Firstly, 18 g of glucose was dissolved in 100 mL of deionised water and mixed with a 1.0 M NaOH solution prepared by dissolving 4 g of NaOH in 100 mL of deionised water. The mixture was ultrasonicated for 2 h, resulting in a dark brown solution. The crude solution was neutralised (pH 7) using 0.1 M HCl. A brown solution was obtained, implying the successful production of CNDs. The ^{red}CQD solution was dried to obtain a solid ^{red}CQD sample.

Synthesis of ^{red}CQD/GCNN nanocomposite

The junction was synthesised via a modified method as reported.[240] 1 g of pure DCDA-derived g-C_3N_4 was dispersed in 200 mL of 0.5 M HCl and ultrasonicated for one h to simultaneously remove any unpolymerised molecules and protonate the surface of the g-C_3N_4. The mixture was then continuously stirred for 4 h at room temperature. This was followed by centrifugation and repeated washings with deionised water to remove excess HCl. Lastly, the protonated g-C_3N_4 (GCNN) was dried in an oven overnight at 70 ° C and then ground into powder. 1g GCNN and 0.03g ^{red}CQD were then subjected to hydrothermal treatment in a Teflon-sealed autoclave with stirring at 120 ° C for 4 h. Once cooled to room temperature, the suspension was centrifuged at 9,000 rpm. The solid sample was collected and washed several times with deionised water, then dried at 70 ° C for 12 h, noted as ^{red}CQD/GCNN.

Synthesis of CQD/FAT nanocomposite

The FAT polymer was synthesis from formic acid (897 µL, 23.8 mmol) and DCDA (2 g, 23.8 mmol) dissolved in 40 mL DI water. The solution was kept at 130 ^{o}C for 6 h before drying and calcination in a lidded crucible by a muffle furnace (ramp rate: 2 ^{o}C/ min, 500 ^{o}C for 4 h). CQD /FAT was synthesised from CQD (100-300 mg 5-15% w.t.) and

FAT (2 g) suspended in 10 mL DMF. After drying at 60 ^{o}C for 10 h, the sample was annealed in the same furnace on a ceramic plate (ramp rate: 10 ^{o}C/ min, 500 ^{o}C for 4 h), together with pure FAT and GCN (to keep consistency). Reference samples involving GCN were synthesised from DCDA using the same parameters.[157] DI water, 0.1 M NaOH and HCl were used to wash the produced powders adequately.

6.2.2 Photocatalytic analysis

Before the photocatalytic reduction of CO_2, 10 mg photocatalyst and 10 mL water were added into a septum-sealed borosilicate glass reactor with a volume of 140 mL. Then, the reactor was purged with CO_2 for the photoreduction experiment. A 300 W Xe lamp (Newport) was utilised as a light source, and the light output power was measured by a Newport 918-D calibrated photodetector. During the reaction, the products were analysed by GC (Varian GC-450) with a thermal conductivity detector (TCD, connected to a molecular sieve column) and a flame ionisation detector (FID, connected to a CP-SIL 5CB capillary column) containing a methaniser equipment. Ar gas was used as the GC carrier gas.

For the isotope-trace experiment, the same photocatalytic process was applied except $^{13}CO_2$ (^{13}C 99%, Sigma-Aldrich) was used as the feed gas. The products containing C-isotope were analysed by GC–MS (Shimadzu QP-2010SE) with a molecular sieve 5 Å capillary column (for CO) or a Rxi-624Sil MS capillary column (for methanol). Helium gas was used as a carrier gas during the measurement.

6.2.3 Computational details.

All the calculations were carried out by Dr. Xiaoyu Han using Vienna ab-initio Simulation Package (VASP). The projected augmented wave (PAW) potentials were adopted to treat the core electrons, and electron exchange and correlation were treated using by PBE functional. The energy cutoff was set to 500 eV. All the atoms were fully relaxed until the total energies were converged up to 10-5 eV and the Hellmann-Feynman forces were less than 0.01 eV /Å. Only Gamma point was using for the k-point sampling. For the gas phase adsorption of CO2 and CH3OH, a DFT-D2 method of Grimme was adopted for the van der Waals correction. Spin polarisations were considered in the whole calculations. According to the Figure 38, 10 different adsorption configurations were considered. They included along or perpendicular

to the A or B hydrogen bonds denoted as A/B_o, A/B_c, respectively. There are also the bonding sites like along the A or B hydrogen bonds but perpendicular with the CQD plane denoted as A/B_p. More configurations included those parallel or perpendicular with AB and BB′ directions. The adsorption energies results for different configurations were listed in Table 8. Overall, the hydrogen bonds play an essential role in the strength of the adsorption. For CO_2, both AB and BB′ sites are the top two stable sites, which involves forming two hydrogen bonds. Compared with CO_2, CH_3OH possesses stronger binding energy by a magnitude. Similarly, several adsorption sites for CO_2 and CH_3OH on protonated porous GCNN are also denoted in Table 9.

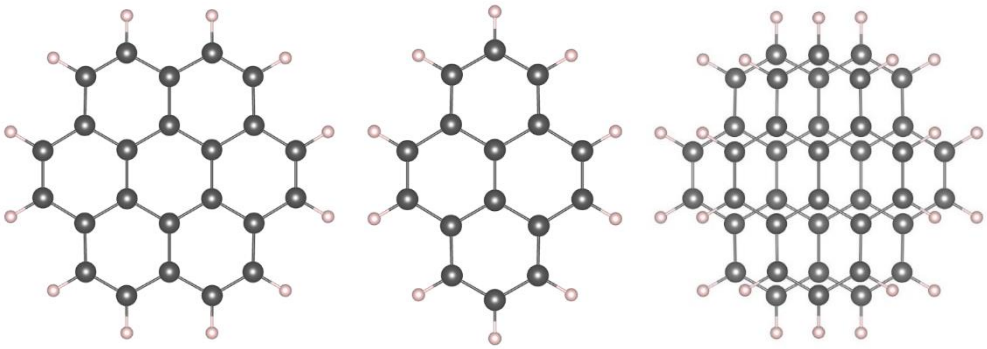

Figure 37. The CQD was adopted two carbon nanoflakes, coronene (left) and pyrene (middle), symmetrically stacking together. The grey and pink balls represent carbon and hydrogen atoms, respectively. Right: the top view of the CQD structure. It consists of a coronene at the bottom and a pyrene on top.

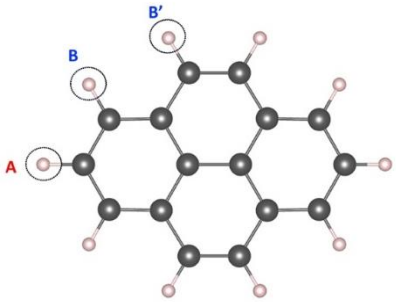

Figure 38. The denotations of the different adsorption sites for CO_2 and CH_3OH by the positions of the H atoms on CQD.

Table 8. The adsorption energies, E_{ad} (in eV), of CO_2, CH_3OH and H_2O on CQD with different configurations.

Configurations	CO_2	CH_3OH	H_2O
A_o	-4.98E-02	-1.04E-01	-1.03E-01
A_c	-7.08E-02	-1.28E-01	-1.01E-01
A_p	-7.28E-02	-1.28E-01	-8.34E-02
B_o	-6.14E-02	-9.07E-02	-1.08E-01
B_c	-9.89E-02	-1.16E-01	-1.12E-01
B_p	-7.79E-02	-2.76E-01	-8.89E-02
AB	-1.12E-01	-1.60E-01	-2.29E-01
AB_p	-8.73E-02	-2.89E-01	-2.30E-01
BB	-1.07E-01	-1.49E-01	-1.16E-01
BB_p	-9.61E-02	-1.34E-01	-2.10E-01

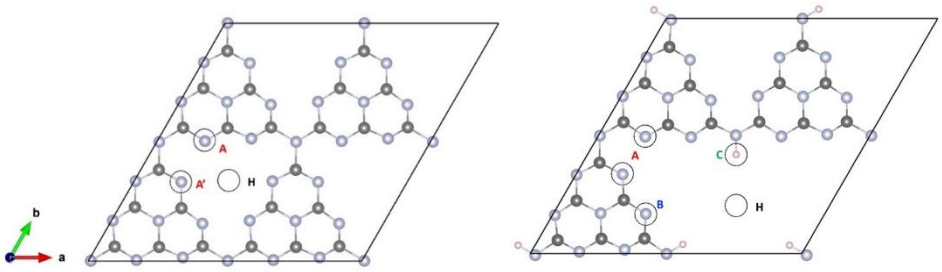

Figure 39. The denotations of distinct positions of protonated porous GCNN for CO_2, CH_3OH and H_2O adsorptions.

Table 9. The adsorption energies, Ead (in eV), of CO_2, CH_3OH and H_2O on protonated porous GCNN with different configurations.

Configurations	CO2	CH3OH	H2O
AA'	-2.80E-01	-3.43E+00	-6.55E-2
AA'_p	-2.23E-01	-4.03E-01	N/A

AB	-1.69E-01	N/A	-6.66E-2
B	-2.31E-01	-3.82E+00	N/A
B_p	-1.79E-01	3.64E+00	N/A
C	-1.83E-01	-3.96E+00	-8.94E-2
C_p	-2.14E-01	-3.91E+00	N/A
H_p	-1.84E-01	-5.26E-01	N/A

6.3 Results and discussion

6.3.1 CO_2 conversion on CQD/GCNN.

6.3.1.1 Characterisations CQD/GCNN

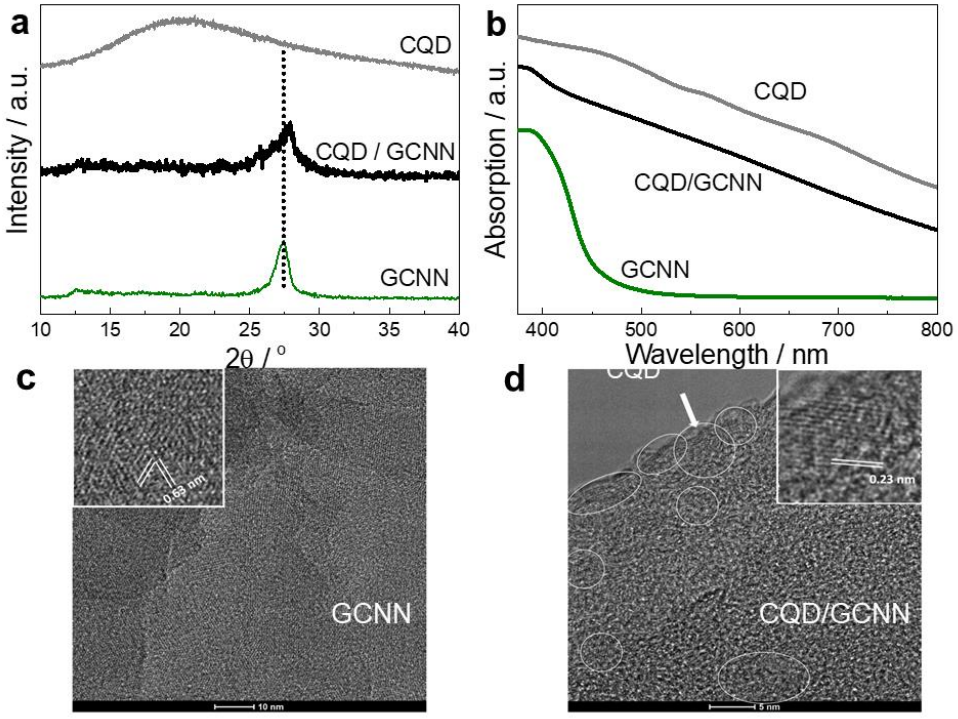

Figure 40. (A) XRD patterns of CQD, GCNN and CQD/GCNN nanocomposite; (B) UV-vis absorption spectra of GCNN and CQD/GCNN. (C) HRTEM image of GCNN. The inset is an enlarged image showing (110) crystal fringes of GCNN. (D) HRTEM image of CQD/GCNN nanocomposite. Some CQD are marked by circles. The inset is an enlarged image of one CQD indicated by the arrow, showing (110) fringes of a 2 x 2 x 1 graphite superstructure.

Firstly, the CQD were synthesised via a modified three-minute microwave-assisted method, much faster than the reported method for high-quality CQD. [15, 20, 24] Then dicyandiamide (DCDA) and purified

CQD were dissolved in DMF (10 mL, stirred for 1 h) and the slurry was stirred for 10 h at 60 °C. The solid was then transferred into a ceramic crucible and heated at 500 °C for 4 h in air, and a thermal exfoliation process was carried out on CQD/GCNN to form the nanosheets. For comparison, GCNN were synthesised from a DCDA precursor followed by thermal oxidation etching as reported earlier.[32] Detailed CQD and nanocomposite photocatalyst preparation procedures are listed in the 6.2.1 Synthetic techniques. According to X-ray diffraction (XRD) patterns (Figure 40.a), CQD shows a broadened (002) band around 20° (d-spacing of 4.43 Å) compared to graphene in the literature (26.5°, 3.36 Å), indicating an enlarged interlayer distance due to a disordered stacking manner which is commonly observed during N doping.[242-243]

The synthesised polymer GCNN exhibits the typical diffraction signals of (002) and (100) at 27.4° (3.26 Å), 13.0° (6.82 Å), respectively.[67]

The co-existence and details of the structures of both CQD and GCNN were further examined by transmission electron microscopy (TEM) (Figure 40. c and d. Figure 41). The as-prepared 2D GCNN is graphene-like, with several micrometres in diameter. The surface of the ultrathin nanosheets is very rough with a crinkly structure caused by the

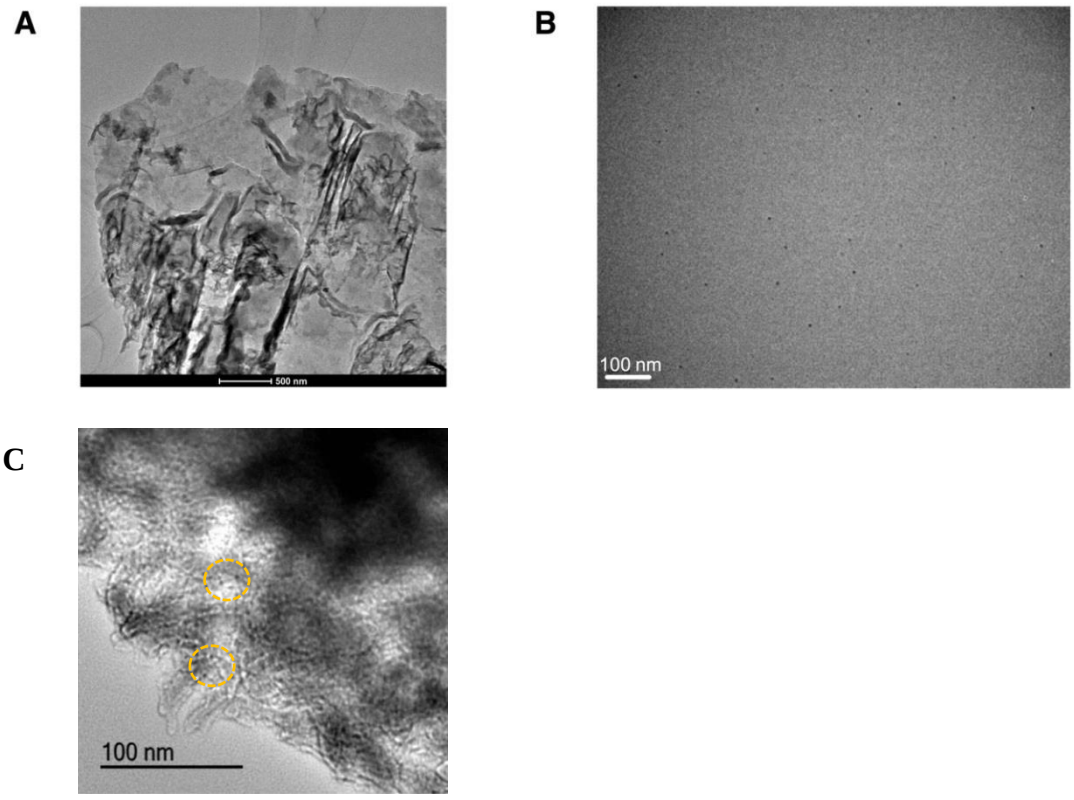

Figure 41. Low magnification TEM image of GCNN (A), CQD prepared by the microwave-assisted method (B) and nanocompositie of CQD (marked by circles)/GCNN (C).

continuous oxidation etching of the bulk GCN layers (Figure 41A).[32] The

diameter of the CQD is 2-10 nm (Figure 41B). HRTEM images (Figure 40C) of some flat areas of GCNN show hexagonal lattice fringes with a typical d-spacing of 0.63 nm, which matches well with the (110) planes of GCN (a = 1.277, c = 0.649 nm in Figure 40C).[32] Both low and high-resolution TEM images of the CQD/GCNN nanocomposite are shown in Figure 40D and 41C. It is evident that those CQDs are coherently embedded or bonded within the GCNN matrixes, confirming the close contact between the two phases. The crystal structure of GCNN was relatively more sensitive to the electron beam irradiation and was therefore damaged, but that of CQD remained intact. The crystal structure of CQD might influence their functions. By TEM, one can confirm that the CQD synthesised here are graphite structure ones. The d-spacing of about 0.23 nm observed in the inset of Figure 40D can be indexed to the (110) planes of a 2 x 2 x 1 hexagonal super unit cell of graphite with a = 0.46 and c = 0.67 nm. Notably, the high magnification images reveal that CQD seems to be concentrated around the GCNN edges and boundaries, which enhances the hole transfer process to water during photocatalysis, as discussed further on. UV-visible diffuse absorption spectroscopy (UV-vis in Figure 40b) confirms that CQD has a generally stronger absorption than GCNN and the absorption of

GCNN photocatalyst is relatively enhanced after loading CQD, especially in the visible region.

6.3.1.2 Photocatalytic activity of CQD/GCNN

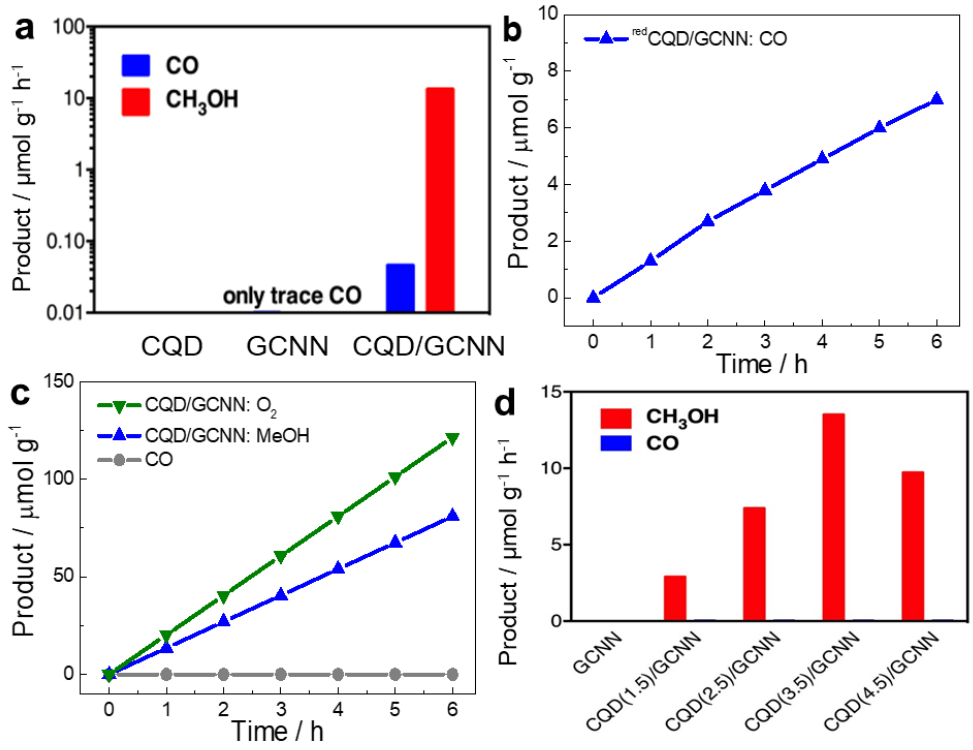

Figure 42. (a) Control experiments of CO_2 conversion on CQD, GCNN, physical mixture of CQD and GCNN and the CQD/GCNN composites. (b) ^{red}CQD/GCNN nanocomposite photocatalysts under visible light (> 420 nm) in 10 mL CO_2 saturation aqueous solution with 10 mg photocatalyst ; (c) Photocatalytic conversion of CO_2 by the CQD/GCNN and (d) Photocatalytic CO and CH_3OH evolution over samples of GCNN, CQD(1.5)/GCNN, CQD(2.5)/GCNN, CQD(3.5)/GCNN and CQD (4.5)/GCNN. The values of 1.5, 2.5, 3.5 and 4.5 are corresponding to the mass ratio between CQDs and DCDA precursor in percentage (1.5%, 2.5%, 3.5% and 4.5%, respectively) before the synthesis.

After preparation of these junctions, the activity of the photocatalysts for reduction of CO_2 by water was evaluated under 1 bar

of CO_2 at room temperature under 300 W Xenon light source irradiation. For comparison, control experiments (Figure 42a) were first performed i) without a CO_2 feed (for CQD/GCNN nanocomposite), ii) in the absence of a photocatalyst and iii) in the absence of light. Under these conditions, the production of both CO and methanol were negligible, indicating that the GCNN and CQD couldn't be decomposed to the products during the experiments. Also, CQD itself showed nearly zero activity, and only a trace amount of CO was photocatalytically produced by pure GCNN. The physical mixture of CQD and GCNN was also tested and showed no evident improvement in activity compared to pure GCNN. The ^{red}CQD was synthesised at the reported optimal concentration of 3%. As for ^{red}CQD/GCNN (Figure 42b), only a small amount of CO was detected as a reduction product with negligible oxygen signals on GC, which might have dissolved in water, consumed via back reactions or was produced with too small concentration. Oxygen was also not observed on the reference material, which is probably due to the same reason.

In contrast, the CQD/GCNN nanocomposite exhibited a remarkably enhanced activity for CO_2 photoreduction with water as the only source of electrons (Figure 42c). The concentration of CQD was

optimised to 3.5% by weight concerning the DCDA precursor (Figure 42d), which is believed to better balance light absorption and water oxidation reaction sites. Further increasing the CQD concentration would block light absorption of GCNN. The yields of both methanol and CO on CQD (3.5)/GCNN increase nearly linearly over time and the average production rates are 13.5 μmol g^{-1} h^{-1} and 0.05 μmol g^{-1} h^{-1} under visible light irradiation (λ > 420 nm).

The apparent quantum yield (AQY) of the optimised CQD/GCNN photocatalyst was measured to be 1.05% at 420 nm under 1 bar conditions at room temperature, which is over an order of magnitude higher than the recently reported on g-C_3N_4 (0.076 %).[24] Neither H_2 nor oxidation products other than O_2 were detected. More interestingly, the selectivity of methanol over CO as the CO_2 reduction products is ~99.6% (Figure 42a). Therefore, the enhanced photocatalytic activity is attributed to the cooperative "synergy" between GCNN and CQD in the nanocomposite, where intimate interfacial contact or binding was created, as discussed above. Moreover, O_2 is evolved as the only oxidation product on the optimised sample and the amount evolved increases linearly with the reaction time, similar to the production profile of CO and methanol (Figure 42c). The ratio of O_2 to methanol is

about 1.45:1, very close to the expected stoichiometric ratio of 1.5:1 when assuming all generated electrons reduce CO_2 to methanol and all holes oxidise water to O_2.

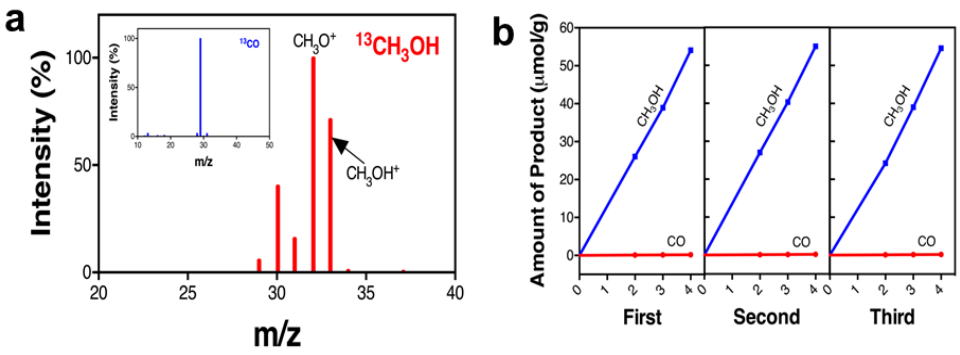

Figure 43. (a) MS spectra of the product $^{13}CH_3OH$ from $^{13}CO_2$ photoconversion by the CQD/GCNN photocatalyst. The inset is the MS spectra of the ^{13}CO from $^{13}CO_2$ photoconversion over the CQD/GCNN photocatalyst.. (b) Consecutive three runs of CO_2 photoconversion to methanol by the CQD/GCN under visible light.

To further confirm the conversion of CO_2, the photoreduction of ^{13}C-labeled CO_2 was conducted over the CQD/GCNN photocatalyst. Dominant peaks of ^{13}CO (m/z =29) and $^{13}CH_3OH^+$ (m/z =33) were observed (Figure 43a). The peak of m/z =32 is assigned to the fragments of $^{13}CH_3O^+$ produced during the MS measurement. All the evidence indicate that the evolved CO and methanol originate from the photoreduction of $^{13}CO_2$ rather than other carbon-containing contaminants adsorbed on the catalyst surface. Therefore, water has

been successfully used as the sole electron donor in the photoreduction of CO_2 and for the first-time methanol was produced with nearly unity selectivity in one step under visible light. Three consecutive runs were carried out over the CQD/GCNN photocatalyst (Figure 43b) to investigate the stability of the as-prepared samples. The CO and methanol evolution rates do not show noticeable changes after three cycles of testing, indicating the excellent stability of the nanocomposite.

6.3.1.3 Functions of CQD cocatalysts

As the discussion above, the majority of the reported CQD promote reduction process as an electron acceptor while few reports are for a hole acceptor. Therefore, after the experimental observation of CO_2 conversion on both CQD/GCNN and the reference ^{red}CQD/GCNN junctions, I collaborated with Dr. Robert Godin and Prof. James Durrant at Imperial College to investigate the charge transfer function and charge dynamics on these two junctions, to understand

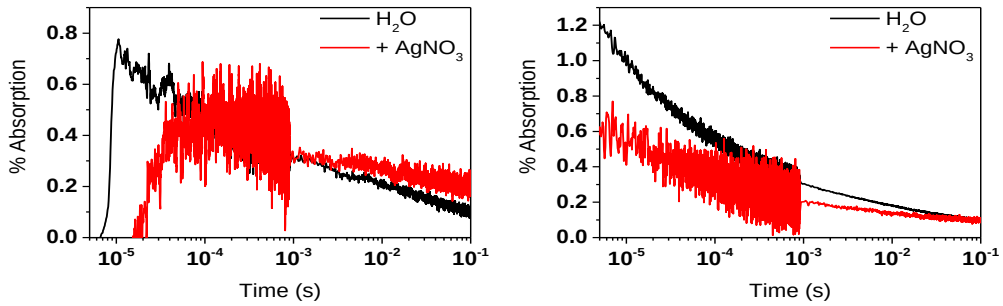

Figure 44. TAS kinetics probed at 510 nm (left) and 700 nm (right) of GCNN dispersed in H_2O (black) and 10 mM AgNO3 aqueous solution (red).

the function of these two CQDs on GCNN. Transient absorption spectroscopy (TAS) as the most sensitive technique for observation of charge transport and separation, was used to experimentally determine the charge carriers' dynamics which would be responsible for the improved activity and pronounced selectivity of the CQD/GCNN nanocomposite. Inspection of kinetic traces probed at 510 nm, and 700 nm of GCNN dispersed in H_2O with and without Ag^+ (Figure 44) show that while electrons are scavenged by Ag^+, the amplitude at 700 nm decreases, the 510 nm signal enhances and features a longer-lived species. Ag^+ ions are well known as an efficient electron scavenger; its addition will yield more long-lived holes, therefore and the signal observed at 510 nm is mainly assigned to photogenerated holes in GCNN and the signal observed at 700 nm is contributed to electrons.

Further observation at different wavelengths reveals that photoexcitation of the GCNN yields a broad absorption spanning from

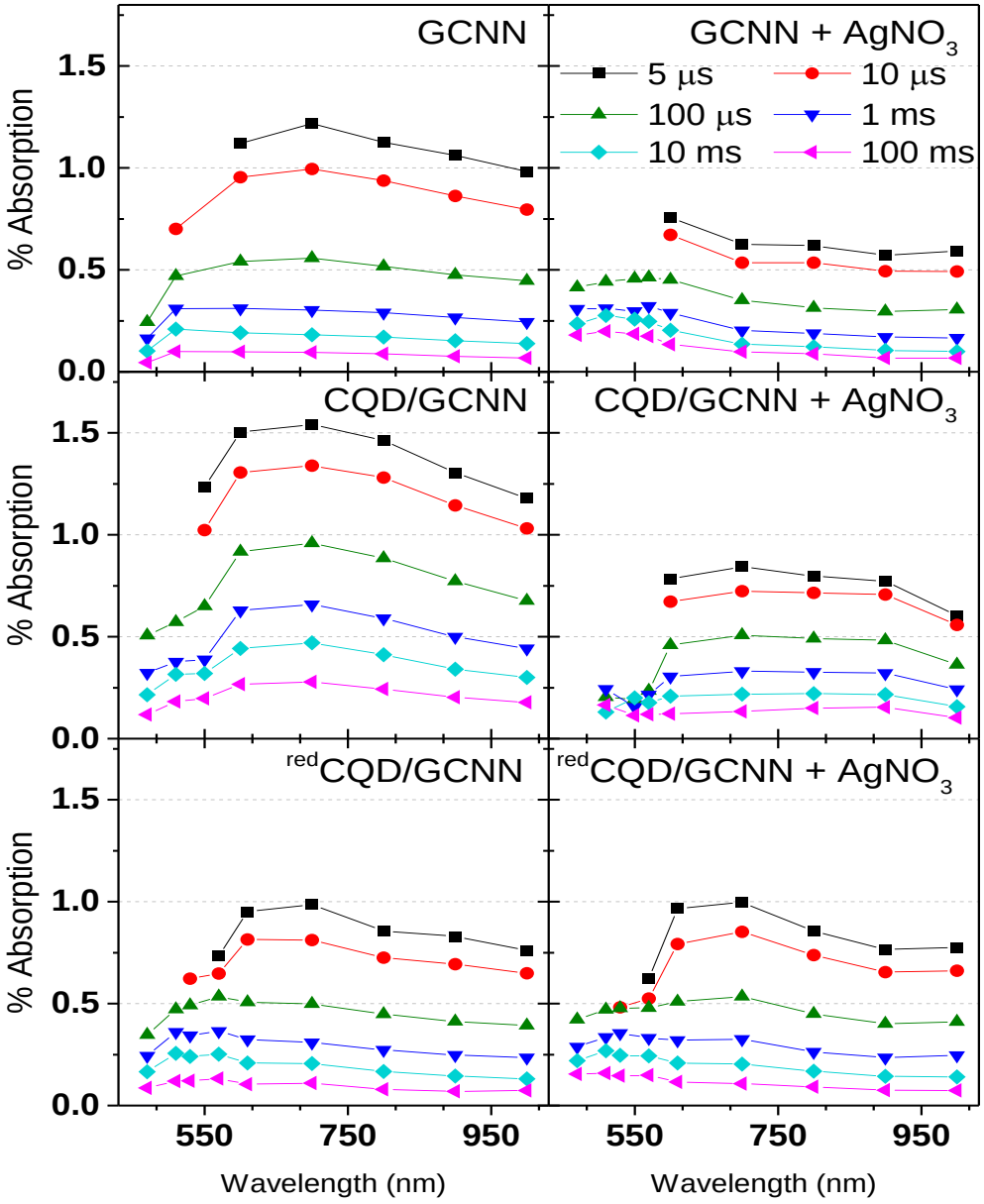

Figure 45. Diffuse reflectance TAS spectra for samples with (right) and (without) 10 mM $AgNO_3$. GCNN (top), CQD/GCNN (middle) and ^{red}CQD/GCNN (bottom) dispersed in aqueous solution. Time delays are the same for the 3 panels and are indicated in the legend of the middle panel. The change of signal amplitude at 700 nm indicates it should be mainly assigned to the electron signal in GCNN, and that CQD improves the charge separation on GCNN due to hole transfer from GCNN to CQD.

450 nm to 1000 nm and peaking near 700 nm (Figure 45 top-left). To determine the nature of the excited state, the TAS spectra were measured again in the presence of a strong electron scavenger (10 mM $AgNO_3$) (Figure 45 top-right). The absorption signal at long wavelength (> 650 nm) is significantly reduced in the presence of the Ag^+ ions and is accordingly assigned to photogenerated electrons in GCNN similar to previous observations on GCN.[18]

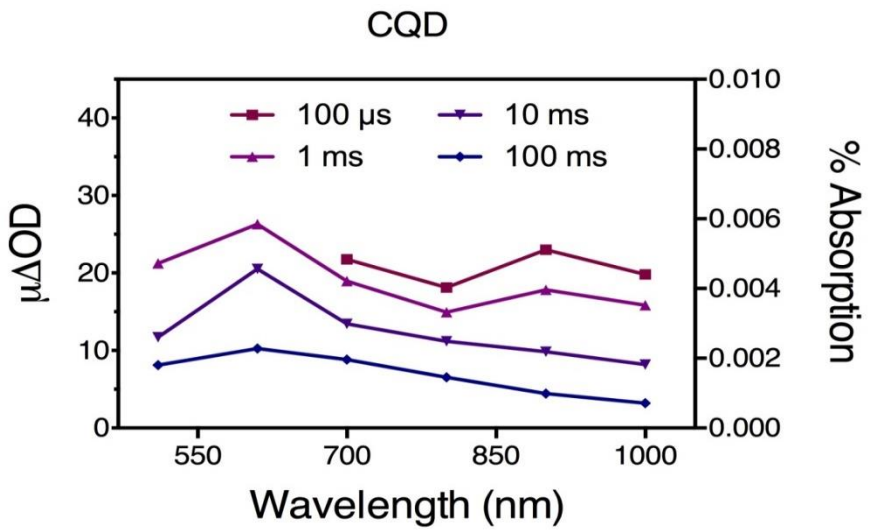

Figure 46. Transmission TAS spectra of CQD (0.6 mg/mL) in aqueous solution.

In the case of the CQD/GCNN nanocomposite (Figure 42 middle), the TAS profile resembles that of the GCNN rather than the isolated CQD (Figure 46). Moreover, the change in optical density is on the

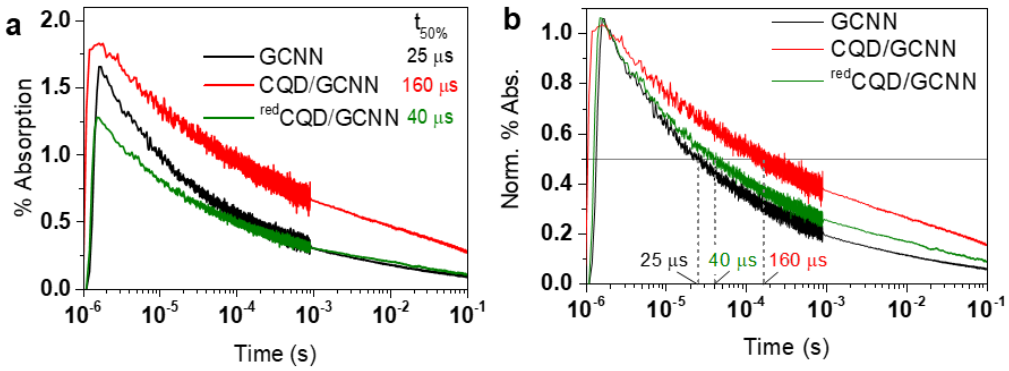

Figure 47. a. Decay kinetics of GCNN (black), CQD/GCNN (red) and ^{red}CQD/GCNN (green) probed at 700 nm. The half-life (where t0 = 2 µs) is indicated to the right of the legend. b. Decay kinetics of GCNN (black), and CQD/GCNN (red) and ^{red}CQD/GCNN (green) probed at 700 nm (assigned to photogenerated electron signal in GCNN) and normalized at 2 µs. A horizontal line is drawn at 0.5, and the crossing with the data is used to determine the decay half-life ($t_{50\%}$).

order of 1% for GCNN and the CQD/GCNN (Figure 45 middle), while it is on the order of 0.005% for CQD. These considerations indicate that the major light absorber is GCNN and the main feature for the CQD/GCNN nanocomposite remains that of electrons localised in GCNN. Compared to the results with GCNN, the amplitude of the broad 700 nm feature (electron signal in GCNN) is higher in the case of the CQD/GCNN (Figure 45 middle), suggesting that hole transfers to CQD, leading to efficient charge separation and more long-lived electrons at these timescales. Further adding Ag+ (Figure 45 middle-right), the signal at long wavelength decrease, again proving this is attributed to photogenerated electrons.

Also, the half-life time (for an initial time t_0 = 2 μs) of the signal observed at 700 nm increases over 6-fold from 25 μs to 160 μs (Figure 47), indicating suppressed charge recombination due to CQD loading, which is consistent with charge separation across the CQD/GCNN junction.

On the other hand, the TAS spectra for the GCNN in the presence of the Ag^+ ions introduces an enhanced signal around 510 nm (Figure 44a). The TAS spectra on three samples of GCNN, CQD/GCNN and ^{red}CQD/GCNN (dispersed in water, with and without Ag^+) are further compared in Figure 45. Close observation can find that the 510 nm signal is suppressed relative to the signal at 700 nm when loading CQD on GCNN junction (Figure 45 top). This direct evidence supports that holes photogenerated in GCNN are transferred to the CQD, and further consistent with the enhanced signal of electrons on GCNN mentioned above.

In contrast, ^{red}CQD/GCNN shows a smaller signal amplitude throughout the probed window, and the addition of $AgNO_3$ does not affect the signal (Figure 45 bottom). A peak near 550 nm for ^{red}CQD/GCNN was also noted, in line with the hole signal observed for GCNN, and a slight increase in the $t_{50\%}$ (from 25 μs to 40 μs) compared

to bare GCNN (Figure 47) attributed to separation of charges by ^{red}CQD. These observations are consistent with the hypothesis of the extraction of electrons from GCNN by ^{red}CQD. Overall, clear evidence of different functions of two CQD could be seen for charge separation and that the specific CQD/GCNN interaction can influence the direction of charge transfer.

Therefore on CQD/GCNN electrons accumulate on the GCNN, where they proceed to reduce CO_2, and holes are transferred to the CQD, where they proceed to oxidise water.

Theoretical calculations based on the Density Functional Theory (DFT) were also employed to elucidate the high efficiency of CQD/GCNN junction for CO_2 reduction. The calculations were carried out using the Vienna ab-initio Package (VASP), in collaboration with Dr Xiaoyu Han[34] Detailed computational settings are illustrated in Chapter 6.2.3. To mimic the structure of the CQD, the model consists of a coronene with a pyrene on the top. It was placed in a 20 × 20 × 10 $Å^3$ box. Two nano-flakes were symmetrically mass-centred with a relaxed interlayer distance of 3.37 Å, which is in line with the XRD and HRTEM observation (Figure. 40A and D). This model has been proven effective

to mimic the CQD.[35] For the GCNN, the models have adopted using the structures observed in the previous calculations.[18]

Table 10 Adsorption energies (eV) of CO_2 and CH_3OH on the CQD and GCNN.

	CO_2	CH_3OH	H_2O
CQD	-0.11	-0.29	-0.23
GCNN	-0.28	-3.96	-0.08

The adsorption energy, E_{ad}, was calculated according to $E_{ad} = E_{total} - (E_{adsorbate} + E_{adsorbent})$, where E_{total}, $E_{adsorbate}$ and $E_{adsorbent}$ represent the energies of the absorbing system, the adsorbate and the adsorbent at equilibrium configurations, respectively. The results for the most stable configurations are listed in Table 10. Energetically, both CO_2 and CH_3OH more favourably bind to porous GCNN (Figure 48. A and B) than CQD, especially for the final product CH_3OH. The situation reverses for the adsorption of H_2O, where CQD show the stronger interaction (Figure 48.C). Hence, the CO_2 reduction preferably occurs on the GCNN where electrons accumulate, while H_2O is oxidised on the CQD where holes gather after photoexcitation. The GCNN and CQD in the nanocomposite selectively adsorb CO_2 and H_2O and more

importantly separate the electrons and holes efficiently, as experimentally confirmed by TAS.

Based on the above experimental results, a proposed pathway of the visible light-driven CO_2 photoconversion combined with water splitting by the CQD/GCNN is presented in Figure 48d. Under visible light irradiation, the GCNN are excited to generate electron-hole pairs. The photoexcited electrons are gradually consumed in photoreduction of CO_2 to CH_3OH (and a small amount of CO) on the surface of GCNN, while the CQD act as an efficient hole acceptor and provide active sites for water oxidation as a cocatalyst. Thus, the photogenerated holes from GCNN would reach the surface of the CQD to oxidise water into O_2 efficiently. On the other hand for ^{red}CQD/GCNN, the ^{red}CQD acts as an electron acceptor where CO_2 reduction takes place and produce CO while water is oxidised by the holes on carbon nitride. CQD/GCNN photocatalyst also showed some photocatalytic activity even under 500 nm or 600 nm light irradiation (AQY = ~0.27% at λ = 500 nm and ~0.13% at λ = 600 nm), which might be due to the light absorption effect of CQD as GCNN couldn't harvest 500~600 nm photons by itself

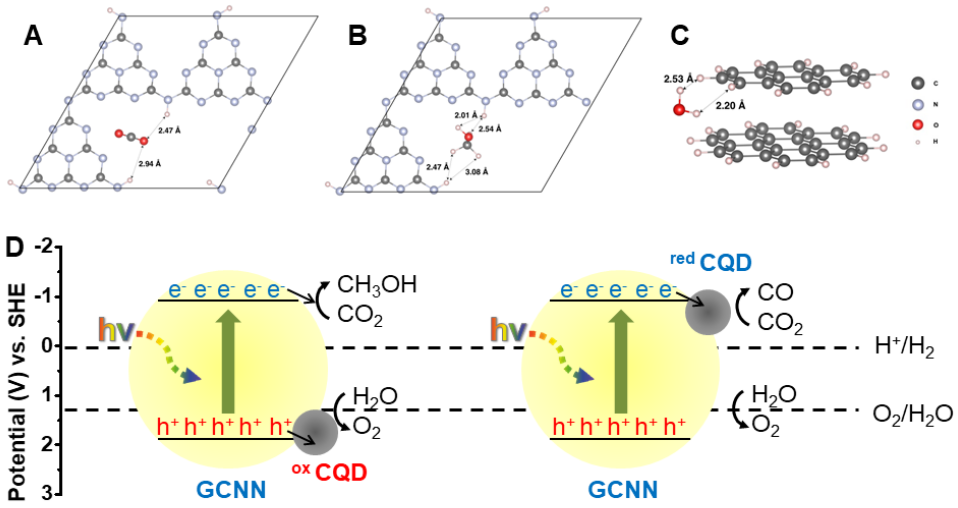

Figure 48. The most stable configurations of CO_2 (A) and CH_3OH (B) on porous GCNN and H_2O on CQD (C). (D)Schematic diagram of photocatalytic CO_2 reduction by the CQD/GCNN (electron donor CQD) and ^{red}CQD/GCNN (electron acceptor CQD).

6.3.2 CO_2 conversion on CQD/FAT junctions

After confirming the function of novel CQD synthesised from the microwave-assisted method on GCNN, the concept of a metal-free photocatalytic junction for CO_2 conversion has been proved. Further, I optimise such CQD and load them on the best polymers FAT as discussed in Chapter 5 to perform efficient CO_2 conversion into liquid fuels, *e.g.* methanol. In this section, the synthetic microwave power for

CQD, the loading amount of CQD, and the pH of solution have been carefully optimised to get the optimal activity for CO_2 photoreduction.

6.3.2.1 Characterisation of CQD/FAT junction

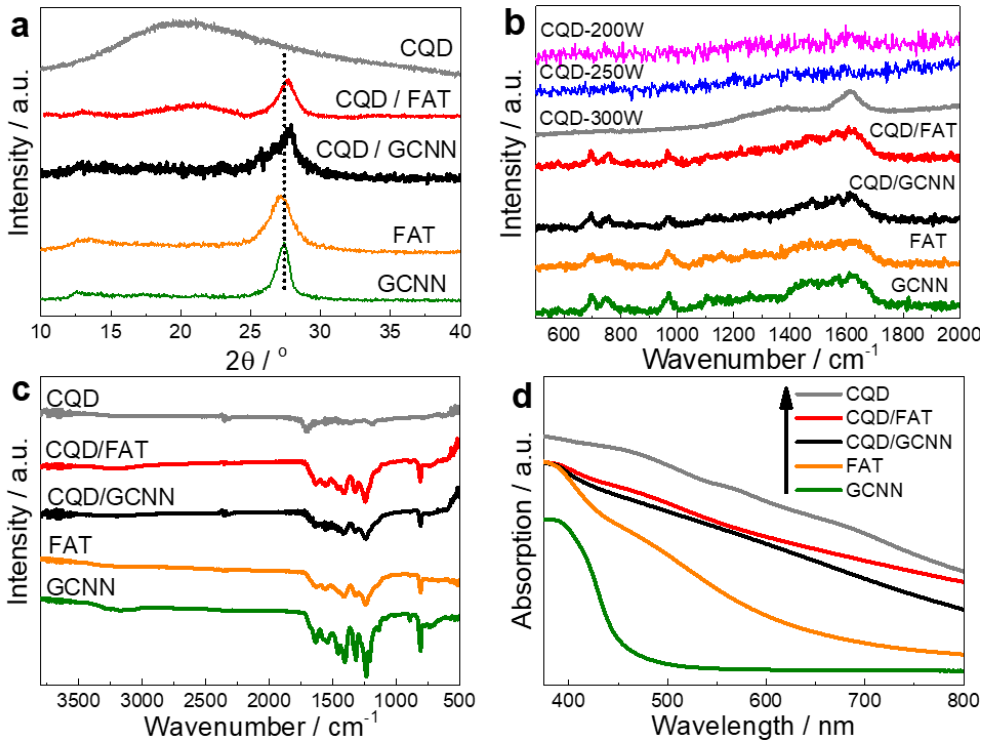

Figure 49. (a) XRD patterns, (b) Raman spectra, (c) FT-IR spectra and (d) UV-vis spectra of samples.

For comparison, CQD/GCNN junction together with pure FAT and GCNN have also been investigated as references. Firstly, thorough characterisations have been carried out to study the structure and composition of the junction photocatalysts. According to XRD patterns (Figure 49.a), similar as the description in the section 6.3.1, CQD show

a broadened band around 20° ((002), d-spacing of 4.43 Å) compared to graphene in literature (26.5°, 3.36 Å), indicating an enlarged interlayer distance due to a disordered stacking manner which is commonly observed during N doping.[242-243] FAT and GCNN were also synthesised as proved by the typical diffraction signals of (002) and (100) at 27.1° (3.29 Å), 13.3° (6.65 Å) and 27.4° (3.26 Å), 13.0° (6.82 Å), respectively.[67] Surprisingly, after coupling them with CQD, the interlayer distances of both CQD/FAT and CQD/GCNN have been compacted to 3.20 Å (27.8°), suggesting the formed junction possesses stronger interaction and attraction, which might be beneficial to charge transfer between CQD and polymers.

Raman spectroscopies were used to examine the backbone of materials (Figure 49.b). Characteristic vibrations of the heptazine-based 2D structure have been found on FAT, GCNN, CQD/FAT and CQD/GCNN, with the peaks in the regions of 1200-1700 cm^{-1}, 980 cm^{-1} and 690 cm^{-1} corresponding to disordered graphitic carbon-nitrogen vibrations, the symmetric N-breathing mode of heptazine and the in-plane bending, respectively.[202-203] For CQD synthesised at different microwave powers (Figure 50.b), 200 and 250 W powers couldn't produce CQD with obvious graphitic signals. Only CQD-300W has a

clear graphitic structure of D-band around 1350 cm^{-1} and G-band around 1600 cm^{-1} with a low-intensity ratio (I_D/I_G) of *ca.* 0.28 (compare to previously reported Hummer method), implying the CQD-300W still maintains a relatively integrated sp^2 structure of graphene.[210, 244-245]

FTIR spectroscopy was carried out to identify the assignment of proposed structure (Figure 49.c). FAT shows similar trends to GCNN except that signals related to C-NH_x at 1200 cm^{-1} and 1450 cm^{-1} decline due to the replacement of linker N atoms by O and the triple peaks of NH_x around 3000-3300 cm^{-1} change to a broad band of -OH signal.[67] Besides C-C vibrations at 1200 cm^{-1} and 1450 cm^{-1}, CQD also displays weak signals around 1250-1550 cm^{-1} of C-N vibrations and peak of C=O around 1730 cm^{-1}, suggesting N and O dopants on graphene.[245-246] As for the two junction samples, apart from the peaks of pristine FAT and GCNN, one can still see the less pronounced C-N vibrations of CQD (1250-1550 cm^{-1}) which are different from heptazine characters, confirming the co-existence of CQD and polymers. And the C=O peak submerges in junctions due to either the small amount of CQD existence or their reaction during the annealing. The peaks between 2250 to 2550 cm^{-1} are attributed to CO_2 from the air.

According to UV-vis spectroscopy (Figure 49.d), CQD absorbs light extensively from UV, visible to near IR, much broader compared to the absorption of FAT and GCNN. Interestingly, even with only ~10% w.t. CQD, both junctions exhibit dramatically enhanced absorption towards IR, close to the absorption of CQD, which indicates the junctions are mixtures of CQD with polymers. It should be noted that the bandgaps of FAT and GCNN are slightly larger than previously reported (FAT: 1.9 eV and GCNN: 2.7 eV).[67] Such enlargement is due to the second annealing of both polymers which removes potential defects and increase the polymerisation degree.[50]

X-ray photoelectron spectroscopy (XPS) was also used to identify different elements (C, N, O) and the chemical states in CQD, FAT, GCNN and junctions, as listed in Table 11-14. XPS survey spectrum of CQD shows its surface chemical composition of 11.86% N, 61.99% C and 26.15% O. [210] Different from the rest samples; obvious C=O signals are only observed in CQD, which agrees with FT-IR spectrum. The compositions of C and N states are similar to the reported.[67] Concerning the O 1s XPS spectra, it could be found that all samples have C-OH on the surface, which is favourable for intimate interaction between CQD and polymer layers during junction fabrication due to

hydrogen bonds and also turns the hydrophobic surface into hydrophilic to promote the contact with water.[247]

Table 11. Surface compositions of C, N, O from XPS spectra for samples used in this study

Sample	C (at %)	N (at %)	O (at %)
CQD (herein)	61.99	11.86	26.15
GCNN	48.41	49.26	2.33
FAT	50.30	42.59	7.11
CQD/GCNN	49.19	47.17	3.64
CQD/FAT	51.10	45.09	3.81

Table 12. Compositions of C 1s XPS spectra for samples used in this study

Sample	C=O (289 eV)	C-N (287.5 eV)	C-O (286.2 eV)	C-C (284.6 eV)
CQD	22.32	25.05	10.55	42.08
FAT	-	62.09	8.51	29.40
GCNN	-	61.83	3.67	34.51
CQD/FAT	-	60.06	13.70	26.24
CQD/GCNN	-	65.39	11.35	23.26

Table 13. Compositions of N 1s XPS spectra for samples used in this study

Sample	NH_x (401 eV)	$N\text{-}C_3$ (400 eV)	C=N-C (398.7 eV)
CQD	33.14	51.18	15.68
FAT	6.74	45.05	50.20
GCNN	9.31	26.41	64.27
CQD/FAT	14.39	20.26	65.35
CQD/GCNN	16.27	26.47	57.25

Table 14. Compositions of O 1s XPS spectra for samples used in this study

Sample	O=C (534 eV)	C-O-C (533.2 eV)	$C\text{-}H_2O$ (532.5 eV)	C-OH (531.5 eV)
CQD	35.67	-	-	64.33
FAT	-	34.48	46.79	18.72
GCNN	-	-	46.48	53.52
CQD/FAT	-	41.74	-	58.26
CQD/GCNN	-	-	76.22	23.78

6.3.2.2 Photocatalytic activity of CQD/FAT junctions

After understanding the structure of synthesised junction photocatalysts, their performance for artificial photosynthesis was evaluated at 1 bar condition under irradiation of 300 W Xenon light source with a light intensity of 100 mW (420 nm < λ < 710 nm), which is close to practical environmental conditions. No product such as

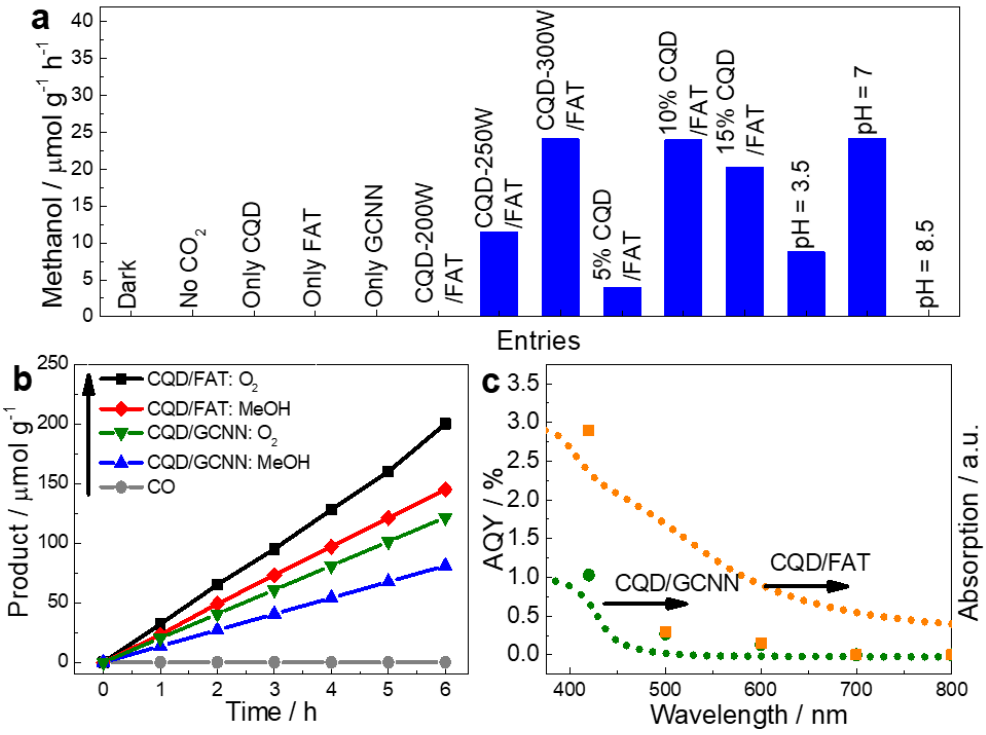

Figure 50. (a) Comparison of methanol production under different conditions including control experiments, CQD at different synthetic microwave powers, mass ratios and pH values when using 10% CQD/FAT as a photocatalyst. (b) Artificial photosynthesis from CO_2 and water on CQD/FAT and CQD/GCN. (c) Apparent quantum yield (AQY) of CQD/FAT and CQD/GCN. Conditions: 1 bar pressure, visible light with 100 mW intensity (420 nm < λ < 710 nm).

methanol or CO was detected under dark conditions, with argon feed gas (no CO_2) or only in the presence of CQD, FAT or GCNN

photocatalysts respectively (Figure 50.a), excluding the possibility of dark reactions, decomposition of organics or CO_2 reduction occurring on either polymeric photocatalyst. Surprisingly, methanol (instead of CO) and O_2 are selectively produced from CO_2 and water at rates of 24.2 and 32.0 $\mu mol \cdot g^{-1} \cdot h^{-1}$, respectively, when CQD and FAT are coupled together. Moreover, its product ratio of 1:1.32 (Figure 50.b) is close to the stoichiometric ratio (1:1.5) of formula $2CO_2 + 4H_2O = 2CH_3OH + 3O_2$, confirming the balance between fluxes of excitons. The reason for a smaller amount of O_2 than ideal ratio might be that some O_2 are dissolved in water.

Similar to natural photosynthesis, such reaction is consisted of two half reactions: $CO_2 + 6H^+ + 6e^- = CH_3OH + H_2O$ (CO_2 reduction) and $2H_2O + 4h^+ = O_2 + 4H^+$ (water oxidation). As illustrated by the charge transfer routine in 6.3.1 , the CO_2 reduction is attributed to FAT polymer, and the O_2 production occurs on CQD. When coupling FAT with CQD synthesised at different microwave powers (200, 250, 300 W), the junctions show an increasing trend in activity as the power goes up from 200 W to 300 W (Figure 50.a), which agrees with the degree of graphitisation according to Raman spectra (Figure 50.b). On the one hand, sp^2 hybrid structure formation in CQD ensures an optical gap for

π–π* excitation and is more stable during junction synthesis.[248] On the other, the similarity of 2D structure between FAT and CQD benefits the stacking of layers and enhances the contact between interfaces for promoted charge transfer, which is the key in junction construction. In other words, both FAT and CQD herein play the roles for CO_2 reduction and water oxidation, respectively.

The weight ratio between CQD and FAT has been optimised to be 1:10 (Figure 50.a, 10% CQD/FAT), as a lower or higher ratio, would not balance the exciton fluxes due to light absorption and charge relaying process, thus decreasing the activity.[18] Also, the starting pH of the system influences the state of CO_2 in water. In this study, CQD/FAT junction works stably under neutral pH where CO_2 reacts with water to produce protons and HCO_3^-. No activity was detected at pH = 8.5 likely because of the lack of protons, although a higher pH increases the solubility of CO_2 by converting CO_2 into CO_3^{2-}.[249] An acidic condition resulted in decreased activity because CO_2 solubility declined sharply at low pH.

As previously reported in Chapter 5, the acceptor-donor nature of FAT polymer results in a more positively positioned CB (consequently a narrower band gap) and better charge separation than GCNN, resulting

in over an order of magnitude enhancement than GCNN in H_2 production, proving that the charge separation rather than driving force is assigned to the rate-determining step. For 6-elections CO_2 reduction process, different from the 2-electron H_2 production, the enhancement of activity on FAT is only around twice that on GCNN. In other words, the advantage of FAT for CO_2 conversion is not as much as its superiority for H_2 production over GCNN. With CQD acting as efficient hole acceptor in junctions to take holes from both polymers, the lifetime of electrons in both junctions has been prolonged. Further, apparent quantum yield (AQY) was calculated on both junctions to determine the efficiency of harvesting photons to undergo redox reactions. Both samples show the highest AQY at 420 nm, indicating the activity in the near-visible region dominates the efficiency. CQD/FAT exhibits an AQY of 2.9% at 420 nm which is 2.6 times of the CQD/GCNN (1.1%) (Figure 50 C). At longer wavelengths of 500 and 600 nm, both CQD/FAT and CQD/GCNN demonstrate similar AQY, suggesting activity at such wavelengths is likely related to the visible photon harvesting of CQD.

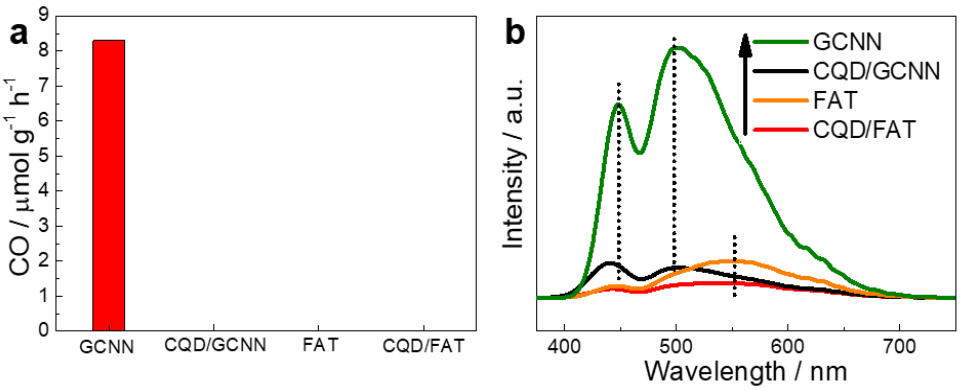

Figure 51. (a) The CH_3OH oxidation test on FAT, GCNN, CQD/FAT and CQD/GCNN samples. Conditions: Conditions: 1 bar pressure of Argon, visible light with 100 mW intensity (420 nm < λ < 710 nm). 20 ml H_2O, 2 umol CH_3OH and 10 mg photocatalysts. (b) Photoluminescence spectra (325 nm laser excitation)

The CO_2 selective reduction to methanol caught substantial interest as methanol is an easy-to-handle liquid product compared to CO and CH_4 but is rather easy to oxidise because $CH_3OH + 4h^+ = H^+ + CO$ (ΔG^0 = 22 kJ/mol) is thermodynamically favourable compared to water oxidation (ΔG^0 = 237 kJ/mol).[250-252] However, the actual oxidation of methanol could be slowed down if methanol is poorly adsorbed on oxidation sites of a catalyst.[250] To reveal whether the catalysts used in this study could efficiently oxidise CH_3OH to CO/CO_2, the methanol oxidation tests were carried out on FAT, GCNN, CQD/FAT and CQD/GCNN samples (Figure 51.a). In the presence of 2μmol CH_3OH under 1 bar argon, surprisingly, GCNN continuously converted methanol to CO, while CQD/GCNN couldn't, agreeing with my observation that methanol cannot be able to be easily oxidised on CQD

and remains as the main product herein. The reasons behind such phenomenon include when methanol is absorbed on GCNN, it can be oxidised by photoholes on GCNN, while on CQD/GCNN junction, holes accumulate on CQD not on GCNN, leaving no photoholes on GCNN to oxidise CH_3OH. This is another indirect evidence of charge transfer between CQD and GCNN, otherwise the junction should also oxidise methanol and produce CO. Interestingly, neither FAT nor CQD/FAT oxidises CH_3OH under the identical conditions, indicating that there might not be active sites on FAT to oxidise methanol or methanol is unfavourably adsorbed on FAT, which is probably another reason for a higher activity of CQD/FAT.

To rationalise the superior performance on such a challenging process, I turned to spectroscopies to investigate the reason. Photoluminescence spectroscopy (PL) was undertaken to examine the radiative recombination on the samples (Figure 51.b). In the PL spectra, the two junctions show the same peak positions as that of FAT and GCNN even after coupling with CQD, maybe because of low amount CQD loaded, Both GCNN and CQD/GCNN exhibit two signals relative to π–π* and n–π* excitation but the CQD/GCNN (max 9,211 a.u.) shows one order of magnitude lower intensity than pure GCNN (max 75,491

a.u.), indicating an enhanced charges separation due to the junction structure.[165] on the other hand, the major peaks on FAT and CQD/FAT are around 550 nm with peaks at 450 nm negligible due to band gap narrowing, consisting with Chapter 5.[67] CQD/FAT (max 4,373 a.u.) also has weaker intensity compared to pure FAT (max 11,296 a.u.), indicating a dramatically mediated charge recombination by CQD. This explains that the promoted performance is related to the suppressed charge recombination caused by the spatial separated electrons and holes in the junctions. The better performance of CQD/FAT compared with CQD/GCNN is believed due to the intrinsic superiority of FAT to GCNN on the suppressed charge recombination as evidenced in Chapter 5.

6.4 Summary

To conclude, a few junctions of CQD/polymer have been successfully synthesised and tested for CO_2 conversion by photocatalysis operated at ambient conditions. Regarding the two kinds of CQD coupled with polymers in this Chapter, the ^{red}CQD/GCNN junction converts CO_2 into CO while the CQD/GCNN junction could directly and selectively reduce CO_2 to methanol, which has been further confirmed by carbon-13 isotope labelling. The difference in selectivity

between these two junctions is attributed to the difference of functions of two kinds of CQD. Time-resolved absorption spectroscopies show that the ^{red}CQD work as an electron acceptor in red-CQD/GCNN while the graphite structure CQD work as the photogenerated hole acceptor instead of electron acceptor after excitation, thus prolonging the lifetime of the charge carriers in the CQD/GCNN photocatalyst. Furthermore, such CQD show more favourable water adsorption yet unfavourable methanol adsorption compared with GCNN, thus facilitating oxidisation of water to O_2 while avoiding oxidation of the photoreduction product, methanol. Therefore, CQD is a key reason for such high selectivity towards methanol. Electrons reach the surface of GCNN and possess sufficient chemical potential to reduce CO_2, together with protons, to produce mainly methanol (99.6% selectivity) with a small amount of CO. As a result, the nanojunction photocatalyst shows very effective visible light-driven photocatalytic activity for direct CO_2 reduction to methanol using water as the only hole scavenger, and an apparent quantum yield of 1.05% at 420 nm. The novel CQD synthesised from microwave-assisted method was then coupled with FAT polymers developed in Chapter 5 to form another junction for CO_2 reduction which selectively produces methanol and oxygen in a

stoichiometry ratio with apparent quantum yield of 2.9% and 1% at 420 and 500 nm, respectively, which shows three times higher activity than the CQD/GCNN because of the intrinsic better charge separation property of FAT polymer compared to GCNN. This enhancement has been found dependence on the synthetic microwave powers of CQD, the mass ratio between CQD and polymeric photocatalyst and pH value of 7.

7. Overall conclusions and future work

Visible light-driven Z-scheme water splitting and CO_2 conversion are among the most promising ones to achieve sustainable solar-to-fuel production, which can alleviate the energy and environmental issues by utilising the inexhaustible solar energy, water and CO_2. In the construction of visible light-driven Z-scheme, it is the key to couple reduction and oxidation photocatalysts with suitable band positions together with efficient charge transfer, which relies on the careful design of photocatalysts. Instead of inorganic photocatalysts with poor tunability, polymeric photocatalysts with their good feasibility are more applicable and low-cost. Although polymeric photocatalysts (*e.g.* g-C_3N_4) have attracted substantial attention in the last decade, most of them can only respond to light < 470 nm, which inhibits the utilisation of the strongest region in the solar spectrum (500~700 nm). Also, the rapid charge recombination on polymeric photocatalyst (*e.g.* g-C_3N_4) remains the other obstacle. Therefore, my PhD research is designed to address the two major obstacles for organic semiconductors and consequently construct the visible light-driven photocatalytic system for solar fuel synthesis.

Two innovative strategies to control the linkages in polymerisation have been developed to synthesise one group of highly active, tuneable and narrow band-gap polymers with fine controlled band positions, which actually address the key challenge for efficient photocatalytic H_2 evolution and still maintain a stable structure. Such polymers are further applied in Z-scheme for water splitting and junctions for CO_2 conversion.

1). Predicted by density-functional theory (DFT) calculations, an oxygen-doped polymeric carbon nitride structure has been identified with heptazine chains linked both by oxygen atoms and nitrogen species, which could result in a reduced band gap and efficient charge separation. So a novel synthetic method has then been developed to control both surface hydrophilicity and more importantly, the linker species in a heptazine-based polymer, oxygen and nitrogen co-linked heptazine polymer, denoting ONLH polymers which highly influences the band gap and charge separation. As such, the synthesized polymer can be excited from UV via visible to even near-IR (λ = 800 nm) wavelengths, resulting in a 25 times higher H_2 evolution rate (HER) than the previous benchmark polymeric g-C_3N_4 (λ > 420 nm), with an apparent quantum yield (AQY) of 10.3% at 420 nm and 2.1% at 500 nm,

measured under ambient conditions, which is closer to the real environment (instead of vacuum conditions). Apart from the general similarity in physical characterisations with g-C_3N_4, the crystallinity of ONLH has been weakened according to XRD patterns, Raman and FT-IR spectra. Additional C-O bonds have been observed in XPS spectra of ONLH, confirming the existence of oxygen linkers and terminals and a higher amount of oxygen has been detected by elemental analysis. PL spectra show that the charge recombination has been mitigated after the oxygen linker/terminal incorporation and the bandgap of such polymer has been dramatically narrowed according to Tauc plot, thus harvesting more visible photons. The strategy used here thus paves a new avenue to dramatically tune both the light absorption and charge separation to increase the activity of polymeric photocatalysts.

2) By coupling ONLH polymer and $BiVO_4$ in the presence of $Fe^{2+/3+}$ shuttles, the constructed Z-scheme stably produces both H_2 and O_2 in a stoichiometry ratio. Although the current solar-to-hydrogen efficiency is low, the concept was proved, and further optimisation including the use of surface modifiers (*e.g.* a-TiO_2 and Cr_2O_3) and fabricating the system into solid-state Z-scheme junctions is suggested.

3) The band gap engineering of semiconductors, in particular, low-cost organic/polymeric photocatalysts, could directly influence their behaviour in visible photon harvesting. However, an effective and rational pathway to stepwise change of the band gap of an organic/polymeric photocatalyst is still very challenging. Here an efficient strategy has been demonstrated to tailor the band gap from 2.7 to 1.9 eV of organic photocatalysts by carefully manipulating the linker/terminal atoms in the chains via designed polymerisation. These polymers work stably and efficiently for both H_2 and O_2 evolution at ambient conditions (420 nm < λ < 710 nm), exhibiting up to 18 times a higher hydrogen evolution rate than a reference photocatalyst g-C_3N_4 and leading to high AQY of 8.6%/2.5% at 420/500 nm, respectively. For the oxygen evolution rate, the optimal polymer shows 19 times higher activity compared to g-C_3N_4 with excellent AQYs of 4.3%/1.0% at 420/500 nm. With the amount of formic acid in the precursors increasing from FAT-0 to FAT-1.0, the bandgap has been narrowed, and the radiative charge recombination has been suppressed according to the characterisations. Further increasing the amount of formic acid enlarges the bandgap slightly and doesn't enhance the charge separation. Theoretical modelling shows that such superior

performance is related to the incorporation of oxygen atoms. Briefly, in such polymers the CB locates on the oxygen-linked/terminated chains while the VB stays on the nitrogen chains, thus separating the electrons and holes in polymers spatially and promoting the redox capability efficiently. As the portion of oxygen linker/terminal increases, the bandgap is getting narrower and charge separation is enhanced. Such a phenomenon has a limit because if the amount of oxygen further increases so that oxygen atoms located on both chains, then the bandgap is wide and charge separation is poor again, agreeing with experimental observations. In short, both theoretical modelling and spectroscopies results indicate that such remarkable enhancement is due to the increased light harvesting and improved charge separation.

4) Finally, a more challenging photochemical process of visible light-driven CO_2 reduction in water was investigated using junctions consisting of the novel polymers and two kinds of carbon quantum dots (CQD) cocatalysts. The novel CQD was synthesised via a microwave-assisted method while the other CQD was fabricated via sonication of glucose (^{red}CQD). Regarding the two kinds of CQD coupled with polymers, the ^{red}CQD/GCNN junction convert CO_2 into CO while the CQD/GCNN junction could directly and selectively reduce CO_2 in water

to methanol, which has been further confirmed by carbon-13 isotope labelling. The difference in selectivity between the two junctions is attributed to the difference of functions of CQDs. Time-resolved absorption spectroscopies show that the ^{red}CQD works as an electron acceptor in ^{red}CQD/GCNN while the graphite structure CQD works as the hole acceptor instead of an electron acceptor after excitation, thus prolonging the lifetime of the charge carriers in the CQD/GCNN photocatalyst. Furthermore, such CQD show more favourable water adsorption yet unfavourable methanol adsorption compared with GCNN, thus facilitating oxidisation of water to O_2 while avoiding oxidation of the photoreduction product, methanol. Therefore, CQD is a key reason for such high selectivity towards methanol. Electrons reach the surface of GCNN and possess sufficient chemical potential to reduce CO_2, together with protons, to produce mainly methanol (99.6% selectivity), and a small amount of CO. As a result, the nanojunction photocatalyst shows very effective visible light-driven photocatalytic activity for direct CO_2 reduction to methanol using water as the only hole scavenger, and an apparent quantum yield of 1.05% at 420 nm. The novel CQD synthesised from microwave-assisted method was then coupled with FAT polymers developed in Chapter 5 to form another

junction for CO_2 reduction which selectively produces methanol and oxygen in a stoichiometry ratio with apparent quantum yields of 2.9% and 1% at 420 and 500 nm, respectively, which shows three times higher activity than the CQD/GCNN. The performance is found dependent on the synthetic microwave powers of doped graphene, mass ratio and pH. By tailoring both organic photocatalysts and co-catalysts, a sustainable and efficient solar energy conversion process has been achieved.

Future work

The proposed future work includes the following aspects based on the outcomes achieved during my PhD research:

1) Optimisation of the Z-scheme overall water splitting system by a few techniques. First, to modify the hydrogen evolution polymers, I would suggest trying post-calcination in molten salt to treat the ONLH polymers to enhance the efficiency, which is the method used to fabricate the benchmark polymer for hydrogen evolution half reaction. Also, the coating of surface modifiers (*e.g.* a-TiO_2 and Cr_2O_3) could be applied to the polymers. Second, I would suggest to choose another oxygen evolution photocatalyst or modify the $BiVO_4$ by doping or

cocatalysts. Third, to fabricate a solid-state Z-scheme based the photocatalysts developed, one can seek an efficient solid shuttle such as Ag, Au and carbon and optimise the contact surfaces.

2) The construction of all-polymer-based Z-scheme. So far, the highest reported solar to hydrogen (STH) energy conversion efficiency of around 1% for a particulate system has been achieved using such an inorganic Z-scheme[116], much better than attained on single photocatalysts. A similar approach could be applied to low-cost and tuneable polymeric photocatalysts. One challenge is lacking efficient oxygen evolution polymers. I would suggest first to try coupling FAT polymers as oxygen evolution photocatalysts with hydrogen evolution polymeric photocatalysts, *e.g.* ONLH. Also, the mediators and efficient cocatalysts should be optimised to develop the first all-polymer solid-state Z-scheme system.

3) Further enhancement of CO_2 conversion on CQD/polymer system. One of the reasons for my current inefficient system is that the limited solubility of CO_2 in water. Following the progress, I suggest trying using different solutions to increase the solubility of CO_2, for example, an ionic liquid with excellent CO_2 capture capability. With CQD as the oxidation cocatalyst, one can find some efficient cocatalyst

for the reduction half reaction. For example, some molecular cocatalyst could aid the reduction process.

4) To better understand the mechanism by which polymeric photocatalysts evolve hydrogen and oxygen and the role of defects. In the case of doped carbon nitrides, it has been demonstrated, as discussed above, that linker/terminal groups other than -NH_2 influence the activity, and that defect engineering can be used to improve hydrogen evolution rates.[53, 253] However, it is not yet clear whether these terminal defects play a greater role in controlling the charge carrier dynamics within the carbon nitride or in promoting efficient interfacial charge transfers, or both. Since interfacial reactions (such as proton reduction) typically takes place on microsecond or longer timescales,[254] photoexcited states typically relax and localise before electron transfer. As observed on carbon nitride, this relaxation (*i.e.*, trapping) process can result in substantial loss of driving force and rate of charge transfer on microsecond timescales,[165] and is likely dependent on the nature of terminal groups. Being able to accurately determine the timescales of relaxation and the excited states involved in interfacial charge transfers, both structurally and energetically, will give the information needed to engineer better materials.

8. Bibliography

1. Deshmukh, A. Y.; Rathod, D. B.; Tayade, D. T.; Bhagwatkar, R. A.; Patil, S. U., Synthesis and Structural Elucidation of Substituted s-Triazines. *Asian Journal of Chemistry* **2010,** *22* (10), 8252-8254.
2. Zhang, Y.; Liu, J.; Wu, G.; Chen, W., Porous graphitic carbon nitride synthesized via direct polymerization of urea for efficient sunlight-driven photocatalytic hydrogen production. *Nanoscale* **2012,** *4* (17), 5300-5303.
3. Oh, Y. J.; Yoo, J. J.; Kim, Y. I.; Yoon, J. K.; Yoon, H. N.; Kim, J.-H.; Park, S. B., Oxygen functional groups and electrochemical capacitive behavior of incompletely reduced graphene oxides as a thin-film electrode of supercapacitor. *Electrochimica Acta* **2014,** *116* (Supplement C), 118-128.
4. Clayton, C.; Lu, Y., A bipolar model of the passivity of stainless steel: the role of Mo addition. *Journal of the Electrochemical Society* **1986,** *133* (12), 2465-2473.
5. Briggs, D.; Beamson, G., XPS studies of the oxygen 1s and 2s levels in a wide range of functional polymers. *Analytical Chemistry* **1993,** *65* (11), 1517-1523.
6. Li, J.; Shen, B.; Hong, Z.; Lin, B.; Gao, B.; Chen, Y., A facile approach to synthesize novel oxygen-doped g-C3N4 with superior visible-light photoreactivity. *Chemical Communications* **2012,** *48* (98), 12017-12019.
7. Habisreutinger, S. N.; Schmidt-Mende, L.; Stolarczyk, J. K., Photocatalytic Reduction of CO2 on TiO2 and Other Semiconductors. *Angewandte Chemie-international Edition* **2013,** *52* (29), 7372-7408.
8. Parkinson, C. R.; Walker, M.; McConville, C. F., Reaction of atomic oxygen with a Pt(111) surface: chemical and structural determination using XPS, CAICISS and LEED. *Surface Science* **2003,** *545* (1), 19-33.
9. Hisatomi, T.; Kubota, J.; Domen, K., Recent advances in semiconductors for photocatalytic and photoelectrochemical water splitting. *Chemical Society Reviews* **2014,** *43* (22), 7520-7535.
10. Kudo, A.; Miseki, Y., Heterogeneous photocatalyst materials for water splitting. *Chemical Society Reviews* **2009,** *38* (1), 253-278.
11. Zhang, J.; Wang, X., Solar Water Splitting at λ=600 nm: A Step Closer to Sustainable Hydrogen Production. *Angewandte Chemie International Edition* **2015,** *54* (25), 7230-7232.
12. Maeda, K.; Teramura, K.; Lu, D.; Takata, T.; Saito, N.; Inoue, Y.; Domen, K., Photocatalyst releasing hydrogen from water. *Nature* **2006,** *440* (7082), 295-295.
13. Fujishima, A.; Honda, K., Electrochemical Photolysis of Water at a Semiconductor Electrode. *Nature* **1972,** *238* (5358), 37-38.
14. Walter, M. G.; Warren, E. L.; McKone, J. R.; Boettcher, S. W.; Mi, Q.; Santori, E. A.; Lewis, N. S., Solar water splitting cells. *Chemical reviews* **2010,** *110* (11), 6446-6473.

15. Doscher, H.; Geisz, J. F.; Deutsch, T. G.; Turner, J. A., Sunlight absorption in water - efficiency and design implications for photoelectrochemical devices. *Energy & Environmental Science* **2014,** *7* (9), 2951-2956.
16. Hu, S.; Xiang, C.; Haussener, S.; Berger, A. D.; Lewis, N. S., An analysis of the optimal band gaps of light absorbers in integrated tandem photoelectrochemical water-splitting systems. *Energy & Environmental Science* **2013,** *6* (10), 2984-2993.
17. Bolton, J. R.; Strickler, S. J.; Connolly, J. S., Limiting and realizable efficiencies of solar photolysis of water. *Nature* **1985,** *316* (6028), 495-500.
18. Martin, D. J.; Reardon, P. J. T.; Moniz, S. J.; Tang, J., Visible light-driven pure water splitting by a nature-inspired organic semiconductor-based system. *Journal of the American Chemical Society* **2014,** *136* (36), 12568-12571.
19. Pinaud, B. A.; Benck, J. D.; Seitz, L. C.; Forman, A. J.; Chen, Z.; Deutsch, T. G.; James, B. D.; Baum, K. N.; Baum, G. N.; Ardo, S.; Wang, H.; Miller, E.; Jaramillo, T. F., Technical and economic feasibility of centralized facilities for solar hydrogen production via photocatalysis and photoelectrochemistry. *Energy & Environmental Science* **2013,** *6* (7), 1983-2002.
20. Su , D. S.; Zhang, J.; Frank, B.; Thomas, A.; Wang, X.; Paraknowitsch, J.; Schlögl, R., Metal-Free Heterogeneous Catalysis for Sustainable Chemistry. *ChemSusChem* **2010,** *3* (2), 169-180.
21. Wang, Y.; Wang, X.; Antonietti, M., Polymeric Graphitic Carbon Nitride as a Heterogeneous Organocatalyst: From Photochemistry to Multipurpose Catalysis to Sustainable Chemistry. *Angewandte Chemie-international Edition* **2012,** *51* (1), 68-89.
22. Wang, X.; Maeda, K.; Thomas, A.; Takanabe, K.; Xin, G.; Carlsson, J. M.; Domen, K.; Antonietti, M., A metal-free polymeric photocatalyst for hydrogen production from water under visible light. *Nat Mater* **2009,** *8* (1), 76-80.
23. Sprick, R. S.; Jiang, J.-X.; Bonillo, B.; Ren, S.; Ratvijitvech, T.; Guiglion, P.; Zwijnenburg, M. A.; Adams, D. J.; Cooper, A. I., Tunable Organic Photocatalysts for Visible-Light-Driven Hydrogen Evolution. *Journal of the American Chemical Society* **2015,** *137* (9), 3265-3270.
24. Kuhn, P.; Antonietti, M.; Thomas, A., Porous, Covalent Triazine-Based Frameworks Prepared by Ionothermal Synthesis. *Angewandte Chemie-international Edition* **2008,** *47* (18), 3450-3453.
25. Sprick, R. S.; Bonillo, B.; Clowes, R.; Guiglion, P.; Brownbill, N. J.; Slater, B. J.; Blanc, F.; Zwijnenburg, M. A.; Adams, D. J.; Cooper, A. I., Visible-Light-Driven Hydrogen Evolution Using Planarized Conjugated Polymer Photocatalysts. *Angewandte Chemie-international Edition* **2016,** *55* (5), 1792-1796.

26. Stegbauer, L.; Schwinghammer, K.; Lotsch, B. V., A hydrazone-based covalent organic framework for photocatalytic hydrogen production. *Chemical Science* **2014,** *5* (7), 2789-2793.
27. Xia, X.; Deng, N.; Cui, G.; Xie, J.; Shi, X.; Zhao, Y.; Wang, Q.; Wang, W.; Tang, B., NIR light induced H2 evolution by a metal-free photocatalyst. *Chemical Communications* **2015,** *51* (54), 10899-10902.
28. Baur, E.; Rebmann, A., Über Versuche zur Photolyse des Wassers. *Helvetica Chimica Acta* **1921,** *4* (1), 256-262.
29. Chen, C.; Ma, W.; Zhao, J., Semiconductor-mediated photodegradation of pollutants under visible-light irradiation. *Chemical Society Reviews* **2010,** *39* (11), 4206-4219.
30. Abe, R., Development of a new system for photocatalytic water splitting into H2 and O2 under visible light irradiation. *Bulletin of the Chemical Society of Japan* **2011,** *84* (10), 1000-1030.
31. Chen, D.; Ye, J., Photocatalytic H2 evolution under visible light irradiation on AgIn5S8 photocatalyst. *Journal of Physics and Chemistry of Solids* **2007,** *68* (12), 2317-2320.
32. Maeda, K.; Takata, T.; Hara, M.; Saito, N.; Inoue, Y.; Kobayashi, H.; Domen, K., GaN: ZnO solid solution as a photocatalyst for visible-light-driven overall water splitting. *Journal of the American Chemical Society* **2005,** *127* (23), 8286-8287.
33. Sato, J.; Saito, N.; Yamada, Y.; Maeda, K.; Takata, T.; Kondo, J. N.; Hara, M.; Kobayashi, H.; Domen, K.; Inoue, Y., RuO2-Loaded β-Ge3N4 as a Non-Oxide Photocatalyst for Overall Water Splitting. *Journal of the American Chemical Society* **2005,** *127* (12), 4150-4151.
34. Maeda, K.; Domen, K., New Non-Oxide Photocatalysts Designed for Overall Water Splitting under Visible Light. *The Journal of Physical Chemistry C* **2007,** *111* (22), 7851-7861.
35. Zhang, G.; Lan, Z.-A.; Lin, L.; Lin, S.; Wang, X., Overall water splitting by Pt/gC 3 N 4 photocatalysts without using sacrificial agents. *Chemical Science* **2016,** *7* (5), 3062-3066.
36. Konta, R.; Ishii, T.; Kato, H.; Kudo, A., Photocatalytic Activities of Noble Metal Ion Doped SrTiO3 under Visible Light Irradiation. *The Journal of Physical Chemistry B* **2004,** *108* (26), 8992-8995.
37. Yang, M.; Huang, X.; Yan, S.; Li, Z.; Yu, T.; Zou, Z., Improved hydrogen evolution activities under visible light irradiation over NaTaO3 codoped with lanthanum and chromium. *Materials Chemistry and Physics* **2010,** *121* (3), 506-510.
38. Martin, D. J.; Reardon, P. J. T.; Moniz, S. J. A.; Tang, J., Visible Light-Driven Pure Water Splitting by a Nature-Inspired Organic Semiconductor-Based System. *Journal of the American Chemical Society* **2014,** *136* (36), 12568-12571.
39. Lotsch, B. V.; Döblinger, M.; Sehnert, J.; Seyfarth, L.; Senker, J.; Oeckler, O.; Schnick, W., Unmasking Melon by a Complementary Approach

Employing Electron Diffraction, Solid-State NMR Spectroscopy, and Theoretical Calculations—Structural Characterization of a Carbon Nitride Polymer. *Chemistry – A European Journal* **2007,** *13* (17), 4969-4980.
40. Liebig, J., Uber einige Stickstoff - Verbindungen. *Annalen der Pharmacie* **1834,** *10* (1), 1-47.
41. Botari, T.; Huhn, W. P.; Lau, V. W.-h.; Lotsch, B. V.; Blum, V., Thermodynamic Equilibria in Carbon Nitride Photocatalyst Materials and Conditions for the Existence of Graphitic Carbon Nitride g-C3N4. *Chemistry of Materials* **2017,** *29* (10), 4445-4453.
42. Moniz, S. J. A.; Shevlin, S. A.; Martin, D. J.; Guo, Z.-X.; Tang, J., Visible-light driven heterojunction photocatalysts for water splitting – a critical review. *Energy & Environmental Science* **2015,** *8* (3), 731-759.
43. Zhang, G.; Zhang, M.; Ye, X.; Qiu, X.; Lin, S.; Wang, X., Iodine Modified Carbon Nitride Semiconductors as Visible Light Photocatalysts for Hydrogen Evolution. *Advanced Materials* **2014,** *26* (5), 805-809.
44. Chen, X.; Zhang, J.; Fu, X.; Antonietti, M.; Wang, X., Fe-g-C3N4-Catalyzed Oxidation of Benzene to Phenol Using Hydrogen Peroxide and Visible Light. *Journal of the American Chemical Society* **2009,** *131* (33), 11658-11659.
45. Zhang, J.; Sun, J.; Maeda, K.; Domen, K.; Liu, P.; Antonietti, M.; Fu, X.; Wang, X., Sulfur-mediated synthesis of carbon nitride: Band-gap engineering and improved functions for photocatalysis. *Energy & Environmental Science* **2011,** *4* (3), 675-678.
46. Liu, G.; Niu, P.; Sun, C.; Smith, S. C.; Chen, Z.; Lu, G. Q.; Cheng, H.-M., Unique Electronic Structure Induced High Photoreactivity of Sulfur-Doped Graphitic C3N4. *Journal of the American Chemical Society* **2010,** *132* (33), 11642-11648.
47. Wang, Y.; Zhang, J.; Wang, X.; Antonietti, M.; Li, H., Boron- and Fluorine-Containing Mesoporous Carbon Nitride Polymers: Metal-Free Catalysts for Cyclohexane Oxidation. *Angewandte Chemie-international Edition* **2010,** *49* (19), 3356-3359.
48. Zhang, Y.; Mori, T.; Ye, J.; Antonietti, M., Phosphorus-Doped Carbon Nitride Solid: Enhanced Electrical Conductivity and Photocurrent Generation. *Journal of the American Chemical Society* **2010,** *132* (18), 6294-6295.
49. Zhang, Y.; Thomas, A.; Antonietti, M.; Wang, X., Activation of Carbon Nitride Solids by Protonation: Morphology Changes, Enhanced Ionic Conductivity, and Photoconduction Experiments. *Journal of the American Chemical Society* **2009,** *131* (1), 50-51.
50. Niu, P.; Zhang, L.; Liu, G.; Cheng, H.-M., Graphene-Like Carbon Nitride Nanosheets for Improved Photocatalytic Activities. *Advanced Functional Materials* **2012,** *22* (22), 4763-4770.
51. Liu, G.; Wang, T.; Zhang, H.; Meng, X.; Hao, D.; Chang, K.; Li, P.; Kako, T.; Ye, J., Nature-Inspired Environmental "Phosphorylation" Boosts

Photocatalytic H2 Production over Carbon Nitride Nanosheets under Visible-Light Irradiation. *Angewandte Chemie* **2015,** *127* (46), 13765-13769.
52. Bhunia, M. K.; Yamauchi, K.; Takanabe, K., Harvesting Solar Light with Crystalline Carbon Nitrides for Efficient Photocatalytic Hydrogen Evolution. *Angewandte Chemie-international Edition* **2014,** *126* (41), 11181-11185.
53. Lau, V. W.-h.; Moudrakovski, I.; Botari, T.; Weinberger, S.; Mesch, M. B.; Duppel, V.; Senker, J.; Blum, V.; Lotsch, B. V., Rational design of carbon nitride photocatalysts by identification of cyanamide defects as catalytically relevant sites. *Nat Commun* **2016,** *7*.
54. Guo, S.; Deng, Z.; Li, M.; Jiang, B.; Tian, C.; Pan, Q.; Fu, H., Phosphorus-Doped Carbon Nitride Tubes with a Layered Micro-nanostructure for Enhanced Visible-Light Photocatalytic Hydrogen Evolution. *Angewandte Chemie-international Edition* **2016,** *55* (5), 1830-1834.
55. Fang, J.; Fan, H.; Li, M.; Long, C., Nitrogen self-doped graphitic carbon nitride as efficient visible light photocatalyst for hydrogen evolution. *Journal of Materials Chemistry A* **2015,** *3* (26), 13819-13826.
56. Wang, Y.; Li, H.; Yao, J.; Wang, X.; Antonietti, M., Synthesis of boron doped polymeric carbon nitride solids and their use as metal-free catalysts for aliphatic C-H bond oxidation. *Chemical Science* **2011,** *2* (3), 446-450.
57. Wang, Y.; Di, Y.; Antonietti, M.; Li, H.; Chen, X.; Wang, X., Excellent Visible-Light Photocatalysis of Fluorinated Polymeric Carbon Nitride Solids. *Chemistry of Materials* **2010,** *22* (18), 5119-5121.
58. Zhang, J.; Zhang, G.; Chen, X.; Lin, S.; Möhlmann, L.; Dołęga, G.; Lipner, G.; Antonietti, M.; Blechert, S.; Wang, X., Co-Monomer Control of Carbon Nitride Semiconductors to Optimize Hydrogen Evolution with Visible Light. *Angewandte Chemie* **2012,** *124* (13), 3237-3241.
59. Zhang, J.; Chen , X.; Takanabe, K.; Maeda, K.; Domen, K.; Epping, J. D.; Fu, X.; Antonietti, M.; Wang , X., Synthesis of a Carbon Nitride Structure for Visible-Light Catalysis by Copolymerization. *Angewandte Chemie International Edition* **2010,** *49* (2), 441-444.
60. Kang, Y.; Yang, Y.; Yin, L. C.; Kang, X.; Liu, G.; Cheng, H. M., An Amorphous Carbon Nitride Photocatalyst with Greatly Extended Visible-Light-Responsive Range for Photocatalytic Hydrogen Generation. *Advanced Materials* **2015,** *27* (31), 4572-4577.
61. Jorge, A. B.; Martin, D. J.; Dhanoa, M. T. S.; Rahman, A. S.; Makwana, N.; Tang, J.; Sella, A.; Corà, F.; Firth, S.; Darr, J. A.; McMillan, P. F., H2 and O2 Evolution from Water Half-Splitting Reactions by Graphitic Carbon Nitride Materials. *The Journal of Physical Chemistry C* **2013,** *117* (14), 7178-7185.
62. Li, Y.; Wang, Z.; Xia, T.; Ju, H.; Zhang, K.; Long, R.; Xu, Q.; Wang, C.; Song, L.; Zhu, J.; Jiang, J.; Xiong, Y., Implementing Metal-to-Ligand

Charge Transfer in Organic Semiconductor for Improved Visible-Near-Infrared Photocatalysis. *Advanced Materials* **2016,** *28* (32), 6959-6965.
63. Zhang, G.; Lin, L.; Li, G.; Zhang, Y.; Savateev, A.; Zafeiratos, S.; Wang, X.; Antonietti, M., Ionothermal Synthesis of Triazine–Heptazine-Based Copolymers with Apparent Quantum Yields of 60 % at 420 nm for Solar Hydrogen Production from "Sea Water". *Angewandte Chemie International Edition* **2018,** *57* (30), 9372-9376.
64. Yang, S.; Gong, Y.; Zhang, J.; Zhan, L.; Ma, L.; Fang, Z.; Vajtai, R.; Wang, X.; Ajayan, P. M., Exfoliated Graphitic Carbon Nitride Nanosheets as Efficient Catalysts for Hydrogen Evolution Under Visible Light. *Advanced Materials* **2013,** *25* (17), 2452-2456.
65. Lin, L.; Ou, H.; Zhang, Y.; Wang, X., Tri-s-triazine-based Crystalline Graphitic Carbon Nitrides for Highly Efficient Hydrogen Evolution Photocatalysis. *ACS Catalysis* **2016**.
66. Wang, W.; Jimmy, C. Y.; Shen, Z.; Chan, D. K.; Gu, T., gC 3 N 4 quantum dots: direct synthesis, upconversion properties and photocatalytic application. *Chemical Communications* **2014,** *50* (70), 10148-10150.
67. Wang, Y.; Bayazit, M. K.; Moniz, S. J. A.; Ruan, Q.; Lau, C. C.; Martsinovich, N.; Tang, J., Linker-controlled polymeric photocatalyst for highly efficient hydrogen evolution from water. *Energy & Environmental Science* **2017,** *10* (7), 1643-1651.
68. Yu, H.; Shi, R.; Zhao, Y.; Bian, T.; Zhao, Y.; Zhou, C.; Waterhouse, G. I. N.; Wu, L.-Z.; Tung, C.-H.; Zhang, T., Alkali-Assisted Synthesis of Nitrogen Deficient Graphitic Carbon Nitride with Tunable Band Structures for Efficient Visible-Light-Driven Hydrogen Evolution. *Advanced Materials* **2017,** *29* (16), 1605148.
69. Ou, H.; Lin, L.; Zheng, Y.; Yang, P.; Fang, Y.; Wang, X., Tri-s-triazine-Based Crystalline Carbon Nitride Nanosheets for an Improved Hydrogen Evolution. *Advanced Materials* **2017,** *29* (22), 1700008.
70. Yang, P.; Ou, H.; Fang, Y.; Wang, X., A Facile Steam Reforming Strategy to Delaminate Layered Carbon Nitride Semiconductors for Photoredox Catalysis. *Angewandte Chemie International Edition* **2017,** *56* (14), 3992-3996.
71. Wang, L.; Wan, Y.; Ding, Y.; Wu, S.; Zhang, Y.; Zhang, X.; Zhang, G.; Xiong, Y.; Wu, X.; Yang, J.; Xu, H., Conjugated Microporous Polymer Nanosheets for Overall Water Splitting Using Visible Light. *Adv Mater* **2017,** *29* (38), 1702428.
72. Katsumata, H.; Tachi, Y.; Suzuki, T.; Kaneco, S., Z-scheme photocatalytic hydrogen production over WO3/g-C3N4 composite photocatalysts. *RSC Advances* **2014,** *4* (41), 21405-21409.
73. Kong, H. J.; Won, D. H.; Kim, J.; Woo, S. I., Sulfur-Doped g-C3N4/BiVO4 Composite Photocatalyst for Water Oxidation under Visible Light. *Chemistry of Materials* **2016,** *28* (5), 1318-1324.

74. Kang, H. W.; Lim, S. N.; Song, D.; Park, S. B., Organic-inorganic composite of g-C3N4–SrTiO3: Rh photocatalyst for improved H2 evolution under visible light irradiation. *international journal of hydrogen energy* **2012,** *37* (16), 11602-11610.
75. Yan, H.; Yang, H., TiO2–g-C3N4 composite materials for photocatalytic H 2 evolution under visible light irradiation. *Journal of alloys and compounds* **2011,** *509* (4), L26-L29.
76. Zang, Y.; Li, L.; Xu, Y.; Zuo, Y.; Li, G., Hybridization of brookite TiO 2 with gC 3 N 4: a visible-light-driven photocatalyst for As 3+ oxidation, MO degradation and water splitting for hydrogen evolution. *Journal of Materials Chemistry A* **2014,** *2* (38), 15774-15780.
77. Zada, A.; Humayun, M.; Raziq, F.; Zhang, X.; Qu, Y.; Bai, L.; Qin, C.; Jing, L.; Fu, H., Exceptional Visible-Light-Driven Cocatalyst-Free Photocatalytic Activity of g-C3N4 by Well Designed Nanocomposites with Plasmonic Au and SnO2. *Advanced Energy Materials* **2016**.
78. Xu, X.; Liu, G.; Randorn, C.; Irvine, J. T., gC 3 N 4 coated SrTiO 3 as an efficient photocatalyst for H 2 production in aqueous solution under visible light irradiation. *international journal of hydrogen energy* **2011,** *36* (21), 13501-13507.
79. Hong, J.; Wang, Y.; Wang, Y.; Zhang, W.; Xu, R., Noble-Metal-Free NiS/C3N4 for Efficient Photocatalytic Hydrogen Evolution from Water. *ChemSusChem* **2013,** *6* (12), 2263-2268.
80. Chen, Z.; Sun, P.; Fan, B.; Zhang, Z.; Fang, X., In situ template-free ion-exchange process to prepare visible-light-active g-C3N4/NiS hybrid photocatalysts with enhanced hydrogen evolution activity. *The Journal of Physical Chemistry C* **2014,** *118* (15), 7801-7807.
81. Yin, L.; Yuan, Y.-P.; Cao, S.-W.; Zhang, Z.; Xue, C., Enhanced visible-light-driven photocatalytic hydrogen generation over g-C3N4 through loading the noble metal-free NiS 2 cocatalyst. *RSC Advances* **2014,** *4* (12), 6127-6132.
82. Agalave, S. G.; Maujan, S. R.; Pore, V. S., Click Chemistry: 1, 2, 3-Triazoles as Pharmacophores. *Chemistry–An Asian Journal* **2011,** *6* (10), 2696-2718.
83. Ge, L.; Zuo, F.; Liu, J.; Ma, Q.; Wang, C.; Sun, D.; Bartels, L.; Feng, P., Synthesis and efficient visible light photocatalytic hydrogen evolution of polymeric g-C3N4 coupled with CdS quantum dots. *The Journal of Physical Chemistry C* **2012,** *116* (25), 13708-13714.
84. Zhang, J.; Wang, Y.; Jin, J.; Zhang, J.; Lin, Z.; Huang, F.; Yu, J., Efficient visible-light photocatalytic hydrogen evolution and enhanced photostability of core/shell CdS/g-C3N4 nanowires. *ACS applied materials & interfaces* **2013,** *5* (20), 10317-10324.
85. Yan, Z.; Sun, Z.; Liu, X.; Jia, H.; Du, P., Cadmium sulfide/graphitic carbon nitride heterostructure nanowire loading with a nickel hydroxide

cocatalyst for highly efficient photocatalytic hydrogen production in water under visible light. *Nanoscale* **2016,** *8* (8), 4748-4756.
86. Xiang, Q.; Yu, J.; Jaroniec, M., Preparation and enhanced visible-light photocatalytic H2-production activity of graphene/C3N4 composites. *The Journal of Physical Chemistry C* **2011,** *115* (15), 7355-7363.
87. Chen, Y.; Li, J.; Hong, Z.; Shen, B.; Lin, B.; Gao, B., Origin of the enhanced visible-light photocatalytic activity of CNT modified gC 3 N 4 for H 2 production. *Physical Chemistry Chemical Physics* **2014,** *16* (17), 8106-8113.
88. Ge, L.; Han, C., Synthesis of MWNTs/gC 3 N 4 composite photocatalysts with efficient visible light photocatalytic hydrogen evolution activity. *Applied Catalysis B: Environmental* **2012,** *117*, 268-274.
89. Wang, R.; Gu, L.; Zhou, J.; Liu, X.; Teng, F.; Li, C.; Shen, Y.; Yuan, Y., Quasi-Polymeric Metal–Organic Framework UiO-66/g-C3N4 Heterojunctions for Enhanced Photocatalytic Hydrogen Evolution under Visible Light Irradiation. *Advanced Materials Interfaces* **2015,** *2* (10), 1500037-n/a.
90. Ong, W.-J.; Tan, L.-L.; Ng, Y. H.; Yong, S.-T.; Chai, S.-P., Graphitic Carbon Nitride (g-C3N4)-Based Photocatalysts for Artificial Photosynthesis and Environmental Remediation: Are We a Step Closer To Achieving Sustainability? *Chemical Reviews* **2016,** *116* (12), 7159-7329.
91. Shi, H.; Chen, G.; Zhang, C.; Zou, Z., Polymeric g-C3N4 coupled with NaNbO3 nanowires toward enhanced photocatalytic reduction of CO2 into renewable fuel. *Acs Catalysis* **2014,** *4* (10), 3637-3643.
92. Yuan, Y.-P.; Cao, S.-W.; Liao, Y.-S.; Yin, L.-S.; Xue, C., Red phosphor/gC 3 N 4 heterojunction with enhanced photocatalytic activities for solar fuels production. *Applied Catalysis B: Environmental* **2013,** *140*, 164-168.
93. Zhang, J.; Zhang, M.; Sun, R. Q.; Wang, X., A facile band alignment of polymeric carbon nitride semiconductors to construct isotype heterojunctions. *Angewandte Chemie-international Edition* **2012,** *124* (40), 10292-10296.
94. Liu, J.; Wang, H.; Chen, Z. P.; Moehwald, H.; Fiechter, S.; van de Krol, R.; Wen, L.; Jiang, L.; Antonietti, M., Microcontact-Printing-Assisted Access of Graphitic Carbon Nitride Films with Favorable Textures toward Photoelectrochemical Application. *Advanced Materials* **2015,** *27* (4), 712-718.
95. Turner, J. A., A Realizable Renewable Energy Future. *Science* **1999,** *285* (5428), 687-689.
96. Tang, J.; Durrant, J. R.; Klug, D. R., Mechanism of Photocatalytic Water Splitting in TiO2. Reaction of Water with Photoholes, Importance of Charge Carrier Dynamics, and Evidence for Four-Hole Chemistry. *Journal of the American Chemical Society* **2008,** *130* (42), 13885-13891.

97. Kudo, A.; Omori, K.; Kato, H., A Novel Aqueous Process for Preparation of Crystal Form-Controlled and Highly Crystalline BiVO4 Powder from Layered Vanadates at Room Temperature and Its Photocatalytic and Photophysical Properties. *Journal of the American Chemical Society* **1999,** *121* (49), 11459-11467.
98. Martin, D. J.; Umezawa, N.; Chen, X.; Ye, J.; Tang, J., Facet engineered Ag 3 PO 4 for efficient water photooxidation. *Energy & Environmental Science* **2013,** *6* (11), 3380-3386.
99. Liu, J.; Liu, Y.; Liu, N.; Han, Y.; Zhang, X.; Huang, H.; Lifshitz, Y.; Lee, S.-T.; Zhong, J.; Kang, Z., Metal-free efficient photocatalyst for stable visible water splitting via a two-electron pathway. *Science* **2015,** *347* (6225), 970-974.
100. Sui, Y.; Liu, J.; Zhang, Y.; Tian, X.; Chen, W., Dispersed conductive polymer nanoparticles on graphitic carbon nitride for enhanced solar-driven hydrogen evolution from pure water. *Nanoscale* **2013,** *5* (19), 9150-9155.
101. Wang, L.; Wan, Y.; Ding, Y.; Niu, Y.; Xiong, Y.; Wu, X.; Xu, H., Photocatalytic oxygen evolution from low-bandgap conjugated microporous polymer nanosheets: a combined first-principles calculation and experimental study. *Nanoscale* **2017,** *9* (12), 4090-4096.
102. Ruan, Q.; Luo, W.; Xie, J.; Wang, Y.; Liu, X.; Bai, Z.; Carmalt, C. J.; Tang, J., A Nanojunction Polymer Photoelectrode for Efficient Charge Transport and Separation. *Angewandte Chemie International Edition* **2017,** *56* (28), 8221-8225.
103. Wang, L.; Zheng, X.; Chen, L.; Xiong, Y.; Xu, H., Van der Waals Heterostructures Comprised of Ultrathin Polymer Nanosheets for Efficient Z-Scheme Overall Water Splitting. *Angewandte Chemie* **2018,** *130* (13), 3512-3516.
104. Jiang, J.-X.; Su, F.; Niu, H.; Wood, C. D.; Campbell, N. L.; Khimyak, Y. Z.; Cooper, A. I., Conjugated microporous poly(phenylene butadiynylene)s. *Chemical Communications* **2008,** (4), 486-488.
105. Wang, Y.; Suzuki, H.; Xie, J.; Tomita, O.; Martin, D. J.; Higashi, M.; Kong, D.; Abe, R.; Tang, J., Mimicking Natural Photosynthesis: Solar to Renewable H2 Fuel Synthesis by Z-Scheme Water Splitting Systems. *Chemical Reviews* **2018,** *118* (10), 5201-5241.
106. Thilagam, A., Natural light harvesting systems: unraveling the quantum puzzles. *Journal of Mathematical Chemistry* **2015,** *53* (2), 466-494.
107. Andrews, D.; Scholes, G.; Wiederrecht, G., *Comprehensive nanoscience and technology*. Academic Press: 2010.
108. Sayama, K.; Yoshida, R.; Kusama, H.; Okabe, K.; Abe, Y.; Arakawa, H., Photocatalytic decomposition of water into H2 and O2 by a two-step photoexcitation reaction using a WO3 suspension catalyst and an Fe3+/Fe2+ redox system. *Chemical Physics Letters* **1997,** *277* (4), 387-391.
109. Sayama, K.; Mukasa, K.; Abe, R.; Abe, Y.; Arakawa, H., A new photocatalytic water splitting system under visible light irradiation

mimicking a Z-scheme mechanism in photosynthesis. *Journal of Photochemistry and Photobiology A: Chemistry* **2002,** *148* (1–3), 71-77.
110. Abe, R.; Sayama, K.; Sugihara, H., Development of New Photocatalytic Water Splitting into H2 and O2 using Two Different Semiconductor Photocatalysts and a Shuttle Redox Mediator IO3-/I. *The Journal of Physical Chemistry B* **2005,** *109* (33), 16052-16061.
111. Kato, H.; Hori, M.; Konta, R.; Shimodaira, Y.; Kudo, A., Construction of Z-scheme Type Heterogeneous Photocatalysis Systems for Water Splitting into H2 and O2 under Visible Light Irradiation. *Chemistry Letters* **2004,** *33* (10), 1348-1349.
112. Hitoki, G.; Takata, T.; Kondo, J. N.; Hara, M.; Kobayashi, H.; Domen, K., An oxynitride, TaON, as an efficient water oxidation photocatalyst under visible light irradiation ([small lambda] [less-than-or-equal] 500 nm). *Chemical Communications* **2002,** (16), 1698-1699.
113. Iwase, A.; Ng, Y. H.; Ishiguro, Y.; Kudo, A.; Amal, R., Reduced Graphene Oxide as a Solid-State Electron Mediator in Z-Scheme Photocatalytic Water Splitting under Visible Light. *Journal of the American Chemical Society* **2011,** *133* (29), 11054-11057.
114. Kudo, A., Z-scheme photocatalyst systems for water splitting under visible light irradiation. *MRS Bulletin* **2011,** *36* (01), 32-38.
115. Pan, Z. H., T.; Wang, Q.; Chen, S.; Nakabayashi, M.; Shibata, N.; Pan, C.; Takata, T. Katayama, M.; Minegishi, T.; Kudo, A.; Domen, K., Photocatalyst Sheets Composed of Particulate $LaMg_{1/3}Ta_{2/3}O_2N$ and Mo-Doped $BiVO_4$ for Z-Scheme Water Splitting under Visible Light. *ACS Catal.* **2016,** *6*, 7188−7196.
116. Wang, Q.; Hisatomi, T.; Jia, Q.; Tokudome, H.; Zhong, M.; Wang, C.; Pan, Z.; Takata, T.; Nakabayashi, M.; Shibata, N., Scalable water splitting on particulate photocatalyst sheets with a solar-to-hydrogen energy conversion efficiency exceeding 1%. *Nature Materials* **2016,** *15* (6), 611-615.
117. Yoshida, M.; Takanabe, K.; Maeda, K.; Ishikawa, A.; Kubota, J.; Sakata, Y.; Ikezawa, Y.; Domen, K., Role and Function of Noble-Metal/Cr-Layer Core/Shell Structure Cocatalysts for Photocatalytic Overall Water Splitting Studied by Model Electrodes. *The Journal of Physical Chemistry C* **2009,** *113* (23), 10151-10157.
118. Wang, Q.; Hisatomi, T.; Suzuki, Y.; Pan, Z.; Seo, J.; Katayama, M.; Minegishi, T.; Nishiyama, H.; Takata, T.; Seki, K.; Kudo, A.; Yamada, T.; Domen, K., Particulate Photocatalyst Sheets Based on Carbon Conductor Layer for Efficient Z-Scheme Pure-Water Splitting at Ambient Pressure. *Journal of the American Chemical Society* **2017,** *139* (4), 1675-1683.
119. Kobayashi, R.; Tanigawa, S.; Takashima, T.; Ohtani, B.; Irie, H., Silver-Inserted Heterojunction Photocatalysts for Z-Scheme Overall Pure-Water Splitting under Visible-Light Irradiation. *The Journal of Physical Chemistry C* **2014,** *118* (39), 22450-22456.

120. Sasaki, Y.; Nemoto, H.; Saito, K.; Kudo, A., Solar Water Splitting Using Powdered Photocatalysts Driven by Z-Schematic Interparticle Electron Transfer without an Electron Mediator. *J Phys Chem C* **2009,** *113* (40), 17536-17542.
121. Ma, S. S. K.; Maeda, K.; Hisatomi, T.; Tabata, M.; Kudo, A.; Domen, K., A Redox-Mediator-Free Solar-Driven Z-Scheme Water-Splitting System Consisting of Modified Ta3N5 as an Oxygen-Evolution Photocatalyst. *Chem-Eur J* **2013,** *19* (23), 7480-7486.
122. Zhao, G.; Huang, X.; Fina, F.; Zhang, G.; Irvine, J. T., Facile structure design based on C 3 N 4 for mediator-free Z-scheme water splitting under visible light. *Catalysis Science & Technology* **2015,** *5* (6), 3416-3422.
123. Pan, Z.; Zheng, Y.; Guo, F.; Niu, P.; Wang, X., Decorating CoP and Pt Nanoparticles on Graphitic Carbon Nitride Nanosheets to Promote Overall Water Splitting by Conjugated Polymers. *ChemSusChem* **2016**, n/a-n/a.
124. Hansen, J. E., Scientific reticence and sea level rise. *Environmental Research Letters* **2007,** *2* (2), 024002.
125. Seneviratne, S. I.; Donat, M. G.; Pitman, A. J.; Knutti, R.; Wilby, R. L., Allowable CO2 emissions based on regional and impact-related climate targets. *Nature* **2016,** *529*, 477.
126. Forkel, M.; Carvalhais, N.; Rödenbeck, C.; Keeling, R.; Heimann, M.; Thonicke, K.; Zaehle, S.; Reichstein, M., Enhanced seasonal CO2 exchange caused by amplified plant productivity in northern ecosystems. *Science* **2016,** *351* (6274), 696-699.
127. Tu, W.; Zhou, Y.; Zou, Z., Photocatalytic Conversion of CO2 into Renewable Hydrocarbon Fuels: State-of-the-Art Accomplishment, Challenges, and Prospects. *Advanced Materials* **2014,** *26* (27), 4607-4626.
128. Sakimoto, K. K.; Wong, A. B.; Yang, P., Self-photosensitization of nonphotosynthetic bacteria for solar-to-chemical production. *Science* **2016,** *351* (6268), 74-77.
129. Rao, H.; Schmidt, L. C.; Bonin, J.; Robert, M., Visible-light-driven methane formation from CO2 with a molecular iron catalyst. *Nature* **2017,** *548*, 74.
130. Liu, C.; Colón, B. C.; Ziesack, M.; Silver, P. A.; Nocera, D. G., Water splitting–biosynthetic system with CO2 reduction efficiencies exceeding photosynthesis. *Science* **2016,** *352* (6290), 1210-1213.
131. Liu, G.; Meng, X.; Zhang, H.; Zhao, G.; Pang, H.; Wang, T.; Li, P.; Kako, T.; Ye, J., Elemental Boron for Efficient Carbon Dioxide Reduction under Light Irradiation. *Angewandte Chemie International Edition* **2017,** *56* (20), 5570-5574.
132. Kuriki, R.; Yamamoto, M.; Higuchi, K.; Yamamoto, Y.; Akatsuka, M.; Lu, D.; Yagi, S.; Yoshida, T.; Ishitani, O.; Maeda, K., Robust Binding between Carbon Nitride Nanosheets and a Binuclear Ruthenium(II) Complex Enabling Durable, Selective CO2 Reduction under Visible Light in Aqueous Solution. *Angewandte Chemie* **2017,** *129* (17), 4945-4949.

133. Ouyang, T.; Huang, H.-H.; Wang, J.-W.; Zhong, D.-C.; Lu, T.-B., A Dinuclear Cobalt Cryptate as a Homogeneous Photocatalyst for Highly Selective and Efficient Visible-Light Driven CO2 Reduction to CO in CH3CN/H2O Solution. *Angewandte Chemie International Edition* **2017,** *56* (3), 738-743.
134. Abou Asi, M.; He, C.; Su, M.; Xia, D.; Lin, L.; Deng, H.; Xiong, Y.; Qiu, R.; Li, X.-z., Photocatalytic reduction of CO2 to hydrocarbons using AgBr/TiO2 nanocomposites under visible light. *Catalysis Today* **2011,** *175* (1), 256-263.
135. Liu, S.; Zhao, Z.; Wang, Z., Photocatalytic reduction of carbon dioxide using sol-gel derived titania-supported CoPc catalysts. *Photochemical & Photobiological Sciences* **2007,** *6* (6), 695-700.
136. Li, X.; Liu, H.; Luo, D.; Li, J.; Huang, Y.; Li, H.; Fang, Y.; Xu, Y.; Zhu, L., Adsorption of CO2 on heterostructure CdS(Bi2S3)/TiO2 nanotube photocatalysts and their photocatalytic activities in the reduction of CO2 to methanol under visible light irradiation. *Chemical Engineering Journal* **2012,** *180*, 151-158.
137. Truong, Q. D.; Le, T. H.; Liu, J.-Y.; Chung, C.-C.; Ling, Y.-C., Synthesis of TiO2 nanoparticles using novel titanium oxalate complex towards visible light-driven photocatalytic reduction of CO2 to CH3OH. *Applied Catalysis A: General* **2012,** *437*, 28-35.
138. Lee, D.-S.; Chen, H.-J.; Chen, Y.-W., Photocatalytic reduction of carbon dioxide with water using InNbO4 catalyst with NiO and Co3O4 cocatalysts. *Journal of Physics and Chemistry of Solids* **2012,** *73* (5), 661-669.
139. Pan, P.-W.; Chen, Y.-W., Photocatalytic reduction of carbon dioxide on NiO/InTaO4 under visible light irradiation. *Catalysis Communications* **2007,** *8* (10), 1546-1549.
140. Wang, Z.-Y.; Chou, H.-C.; Wu, J. C. S.; Tsai, D. P.; Mul, G., CO2 photoreduction using NiO/InTaO4 in optical-fiber reactor for renewable energy. *Applied Catalysis A: General* **2010,** *380* (1), 172-177.
141. Tsai, C.-W.; Chen, H. M.; Liu, R.-S.; Asakura, K.; Chan, T.-S., Ni@NiO Core–Shell Structure-Modified Nitrogen-Doped InTaO4 for Solar-Driven Highly Efficient CO2 Reduction to Methanol. *The Journal of Physical Chemistry C* **2011,** *115* (20), 10180-10186.
142. Liu, Y.; Huang, B.; Dai, Y.; Zhang, X.; Qin, X.; Jiang, M.; Whangbo, M.-H., Selective ethanol formation from photocatalytic reduction of carbon dioxide in water with BiVO4 photocatalyst. *Catalysis Communications* **2009,** *11* (3), 210-213.
143. Cheng, H.; Huang, B.; Liu, Y.; Wang, Z.; Qin, X.; Zhang, X.; Dai, Y., An anion exchange approach to Bi2WO6 hollow microspheres with efficient visible light photocatalytic reduction of CO2 to methanol. *Chemical Communications* **2012,** *48* (78), 9729-9731.

144. Li, X.; Chen, J.; Li, H.; Li, J.; Xu, Y.; Liu, Y.; Zhou, J., Photoreduction of CO2 to methanol over Bi2S3/CdS photocatalyst under visible light irradiation. *Journal of Natural Gas Chemistry* **2011,** *20* (4), 413-417.
145. Liu, J.-Y.; Garg, B.; Ling, Y.-C., CuxAgyInzZnkSm solid solutions customized with RuO2 or Rh1.32Cr0.66O3 co-catalyst display visible light-driven catalytic activity for CO2 reduction to CH3OH. *Green Chemistry* **2011,** *13* (8), 2029-2031.
146. Mao, J.; Peng, T.; Zhang, X.; Li, K.; Ye, L.; Zan, L., Effect of graphitic carbon nitride microstructures on the activity and selectivity of photocatalytic CO2 reduction under visible light. *Catalysis Science & Technology* **2013,** *3* (5), 1253-1260.
147. Hsu, H.-C.; Shown, I.; Wei, H.-Y.; Chang, Y.-C.; Du, H.-Y.; Lin, Y.-G.; Tseng, C.-A.; Wang, C.-H.; Chen, L.-C.; Lin, Y.-C.; Chen, K.-H., Graphene oxide as a promising photocatalyst for CO2 to methanol conversion. *Nanoscale* **2013,** *5* (1), 262-268.
148. Gusain, R.; Kumar, P.; Sharma, O. P.; Jain, S. L.; Khatri, O. P., Reduced graphene oxide–CuO nanocomposites for photocatalytic conversion of CO2 into methanol under visible light irradiation. *Applied Catalysis B: Environmental* **2016,** *181*, 352-362.
149. Li, H.; Zhang, X.; MacFarlane, D. R., Carbon Quantum Dots/Cu2O Heterostructures for Solar-Light-Driven Conversion of CO2 to Methanol. *Advanced Energy Materials* **2015,** *5* (5), n/a-n/a.
150. Liu, E.; Kang, L.; Wu, F.; Sun, T.; Hu, X.; Yang, Y.; Liu, H.; Fan, J., Photocatalytic Reduction of CO2 into Methanol over Ag/TiO2 Nanocomposites Enhanced by Surface Plasmon Resonance. *Plasmonics* **2014,** *9* (1), 61-70.
151. Zhang, Q.; Lin, C.-F.; Chen, B.-Y.; Ouyang, T.; Chang, C.-T., Deciphering Visible Light Photoreductive Conversion of CO2 to Formic Acid and Methanol Using Waste Prepared Material. *Environmental Science & Technology* **2015,** *49* (4), 2405-2417.
152. Mao, J.; Peng, T.; Zhang, X.; Li, K.; Zan, L., Selective methanol production from photocatalytic reduction of CO2 on BiVO4 under visible light irradiation. *Catalysis Communications* **2012,** *28*, 38-41.
153. Liu, Q.; Low, Z.-X.; Li, L.; Razmjou, A.; Wang, K.; Yao, J.; Wang, H., ZIF-8/Zn2GeO4 nanorods with an enhanced CO2 adsorption property in an aqueous medium for photocatalytic synthesis of liquid fuel. *Journal of Materials Chemistry A* **2013,** *1* (38), 11563-11569.
154. Singhal, N.; Goyal, R.; Kumar, U., Visible-Light-Assisted Photocatalytic CO2 Reduction over InTaO4: Selective Methanol Formation. *Energy & Fuels* **2017,** *31* (11), 12434-12438.
155. Sreethawong, T.; Ngamsinlapasathian, S.; Yoshikawa, S., Photochemically deposited nano-Ag/sol–gel TiO2–In2O3 mixed oxide mesoporous-assembled nanocrystals for photocatalytic dye degradation. *Journal of Colloid and Interface Science* **2014,** *421*, 191-198.

156. Ohno, T.; Murakami, N.; Koyanagi, T.; Yang, Y., Photocatalytic reduction of CO2 over a hybrid photocatalyst composed of WO3 and graphitic carbon nitride (g-C3N4) under visible light. *Journal of CO2 Utilization* **2014,** *6*, 17-25.
157. Di, Y.; Wang, X.; Thomas, A.; Antonietti, M., Making Metal□Carbon Nitride Heterojunctions for Improved Photocatalytic Hydrogen Evolution with Visible Light. *ChemCatChem* **2010,** *2* (7), 834-838.
158. Wojdyla, M.; Gallagher, S. A.; Moloney, M. P.; Gun'ko, Y. K.; Kelly, J. M.; Magno, L. M.; Quinn, S. J.; Clark, I. P.; Greetham, G. M.; Towrie, M., Picosecond to Millisecond Transient Absorption Spectroscopy of Broad-Band Emitting Chiral CdSe Quantum Dots. *The Journal of Physical Chemistry C* **2012,** *116* (30), 16226-16232.
159. Kim, W. D.; Kim, J.-H.; Lee, S.; Lee, S.; Woo, J. Y.; Lee, K.; Chae, W.-S.; Jeong, S.; Bae, W. K.; McGuire, J. A.; Moon, J. H.; Jeong, M. S.; Lee, D. C., Role of Surface States in Photocatalysis: Study of Chlorine-Passivated CdSe Nanocrystals for Photocatalytic Hydrogen Generation. *Chemistry of Materials* **2016,** *28* (3), 962-968.
160. Vietmeyer, F.; Frantsuzov, P. A.; Janko, B.; Kuno, M., Carrier recombination dynamics in individual CdSe nanowires. *Physical Review B* **2011,** *83* (11), 115319.
161. Kadoya, K.; Matsunaga, N.; Nagashima, A., VISCOSITY AND THERMAL-CONDUCTIVITY OF DRY AIR IN THE GASEOUS-PHASE. *Journal of physical and chemical reference data* **1985,** *14* (4), 947-970.
162. Vyas, V. S.; Haase, F.; Stegbauer, L.; Savasci, G.; Podjaski, F.; Ochsenfeld, C.; Lotsch, B. V., A tunable azine covalent organic framework platform for visible light-induced hydrogen generation. *Nature Communications* **2015,** *6*, 8508.
163. Kailasam, K.; Schmidt, J.; Bildirir, H.; Zhang, G.; Blechert, S.; Wang, X.; Thomas, A., Room Temperature Synthesis of Heptazine-Based Microporous Polymer Networks as Photocatalysts for Hydrogen Evolution. *Macromolecular Rapid Communications* **2013,** *34* (12), 1008-1013.
164. Lau, V. W.-h.; Klose, D.; Kasap, H.; Podjaski, F.; Pignié, M.-C.; Reisner, E.; Jeschke, G.; Lotsch, B. V., Dark Photocatalysis: Storage of Solar Energy in Carbon Nitride for Time-Delayed Hydrogen Generation. *Angewandte Chemie International Edition* **2017,** *56* (2), 510-514.
165. Godin, R.; Wang, Y.; Zwijnenburg, M. A.; Tang, J.; Durrant, J. R., Time-Resolved Spectroscopic Investigation of Charge Trapping in Carbon Nitrides Photocatalysts for Hydrogen Generation. *Journal of the American Chemical Society* **2017**.
166. Asahi, R.; Morikawa, T.; Ohwaki, T.; Aoki, K.; Taga, Y., Visible-Light Photocatalysis in Nitrogen-Doped Titanium Oxides. *Science* **2001,** *293* (5528), 269-271.

167. Yang, H. G.; Sun, C. H.; Qiao, S. Z.; Zou, J.; Liu, G.; Smith, S. C.; Cheng, H. M.; Lu, G. Q., Anatase TiO2 single crystals with a large percentage of reactive facets. *Nature* **2008,** *453* (7195), 638-641.
168. Handoko, A. D.; Tang, J., Controllable proton and CO 2 photoreduction over Cu 2 O with various morphologies. *international journal of hydrogen energy* **2013,** *38* (29), 13017-13022.
169. Wang, D.; Ye, J.; Kako, T.; Kimura, T., Photophysical and Photocatalytic Properties of SrTiO3 Doped with Cr Cations on Different Sites. *The Journal of Physical Chemistry B* **2006,** *110* (32), 15824-15830.
170. Dovesi, R.; Orlando, R.; Civalleri, B.; Roetti, C.; Saunders Victor, R.; Zicovich-Wilson Claudio, M., CRYSTAL: a computational tool for the ab initio study of the electronic properties of crystals. In *Zeitschrift für Kristallographie - Crystalline Materials*, 2005; Vol. 220, p 571.
171. Dovesi, R.; Saunders, V.; Roetti, C.; Orlando, R.; Zicovich-Wilson, C.; Pascale, F.; Civalleri, B.; Doll, K.; Harrison, N.; Bush, I., CRYSTAL09 (CRYSTAL09 user's manual). *University of Torino, Torino* **2009**.
172. Dovesi, R.; Causa, M.; Orlando, R.; Roetti, C.; Saunders, V., Abinitio approach to molecular crystals: A periodic Hartree–Fock study of crystalline urea. *The Journal of Chemical Physics* **1990,** *92* (12), 7402-7411.
173. Gatti, C.; Saunders, V.; Roetti, C., Crystal field effects on the topological properties of the electron density in molecular crystals: the case of urea. *The Journal of chemical physics* **1994,** *101* (12), 10686-10696.
174. Grimme, S., Semiempirical GGA-type density functional constructed with a long-range dispersion correction. *Journal of computational chemistry* **2006,** *27* (15), 1787-1799.
175. Dovesi, R.; Saunders, V.; Roetti, C.; Orlando, R.; Zicovich-Wilson, C.; Pascale, F.; Civalleri, B.; Doll, K.; Harrison, N.; Bush, I., CRYSTAL14 user's manual. *University of Torino, Torino* **2014**.
176. Pascale, F.; Zicovich-Wilson, C. M.; Lopez Gejo, F.; Civalleri, B.; Orlando, R.; Dovesi, R., The calculation of the vibrational frequencies of crystalline compounds and its implementation in the CRYSTAL code. *Journal of computational chemistry* **2004,** *25* (6), 888-897.
177. VandeVondele, J.; Hutter, J., Gaussian basis sets for accurate calculations on molecular systems in gas and condensed phases. *The Journal of Chemical Physics* **2007,** *127* (11), 114105.
178. Guidon, M.; Hutter, J.; VandeVondele, J., Auxiliary Density Matrix Methods for Hartree−Fock Exchange Calculations. *Journal of Chemical Theory and Computation* **2010,** *6* (8), 2348-2364.
179. Goedecker, S.; Teter, M.; Hutter, J., Separable dual-space Gaussian pseudopotentials. *Physical Review B* **1996,** *54* (3), 1703-1710.
180. Hutter, J.; Iannuzzi, M.; Schiffmann, F.; VandeVondele, J., CP2K: atomistic simulations of condensed matter systems. *Wiley Interdisciplinary Reviews: Computational Molecular Science* **2014,** *4* (1), 15-25.

181. Kailasam, K.; Mesch, M. B.; Möhlmann, L.; Baar, M.; Blechert, S.; Schwarze, M.; Schröder, M.; Schomäcker, R.; Senker, J.; Thomas, A., Donor–Acceptor-Type Heptazine-Based Polymer Networks for Photocatalytic Hydrogen Evolution. *Energy Technology* **2016,** *4* (6), 744-750.
182. Zhou, Z.; Wang, J.; Yu, J.; Shen, Y.; Li, Y.; Liu, A.; Liu, S.; Zhang, Y., Dissolution and Liquid Crystals Phase of 2D Polymeric Carbon Nitride. *Journal of the American Chemical Society* **2015,** *137* (6), 2179-2182.
183. Ozturk, B.; de-Luna-Bugallo, A.; Panaitescu, E.; Chiaramonti, A. N.; Liu, F.; Vargas, A.; Jiang, X.; Kharche, N.; Yavuzcetin, O.; Alnaji, M.; Ford, M. J.; Lok, J.; Zhao, Y.; King, N.; Dhar, N. K.; Dubey, M.; Nayak, S. K.; Sridhar, S.; Kar, S., Atomically thin layers of B–N–C–O with tunable composition. *Science Advances* **2015,** *1* (6).
184. Tien, H.-W.; Huang, Y.-L.; Yang, S.-Y.; Wang, J.-Y.; Ma, C.-C. M., The production of graphene nanosheets decorated with silver nanoparticles for use in transparent, conductive films. *Carbon* **2011,** *49* (5), 1550-1560.
185. Ren, L.; Yang, F.; Wang, C.; Li, Y.; Liu, H.; Tu, Z.; Zhang, L.; Liu, Z.; Gao, J.; Xu, C., Plasma synthesis of oxidized graphene foam supporting Pd nanoparticles as a new catalyst for one-pot synthesis of dibenzyls. *RSC Advances* **2014,** *4* (108), 63048-63054.
186. Xie, J.; Guo, C.; Yang, P.; Wang, X.; Liu, D.; Li, C. M., Bi-functional ferroelectric BiFeO3 passivated BiVO4 photoanode for efficient and stable solar water oxidation. *Nano Energy* **2017,** *31*, 28-36.
187. Jiang, C.; Moniz, S. J. A.; Khraisheh, M.; Tang, J., Earth-Abundant Oxygen Evolution Catalysts Coupled onto ZnO Nanowire Arrays for Efficient Photoelectrochemical Water Cleavage. *Chemistry – A European Journal* **2014,** *20* (40), 12954-12961.
188. Wang, Y.; Silveri, F.; Bayazit, M. K.; Ruan, Q.; Li, Y.; Xie, J.; Catlow, C. R. A.; Tang, J., Bandgap Engineering of Organic Semiconductors for Highly Efficient Photocatalytic Water Splitting. *Advanced Energy Materials 0* (0), 1801084.
189. Pachfule, P.; Acharjya, A.; Roeser, J.; Langenhahn, T.; Schwarze, M.; Schomäcker, R.; Thomas, A.; Schmidt, J., Diacetylene Functionalized Covalent Organic Framework (COF) for Photocatalytic Hydrogen Generation. *Journal of the American Chemical Society* **2018,** *140* (4), 1423-1427.
190. Xie, J.; Shevlin, S. A.; Ruan, Q.; Moniz, S. J. A.; Liu, Y.; Liu, X.; Li, Y.; Lau, C. C.; Guo, Z. X.; Tang, J., Efficient visible light-driven water oxidation and proton reduction by an ordered covalent triazine-based framework. *Energy & Environmental Science* **2018**.
191. Deifallah, M.; McMillan, P. F.; Corà, F., Electronic and Structural Properties of Two-Dimensional Carbon Nitride Graphenes. *The Journal of Physical Chemistry C* **2008,** *112* (14), 5447-5453.
192. Chen, Y.; Wang, B.; Lin, S.; Zhang, Y.; Wang, X., Activation of n → π* Transitions in Two-Dimensional Conjugated Polymers for Visible Light

Photocatalysis. *The Journal of Physical Chemistry C* **2014,** *118* (51), 29981-29989.
193. Kresse, G.; Furthmüller, J., Efficiency of ab-initio total energy calculations for metals and semiconductors using a plane-wave basis set. *Computational Materials Science* **1996,** *6* (1), 15-50.
194. Blöchl, P. E., Projector augmented-wave method. *Physical Review B* **1994,** *50* (24), 17953-17979.
195. Perdew, J. P.; Burke, K.; Ernzerhof, M., Generalized Gradient Approximation Made Simple. *Physical Review Letters* **1996,** *77* (18), 3865-3868.
196. Grimme, S.; Antony, J.; Ehrlich, S.; Krieg, H., A consistent and accurate ab initio parametrization of density functional dispersion correction (DFT-D) for the 94 elements H-Pu. *The Journal of Chemical Physics* **2010,** *132* (15), 154104.
197. Blöchl, P. E.; Jepsen, O.; Andersen, O. K., Improved tetrahedron method for Brillouin-zone integrations. *Physical Review B* **1994,** *49* (23), 16223-16233.
198. Fina, F.; Callear, S. K.; Carins, G. M.; Irvine, J. T. S., Structural Investigation of Graphitic Carbon Nitride via XRD and Neutron Diffraction. *Chemistry of Materials* **2015,** *27* (7), 2612-2618.
199. Hu, Y.; Shim, Y.; Oh, J.; Park, S.; Park, S.; Ishii, Y., Synthesis of 13C-,15N-Labeled Graphitic Carbon Nitrides and NMR-Based Evidence of Hydrogen-Bonding Assisted Two-Dimensional Assembly. *Chemistry of Materials* **2017,** *29* (12), 5080-5089.
200. Pfitzmann, A.; Fliedner, E.; Fedtke, M., Curing of epoxy resins with dicyandiamide: NMR and IR investigation of isolated main products. *Polymer Bulletin* **1994,** *32* (3), 311-317.
201. El-Gamel, N. E. A.; Seyfarth, L.; Wagler, J.; Ehrenberg, H.; Schwarz, M.; Senker, J.; Kroke, E., The Tautomeric Forms of Cyameluric Acid Derivatives. *Chemistry – A European Journal* **2007,** *13* (4), 1158-1173.
202. Ferrari, A. C.; Rodil, S. E.; Robertson, J., Interpretation of infrared and Raman spectra of amorphous carbon nitrides. *Physical Review B* **2003,** *67* (15), 155306.
203. Larkin, P. J.; Makowski, M. P.; Colthup, N. B., The form of the normal modes of s-triazine: infrared and Raman spectral analysis and ab initio force field calculations. *Spectrochimica Acta Part A: Molecular and Biomolecular Spectroscopy* **1999,** *55* (5), 1011-1020.
204. Carter III, R. O.; Dickie, R. A.; Holubka, J. W.; Lindsay, N. E., Infrared studies of interfacial reactions of dicyandiamide on zinc. *Industrial & Engineering Chemistry Research* **1989,** *28* (1), 48-51.
205. Banfi, D.; Patiny, L., www.nmrdb.org: Resurrecting and Processing NMR Spectra On-line. *CHIMIA International Journal for Chemistry* **2008,** *62* (4), 280-281.

206. Steinbeck, C.; Krause, S.; Kuhn, S., NMRShiftDBConstructing a Free Chemical Information System with Open-Source Components. *Journal of Chemical Information and Computer Sciences* **2003,** *43* (6), 1733-1739.
207. Castillo, A. M.; Patiny, L.; Wist, J., Fast and accurate algorithm for the simulation of NMR spectra of large spin systems. *Journal of Magnetic Resonance* **2011,** *209* (2), 123-130.
208. Casalongue, H. S.; Kaya, S.; Viswanathan, V.; Miller, D. J.; Friebel, D.; Hansen, H. A.; Nørskov, J. K.; Nilsson, A.; Ogasawara, H., Direct observation of the oxygenated species during oxygen reduction on a platinum fuel cell cathode. *Nature Communications* **2013,** *4*, 2817.
209. Schniepp, H. C.; Li, J.-L.; McAllister, M. J.; Sai, H.; Herrera-Alonso, M.; Adamson, D. H.; Prud'homme, R. K.; Car, R.; Saville, D. A.; Aksay, I. A., Functionalized Single Graphene Sheets Derived from Splitting Graphite Oxide. *The Journal of Physical Chemistry B* **2006,** *110* (17), 8535-8539.
210. Li, M.; Wang, Y.; Tang, P.; Xie, N.; Zhao, Y.; Liu, X.; Hu, G.; Xie, J.; Zhao, Y.; Tang, J.; Zhang, T.; Ma, D., Graphene with Atomic-Level In-Plane Decoration of h-BN Domains for Efficient Photocatalysis. *Chemistry of Materials* **2017,** *29* (7), 2769-2776.
211. Zhang, G.; Zhang, J.; Zhang, M.; Wang, X., Polycondensation of thiourea into carbon nitride semiconductors as visible light photocatalysts. *Journal of Materials Chemistry* **2012,** *22* (16), 8083-8091.
212. Zhang, J.; Grzelczak, M.; Hou, Y.; Maeda, K.; Domen, K.; Fu, X.; Antonietti, M.; Wang, X., Photocatalytic oxidation of water by polymeric carbon nitride nanohybrids made of sustainable elements. *Chemical Science* **2012,** *3* (2), 443-446.
213. Gan, Z.; Shan, Y.; Chen, J.; Gui, Q.; Zhang, Q.; Nie, S.; Wu, X., The origins of the broadband photoluminescence from carbon nitrides and applications to white light emitting. *Nano Research* **2016,** *9* (6), 1801-1812.
214. Hu, W.; Lin, L.; Yang, C.; Dai, J.; Yang, J., Edge-Modified Phosphorene Nanoflake Heterojunctions as Highly Efficient Solar Cells. *Nano Letters* **2016,** *16* (3), 1675-1682.
215. Hu, W.; Lin, L.; Zhang, R.; Yang, C.; Yang, J., Highly Efficient Photocatalytic Water Splitting over Edge-Modified Phosphorene Nanoribbons. *Journal of the American Chemical Society* **2017,** *139* (43), 15429-15436.
216. Barton, E. E.; Rampulla, D. M.; Bocarsly, A. B., Selective Solar-Driven Reduction of CO2 to Methanol Using a Catalyzed p-GaP Based Photoelectrochemical Cell. *Journal of the American Chemical Society* **2008,** *130* (20), 6342-6344.
217. Schreier, M.; Curvat, L.; Giordano, F.; Steier, L.; Abate, A.; Zakeeruddin, S. M.; Luo, J.; Mayer, M. T.; Grätzel, M., Efficient photosynthesis of carbon monoxide from CO2 using perovskite photovoltaics. *Nature Communications* **2015,** *6*, 7326.

218. Varela, A. S.; Ranjbar Sahraie, N.; Steinberg, J.; Ju, W.; Oh, H.-S.; Strasser, P., Metal-Doped Nitrogenated Carbon as an Efficient Catalyst for Direct CO2 Electroreduction to CO and Hydrocarbons. *Angewandte Chemie International Edition* **2015,** *54* (37), 10758-10762.
219. Becke, A. D., Density-functional thermochemistry. III. The role of exact exchange. *The Journal of chemical physics* **1993,** *98* (7), 5648-5652.
220. Lee, C.; Yang, W.; Parr, R. G., Development of the Colle-Salvetti correlation-energy formula into a functional of the electron density. *Physical Review B* **1988,** *37* (2), 785-789.
221. An, X.; Li, K.; Tang, J., Cu2O/Reduced Graphene Oxide Composites for the Photocatalytic Conversion of CO2. *ChemSusChem* **2014,** *7* (4), 1086-1093.
222. AlOtaibi, B.; Fan, S.; Wang, D.; Ye, J.; Mi, Z., Wafer-Level Artificial Photosynthesis for CO2 Reduction into CH4 and CO Using GaN Nanowires. *ACS Catalysis* **2015,** *5* (9), 5342-5348.
223. Huang, C.; Chen, C.; Zhang, M.; Lin, L.; Ye, X.; Lin, S.; Antonietti, M.; Wang, X., Carbon-doped BN nanosheets for metal-free photoredox catalysis. *Nature Communications* **2015,** *6*, 7698.
224. Halmann, M., Photoelectrochemical reduction of aqueous carbon dioxide on p-type gallium phosphide in liquid junction solar cells. *Nature* **1978,** *275*, 115.
225. Aresta, M.; Dibenedetto, A., Utilisation of CO2 as a chemical feedstock: opportunities and challenges. *Dalton Transactions* **2007,** (28), 2975-2992.
226. Inoue, T.; Fujishima, A.; Konishi, S.; Honda, K., Photoelectrocatalytic reduction of carbon dioxide in aqueous suspensions of semiconductor powders. *Nature* **1979,** *277*, 637.
227. White, J. L.; Baruch, M. F.; Pander, J. E.; Hu, Y.; Fortmeyer, I. C.; Park, J. E.; Zhang, T.; Liao, K.; Gu, J.; Yan, Y.; Shaw, T. W.; Abelev, E.; Bocarsly, A. B., Light-Driven Heterogeneous Reduction of Carbon Dioxide: Photocatalysts and Photoelectrodes. *Chemical Reviews* **2015,** *115* (23), 12888-12935.
228. Blankenship, R. E.; Tiede, D. M.; Barber, J.; Brudvig, G. W.; Fleming, G.; Ghirardi, M.; Gunner, M. R.; Junge, W.; Kramer, D. M.; Melis, A.; Moore, T. A.; Moser, C. C.; Nocera, D. G.; Nozik, A. J.; Ort, D. R.; Parson, W. W.; Prince, R. C.; Sayre, R. T., Comparing Photosynthetic and Photovoltaic Efficiencies and Recognizing the Potential for Improvement. *Science* **2011,** *332* (6031), 805-809.
229. Shi, L.; Wang, T.; Zhang, H.; Chang, K.; Ye, J., Electrostatic Self-Assembly of Nanosized Carbon Nitride Nanosheet onto a Zirconium Metal–Organic Framework for Enhanced Photocatalytic CO2 Reduction. *Advanced Functional Materials* **2015,** *25* (33), 5360-5367.
230. Wei, J.; Zhou, D.; Sun, Z.; Deng, Y.; Xia, Y.; Zhao, D., A Controllable Synthesis of Rich Nitrogen-Doped Ordered Mesoporous Carbon for CO2

Capture and Supercapacitors. *Advanced Functional Materials* **2013,** *23* (18), 2322-2328.
231. Chen, J.; Shen, S.; Guo, P.; Wu, P.; Guo, L., Spatial engineering of photo-active sites on g-C3N4 for efficient solar hydrogen generation. *Journal of Materials Chemistry A* **2014,** *2* (13), 4605-4612.
232. Li, Q.; Yang, J.; Feng, D.; Wu, Z.; Wu, Q.; Park, S. S.; Ha, C.-S.; Zhao, D., Facile synthesis of porous carbon nitride spheres with hierarchical three-dimensional mesostructures for CO2 capture. *Nano Research* **2010,** *3* (9), 632-642.
233. Martindale, B. C. M.; Hutton, G. A. M.; Caputo, C. A.; Prantl, S.; Godin, R.; Durrant, J. R.; Reisner, E., Enhancing Light Absorption and Charge Transfer Efficiency in Carbon Dots through Graphitization and Core Nitrogen Doping. *Angewandte Chemie International Edition* **2017,** *56* (23), 6459-6463.
234. Wu, X.; Zhu, C.; Wang, L.; Guo, S.; Zhang, Y.; Li, H.; Huang, H.; Liu, Y.; Tang, J.; Kang, Z., Control Strategy on Two-/Four-Electron Pathway of Water Splitting by Multidoped Carbon Based Catalysts. *ACS Catalysis* **2017,** *7* (3), 1637-1645.
235. Li, H.; He, X.; Kang, Z.; Huang, H.; Liu, Y.; Liu, J.; Lian, S.; Tsang, C. H. A.; Yang, X.; Lee, S.-T., Water-Soluble Fluorescent Carbon Quantum Dots and Photocatalyst Design. *Angewandte Chemie International Edition* **2010,** *49* (26), 4430-4434.
236. Gupta, V.; Chaudhary, N.; Srivastava, R.; Sharma, G. D.; Bhardwaj, R.; Chand, S., Luminscent Graphene Quantum Dots for Organic Photovoltaic Devices. *Journal of the American Chemical Society* **2011,** *133* (26), 9960-9963.
237. Kwon, W.; Lee, G.; Do, S.; Joo, T.; Rhee, S.-W., Size-Controlled Soft-Template Synthesis of Carbon Nanodots toward Versatile Photoactive Materials. *Small* **2014,** *10* (3), 506-513.
238. Li, X.; Rui, M.; Song, J.; Shen, Z.; Zeng, H., Carbon and Graphene Quantum Dots for Optoelectronic and Energy Devices: A Review. *Advanced Functional Materials* **2015,** *25* (31), 4929-4947.
239. Lim, S. Y.; Shen, W.; Gao, Z., Carbon quantum dots and their applications. *Chemical Society Reviews* **2015,** *44* (1), 362-381.
240. Ong, W.-J.; Putri, L. K.; Tan, Y.-C.; Tan, L.-L.; Li, N.; Ng, Y. H.; Wen, X.; Chai, S.-P., Unravelling charge carrier dynamics in protonated g-C3N4 interfaced with carbon nanodots as co-catalysts toward enhanced photocatalytic CO2 reduction: A combined experimental and first-principles DFT study. *Nano Research* **2017,** *10* (5), 1673-1696.
241. Qu, S.; Wang, X.; Lu, Q.; Liu, X.; Wang, L., A Biocompatible Fluorescent Ink Based on Water-Soluble Luminescent Carbon Nanodots. *Angewandte Chemie International Edition* **2012,** *51* (49), 12215-12218.
242. Hu, C.; Liu, Y.; Yang, Y.; Cui, J.; Huang, Z.; Wang, Y.; Yang, L.; Wang, H.; Xiao, Y.; Rong, J., One-step preparation of nitrogen-doped

graphene quantum dots from oxidized debris of graphene oxide. *Journal of Materials Chemistry B* **2013,** *1* (1), 39-42.
243. Qu, L.; Liu, Y.; Baek, J.-B.; Dai, L., Nitrogen-Doped Graphene as Efficient Metal-Free Electrocatalyst for Oxygen Reduction in Fuel Cells. *ACS Nano* **2010,** *4* (3), 1321-1326.
244. Choi, C. H.; Chung, M. W.; Kwon, H. C.; Park, S. H.; Woo, S. I., B, N- and P, N-doped graphene as highly active catalysts for oxygen reduction reactions in acidic media. *Journal of Materials Chemistry A* **2013,** *1* (11), 3694-3699.
245. Gong, Y.; Shi, G.; Zhang, Z.; Zhou, W.; Jung, J.; Gao, W.; Ma, L.; Yang, Y.; Yang, S.; You, G.; Vajtai, R.; Xu, Q.; MacDonald, A. H.; Yakobson, B. I.; Lou, J.; Liu, Z.; Ajayan, P. M., Direct chemical conversion of graphene to boron- and nitrogen- and carbon-containing atomic layers. *Nature Communications* **2014,** *5*, 3193.
246. Yang, X.; Zhang, X.; Ma, Y.; Huang, Y.; Wang, Y.; Chen, Y., Superparamagnetic graphene oxide-Fe3O4nanoparticles hybrid for controlled targeted drug carriers. *Journal of Materials Chemistry* **2009,** *19* (18), 2710-2714.
247. Yan, J.-A.; Xian, L.; Chou, M. Y., Structural and Electronic Properties of Oxidized Graphene. *Physical Review Letters* **2009,** *103* (8), 086802.
248. Robertson, J.; O'Reilly, E. P., Electronic and atomic structure of amorphous carbon. *Physical Review B* **1987,** *35* (6), 2946-2957.
249. Kim, B.; Ma, S.; Molly Jhong, H.-R.; Kenis, P. J. A., Influence of dilute feed and pH on electrochemical reduction of CO2 to CO on Ag in a continuous flow electrolyzer. *Electrochimica Acta* **2015,** *166*, 271-276.
250. Iwasita, T., Electrocatalysis of methanol oxidation. *Electrochimica Acta* **2002,** *47* (22), 3663-3674.
251. Navarro, R. M.; Peña, M. A.; Fierro, J. L. G., Production of Hydrogen by Partial Oxidation of Methanol over a Cu/ZnO/Al2O3 Catalyst: Influence of the Initial State of the Catalyst on the Start-Up Behaviour of the Reformer. *Journal of Catalysis* **2002,** *212* (1), 112-118.
252. Jiang, Z.; Xiao, T.; Kuznetsov, V. L.; Edwards, P. P., Turning carbon dioxide into fuel. *Philosophical Transactions of the Royal Society A: Mathematical, Physical and Engineering Sciences* **2010,** *368* (1923), 3343-3364.
253. Lau, V. W.-h.; Yu, V. W.-z.; Ehrat, F.; Botari, T.; Moudrakovski, I.; Simon, T.; Duppel, V.; Medina, E.; Stolarczyk, J.; Feldmann, J.; Blum, V.; Lotsch, B. V., Urea-Modified Carbon Nitrides: Enhancing Photocatalytic Hydrogen Evolution by Rational Defect Engineering. *Advanced Energy Materials* **2017**, 1602251-n/a.
254. Godin, R.; Kafizas, A.; Durrant, J. R., Electron transfer dynamics in fuel producing photosystems. *Current Opinion in Electrochemistry* **2017,** *2* (1), 136-143.